PORTABLE ELECTROMAGNETIC SURFACE

PROFILING SYSTEM

by

Bassel Mohamad Al Homssi

A Thesis Presented to the Faculty of the
American University of Sharjah
College of Engineering
in Partial Fulfillment
of the Requirements
for the Degree of

Master of Science in
Electrical Engineering

Sharjah, United Arab Emirates

June 2016

Approval Signatures

We, the undersigned, approve the Master's Thesis of Bassel Mohamad Al Homssi.

Thesis Title: Portable Electromagnetic Surface Profiling System

Signature	**Date of Signature** (dd/mm/yyyy)
_____	_____
Dr. Nasser Qaddoumi Professor, Department of Electrical Engineering Thesis Advisor	
_____	_____
Dr. Bassam Abu-Nabah Assistant Professor, Department of Mechanical Engineering Thesis Co-Advisor	
_____	_____
Dr. Amer Zakarai Assistant Professor, Department of Electrical Engineering Thesis Committee Member	
_____	_____
Dr. Mamoun Abdel-Hafez Associate Professor, Department of Mechanical Engineering Thesis Committee Member	
_____	_____
Dr. Nasser Qaddoumi Professor, Department of Electrical Engineering	
_____	_____
Dr. Mohamed El-Tarhuni Associate Dean, College of Engineering	
_____	_____
Dr. Leland Blank Dean, College of Engineering	
_____	_____
Dr. Khaled Assaleh Interim Vice Provost for Research and Graduate Studies	

Acknowledgement

My sincerest appreciation goes to my thesis Advisor Dr. Nasser Qaddoumi, head of the Electrical Engineering Department, at the American University of Sharjah. His continued support, guidance and expert advice did not only steer me in the right direction but also inspired me to no end. I will continue to value his exceptional approach to science and research.

The encouragement and enthusiasm of my second advisor Dr. Bassam Abu-Nabah, have been rewarding both on the intellectual and personal levels. His energy and meticulous attention to detail were a driving force that kept me going. The valuable recommendations and knowledge he provided, were fundamental to the work done.

My gratitude extends to the committee members Drs. Mamoun Abdel-Hafiz and Dr. Amer Zakaria, for their valuable suggestions, and for the earnest dedication they displayed. I thank them for their insightful comments and questions during the oral presentation.

I am greatly fortunate to have had extraordinary mentors over the course of my academic years. This goes for Dr. Hasan Mir for his mentorship, and the valuable expertise he shared at every turn. His boundless reserve of knowledge, experience, and aptitude are inspirational. A special thanks goes to Dr. Yussof Zureigat whose thoughts, approach and devotion to education ultimately had a pronounced impact on my work.

I would finally like to thank my parents for their unlimited love and encouragement. Their passion for science was always a source of strength and motivation in my life. For my family's ability to display unconditional support in everything I tackle, thank you.

To all humanity…

Abstract

Due to its potential accuracy and speed, the use of profiling and detection sensing systems has been gaining rapid popularity in the industry. Whether they are implemented in coordinate measurement machines or encoded in custom-designed measurement systems, real-time accuracy and precision in determining the sensor position and orientation are crucial elements to the performance of inspection sensor measurement techniques. Uncertainty in tracking these sensors within a measurement system can adversely affect the quality of 3-dimensional surface profiling techniques. Recent advancements in micro-electro-mechanical systems and their applications in multiple-axis inertia measurement units (IMUs) have been offering relatively high accuracy and precision in determining linear accelerations and angular velocities within the operating range of inspection measurement systems. This effort targets taking a step forward towards integrating IMUs to offer robust and portable inspection measurement systems. Utilizing the gyroscope as a feedback, different forward models will be analyzed to accurately extract gravitational acceleration from IMU's accelerometer measurements at random real-time orientations simulating realistic measurement environments. Accuracy in the forward model lends itself for real-time assessment of a sensor's position and orientation as part of the inverse model, which will be investigated with different physics-based data processing techniques. Forward and inverse models and their real-time transformational matrixes allow taking a point from the sensor coordinate system to the world coordinate system. The developed models are tested for dimensional accuracy against known input profiles to show the potential capabilities and limitations of the proposed effort. Using the proposed algorithm, the drift bias error was minimized drastically demonstrating potential in usage as an alternative to bulky profiling machines used conventionally.

Search Terms: Laser vision sensor; Surface profiling; coordinate systems; Euler angles

Table of Contents

List of Figures

List of Tables

List of Abbreviations

1D	-	One Dimensional
2D	-	Two Dimensional
3D	-	Two Dimensional
DC	-	Direct Current
DSP	-	Digital Signal Processing
FT	-	Fourier Transform
GPS	-	Global Position Sensor
HPF	-	High Pass Filter
IMU	-	Inertial Measurement Unit
INS	-	Inertial Navigation System
LPF	-	Low Pass Filter
LVS	-	Laser Vision Sensor
MEMS	-	Micro-electro-mechanical System
NDT	-	Non-Destructive Testing
SNR	-	Signal to Noise Ratio
WT	-	Wavelet Transform

Chapter 1: Portable Position Tracking

1.1 Profiling System Limitations

Portability of a measurement system is a very important characteristic that has been developed to be attractive in the twenty first century. Phones are mobile, computers are mobile and so are cameras. Recently, the industry has been demanding for portable three dimensional (3D) surface profiling systems. The problem in mobility is that it is not only dependent on the size of the system but also its speed. Most profiling systems available are extremely slow when compared to microprocessor speeds or even mobile phone speeds.

1.2 Problem Formulation

Given the limitations in profiling systems present, an extremely fast, cheap and relatively small in size system is needed in order to fulfill the mobility role needed and compensate for the speed limitations of the hardware motors imposed in the conventional bulky systems. Another important criterion is the programmability of the system to allow for the vastest type of measurements required. As thus, any solution to the proposed problem is required to be flexible in terms of measurement setups and profiling surfaces.

1.3 Proposed Solution

Inertial Navigation Systems (INS) are systems that estimate position based on the present location in relevance to a previous location. The distinctive characteristics of INS allow it to assist navigation processes, making it a favorable solution in a wide range of fields. It was adopted by a diversity of applications to include the fields of automobiles, mechatronics, biomedical, and biometric analysis [1-12]. Capturing position for a set of readings requires an accurate representation. One of the eminent proposed solutions is the accelerometer. Accelerometers have been the main focus of many researches due to their portability and affordability [1-12]. The appeal of accelerometers comes from its use of low power integrated circuits along with its small size, low weight and relatively acceptable measurements. This ultimately facilitates the use of single and multiple arrays on readings [1, 2]. Accelerometers have been contrasted against other amiable tools such as Global Positioning Systems (GPS) and

odometers. When compared to GPS, accelerometers are superior in terms of signal coverage, however, unlike the GPS, they encounter high drift errors. Signal blockage is a critical drawback in absolute position sensors, such as GPS, radar and active beacon. In contrast to odometers, which deliver 1D data along the path of motion, accelerometers can measure in all three dimensions using tri-axial sensor design, and can result in higher data rates. Moreover, accelerometers are self-contained devices which makes them more attainable than odometers. Therefore, for an application that requires mobility on a relatively short period of time, accelerometers are found to be far more adequate [3, 4]. Much of the present technology focuses on the incorporation of an amalgam of sensors as opposed to the accelerometer. The benefit of using an accelerometer instead is that it replaces the more complex algorithms involved, with simpler ones. Other studied solutions were derived from the use of high power devices. Nevertheless, such a technique qualifies the monitoring proficiencies and offline analysis. Besides, the use of these high power sensors such as gyroscopes is limited due to the fact that they are cost ineffective [2]. Another benefit to the use of accelerometers, is the ease of calibration due to the gravity bias, replacing many other sensors that required high calibration criteria [5].

Numerous studies evaluated position calculations using accelerometers in an attempt to estimate position. Accelerometers have been the main focus in terms of velocity and position estimation to support vehicle and robotic navigation. Technological leaps in the gaming fields enabled the accelerometers embedded in smart phones to act as remote controllers. Accelerometers make use of motion recognition, sensing techniques that evaluate both position and speed during movements of the console, i.e. smart phone [6]. Research efforts have rather expanded the potential use of the accelerometer embedded in smart phones to encompass gait recognition. Despite the computational limitations of smart phones, the use of accelerometers fixated within smart phones was proven to be a feasible approach [7]. Accelerometers have also been used to classify Parkinson tremor from the position readings. The readings were able to clearly characterize the distinguishing factors that can aid in proper classification [8], whereas, in the field of biometric analysis, accelerometers are used in estimating the distance covered by runners to classify fatigue breakdown in runners' performance [9]. Mathematical models were developed in order to estimate the distance covered typically by a person's stride, with the aid of Euler angle measurement to identify the existence of gravity in the readings. Along with the acceleration measurements

provided by the accelerometers, the change of the center of gravity of the body helps to maintain accurate readings. The presence of gravity in one or more of the axis enables the mathematical model to realize more viable readings. Those mathematical models were developed by using a pedometer and a tri-axial accelerometer. In a smart phone, the accelerometer data is usually manipulated to estimate the pedometer data [10, 11]. Similarly, the different human activities can also be both monitored and classified using a tri-axial accelerometer. The accelerometer can distinguish between the activities of walking, sitting and lying accurately by using raw acceleration values without displacement calculations [1]. The diverse applications of this technology allowed for its use in sports coaching. An integration between accelerometers and GPS allowed for a quantitative analysis of velocity and stroke measurement of swimmers. The implementation of the technology was proven to be beneficial for sports professionals and scientists, with the potential of replacing classical quantifying methods such as video analysis [12]. Another sensor that is usually integrated with the accelerometer in order to utilize a higher accuracy location analysis is the gyroscope. Gyroscopes are used for inertial rotation sensing, by measuring angular velocities which can then be integrated. Gyroscope measurements are coupled with bias, and so high-pass filtering is required for the angular velocities. Similar to acceleration values, angular velocities require a rotation algorithm that can associate the values with the body's coordinate system. Gyroscopes allow for an accurate representation of orientation over a short period of time. The convenience of using a gyroscope is derived from its ability to adapt to instantaneous changes in a dynamic system [13]. The more commonly used Micro-Electro-Mechanical System (MEMS) gyroscope is popular for its low cost, portability and lightweight nature. Compensation for the shortfalls of a MEMS gyroscope is done through the use of the proper processing tool [14]. Moreover, power consumption of MEMS gyroscopes is relatively minimal, and so gyroscopes are considered to be a viable option for energy conservation. For instance, the power dissipation for a simple axis MEMS gyroscope can be as low as below 30mW [15].

The use of gyroscopes for orientation determination has infiltrated, in the versatility of its application, many fields. In regards to automobile- satellite communication, gyroscopes were found beneficial in securing moving vehicle connectivity. In dealing with moving vehicles, the most prominent task lies in establishing an unerring link to the satellite. A study on establishing a method to ascertain vehicle altitude proposes the use of GPS antennas along with a triad

accelerometer and gyroscope. The merging of these sensors, combined with the appropriate filtering techniques provides an efficacious, yet cost effective solution [16]. Moreover, researchers have also studied the incorporation of gyroscopes to mobile phones for vision applications. A research on the assessment of camera motion unites the concepts of visual and inertial sensors. Challenges in visual stabilization and camera tracking, are a result of the camera's way of capturing a row in a frame. Cameras within cell phones capture rows consecutively as opposed to simultaneously, which in the case of fast motion causes a distortion in the frame. Despite the existence of many texts that assume an offline synchronization or calibration of these two integrated systems, this study proposes providing means to allow for online calibration in the fusion of camera and gyroscopes [17]. In addition, applications of gyroscopes extend to implications in robotics. Challenges of orientation are imperative in the field of robotics for obvious importance associated with establishment of impact free paths for a moving robot and machine stabilization [18]. Furthermore, beyond the scope of automobiles and robotics, gyroscopes can be used in aviation for autopilot projects. A study on a navigation system for such a project involved the use of cameras, gyroscopes and accelerometers [19].

The coupling of gyroscopes with accelerometers, allows for the combination of the benefits acquired from angular velocity and acceleration measurements. The biases accompanying gyroscope measurements make it a suitable method only over short periods, while the delays and vibrations accompanying accelerometer readings make it an appropriate method for long-term measurements. [13, 16]. The inertial systems for orientation measurement can evaluate velocity, position and altitude. Their fusion can therefore be an asset in so many applications. These systems, however, require proper calibration; which is generally facilitated by Kalman filters [20]. The incorporation of Kalman filters within the amalgamated system allows each orientation measurement method to compensate for the shortfalls of the other method. The fusion can therefore, ideally result in an overall enhancement in the sensitivity and stability of the system that is durable over both short and long periods of time [13, 16].

1.3 Sensor Types

In the literature, for position tracking applications, two main accelerometer types are used. Those accelerometers are classified based on the architecture and material used to sense the vibrations in order to translate it into acceleration

measurements. Capacitive accelerometers take the advantage of the capacitor model which measures the change of voltage which directly corresponds to acceleration values. There is a third plate suspended between the two fixed plates of the capacitor making the capacitor split into three different capacitors. When the suspended middle plate moves, the capacitance which is a function of distance is also affected. This relates to the voltage of the overall system which in turn once calibrated versus acceleration, produces different values of acceleration [21]. The main capacitive accelerometers are made using MEMS technology due to its relatively small sizes and easy integration to chips. Piezoelectric accelerometers are also another type of accelerometers depending on a piezoelectric material that is stressed with motion and produces charge variations. Since charge is a function of current and voltage of the overall sensor, acceleration is calibrated versus voltage, and for every voltage value, different acceleration values can be outputted [22].

1.4 Errors in IMUs and Compensation Models

In light of the challenging convolutions accompanying the operational aspects of accelerometers and other relative positioning sensors, it is reasonably prevised that certain errors will inexorably accompany position calculations. These errors can induce substantial deviations from the exact real measurements; a small acceleration error can cause a large amplification resulting in misleading position assessments. The reason for this amplification is the accumulation of error from the process of double integrating measured acceleration values. Fortunately, most of the errors that ensue from accelerometer measurements despite the accumulation are still considered negligible. However, some errors must still be nullified in order to obtain viable data. Bias drift error generated by the accelerometer's acceleration readings is the most significant type of error [1-4, 8]. Another common error that affects accelerometers' readings is bias instability. The acceleration values change their bias or offset even at static position due to environmental changes such as temperature, external stress, and pressure on the system; this is usually referred to as the Thermal Bias Error [4]. To reduce the effects of bias drift, thermal bias and random noise in accelerometer readings, various techniques were studied. Kalman filtering techniques were imposed as a solution to reduce these effects. Since the orientation estimation produces a nonlinear system, Kalman filters are typically appropriate for these systems. Two generally investigated classes of Kalman filters are the extended and unscented Kalman filters. When

subjected to trigonometric functions, the unscented Kalman filter shows eminence in comparison to the extended Kalman filter. The superiority of the unscented Kalman filter comes from the simplicity of its algorithm. Hence, the viability of its implementation in a digital signal processor is adequate. The algorithm for an unscented Kalman filter is regarded simpler because it does not require the evaluation of the Jacobian matrix [16]. A newly proposed method of Kalman filtering is the Naive Kalman filtering. The Naive Kalman filter makes use of different distinct Kalman filters based on each of the three compartments within the angular velocity vector. The proposed use of Naive Kalman filters is a consequence of its ability to disentangle a complex problem by subdividing the angular velocity vector, dealing with each independent compartment separately [18]. Besides, some research utilizes the use of adaptive Kalman filtering, which is essentially an enhanced conventional Kalman filter. The improvement is based upon a processing technique that continuously updates the time changing variables [14]. To simplify, a Kalman filter is a statistical algorithm that uses two phases; a predictor and a corrector. The predictor as a concept foresees the values of acceleration that are yet to be read by the sensor. The corrector evaluates a value in relation to the predicted value and the actual value read by the accelerometer [4, 23]. Another proposed error reduction method is the usage of an error model along with the Kalman filter. This technique makes use of other sensor such as gyroscopes in order to reduce the bias drift [3]. Bias errors can also be compensated by a model made of a linear neural network model that calculates the coefficients in order to mathematically manipulate the values and efficiently reduce the error. However, a calibration criterion is needed beforehand with known inputs and outputs in order to 'teach' the neural network system of the error behavior. When properly formulated, results show better representation of the acceleration and velocity profiles leading to lower bias errors [24].

Random noise is another factor that can impair acceleration values. This error occurs when the signal-to-noise ratio (SNR) of the accelerometer is low allowing for overlapping and mixing between the acceleration signal and the noise. However, even with high SNR accelerometers, some random noise blends with the signal. This type of error is usually qualified by using filters [1-3]. Wavelet Transform (WT) is a technique that helped make an accelerometer's output values more accurate by reducing the random noise effects. The characteristics of the wavelet transform allow it to break down the signal generated by an accelerometer. In comparison to the famous Fourier

Transform (FT), the WT is far more efficient than the FT in dealing with the transient response of acceleration coming from robotic arm, hand movement, or any mechanical dynamic system [2]. WT can allow for further filtering of the signal coming from an accelerometer with the use of a suitable mother signal and signal decomposition factors, hence, ending up with signals with less fluctuations and smoother in response. Another proposed method to limit random noise is the dynamic mean method. This method is a form of down sampling. Down sampling allows for a running average that can be taken every few samples in order to reduce the noise error coming from the accelerometer. This method takes care of any signal that fluctuates around a certain set value. The logic behind this mechanism is effective since the higher values are taken care of by averaging them with the lower values keeping a consistent and more reasonable set of data [8]. The problem with WT or FT is that a constant model of the noise is needed as an input to the system. However, noise profiles usually change based on many factors such as temperature, medium characteristics, or even the signals passing through. Consequently, the constant model tends to fail to depict the noise in an online manner. Adaptive filtering techniques can change that. The filter adapts to the surrounding, and deploys a noise model based on a real time noise identification system. A highly used adaptive filter is the Least Mean Square (LMS) and Block Least Mean Square (BLMS) adaptive filters. By comparing the input acceleration data with the noise from the surrounding, the adaptive filter calculates a set of coefficients that acts as a filter in order to remove the noise in an iterative manner until a certain accuracy is acquired [25, 26]. Table 1.1 summarizes the different compensation methods and the corresponding reduced type of error.

Table 1.1: Error Compensation Methods

Error Type	**Compensation Methods**
Bias Drift Error	Kalman Filter
	Complementary Filter
	Least Mean Square
Random Noise Error	Discrete Wavelet Transform
	Least Mean Square
	Dynamic Mean
Orientation Error	More Accelerometers
	Rotation using Euler Angles

Orientation error is an error that follows from the difference between the accelerometer axis and the body frame axis. This error usually arises from the misalignment of the accelerometer and the body frame on which it is mounted. The gravity force affects one of the axis. However, the problem occurs when the accelerometer is tilted and the gravity force is divided unequally to the other axis. When this occurs, it is usually hard to identify the location of the accelerometer accurately and algorithms needed to reduce the acceleration values of gravity force are necessary [27, 28]. Many methods were developed in an attempt to eradicate this type of error, nonetheless, most need the knowledge of either the exact value of the bias voltage of the accelerometer or the maximum and minimum acceleration values i.e. gravity for each axis [27]. Considering that noise is never nullified completely, it is nearly impossible to determine the absolute maximum and minimum acceleration values. In order to reduce this error, mathematical derivations and filtering techniques were developed. These methods are established to identify and reallocate the orientation of the accelerometer [27]. By using the angular acceleration, the accelerometer values can be adjusted. Another way of minimizing this error is the installation of many closely packed accelerometers on the same body frame. Nevertheless, the large number of sensors makes it a costly method, and one that relies on intricate computations [29]. Unlike calibration techniques which are usually performed in the waking up sequence of the accelerometer i.e. before it is even used, other procedures using Euler angles and rotational matrices were generated. This method takes every set of accelerometer data and orients it to a reference position set beforehand. Roll, Pitch and Yaw are calculated based on the acceleration values. Studies combine magnetometers and accelerometers in order to calculate Euler angles using six different methodologies. Those six methodologies are unique in terms of the values used to calculate the angles. However, not all six methods produce accurate data, hence, depending on the rotation axis, a method is chosen over another. Those six methods depend on the accelerating axis, for example, if a high acceleration were to act on the *x*-axis the accelerometer values in both *y*-axis and *z*-axis along with magnetic force along *y* or *z* are used in order to calculate Roll, Pitch and Yaw [30]. An alternative method to calculating Roll and Pitch, is using trigonometric relations that use discrete values that are measured solely from the accelerometer [31]. Once these angles are accurately acquired, a rotation matrix is imposed on the acceleration values in order to realign them back to the reference set point. If rotation was to occur along the *y*-axis, the angles corresponding to this change

will be multiplied with the acceleration values in order to realign it. This also nullifies any tendency for tilt errors [31-33]. Once the reference point is fixed to set gravity in a certain axis, then after multiplying the acceleration values by the rotation matrix, the acceleration values will be corrected and the gravity component will only show in that certain fixed axis.

1.5 Surface Profiling System

In order to capture rich and accurate three dimensional information from the surface of the body being examined, a vision sensing technique is required. Many profiling systems were established in order to meet the requirements imposed by the industry. In order to detect information on a surface of a rigid body, the profiling systems required a tremendous amount of time to only capture a small area of the body [24-35].

1.5.1 Laser vision sensor

Laser vision sensor (LVS) is a surface profiling mechanism that excels at capturing such information due to its lack of noise sensitivity and high recognition sensitivity when compared to other profiling systems [34]. Overall, LVS profiling systems are inexpensive, and a camera that has a high frame rate can accomplish the job [35]. Moreover, laser beams have strong orientation and high energy density leading to a high SNR offering higher profiling precision [36]. Moreover, LVS systems have been used for profiling in many applications due to their dominance in information capturing. Weld deficiency detection has been the main focus of many industries such as oil and gas industries. LVS was implemented to test pipe deficiencies leading into a noncontact profiling technique [37-39]. Another step forward was to fully automate the procedure of welding and making a feedback loop by using the LVS system to detect the deficits allowing the welding to correct itself automatically [40-42]. In order to detect those deficiencies, a profiling system is required. Robotic welding underwater is another domain where LVS was implemented and returned high precision feedback [43-45]. LVS profiling system requires a charge-coupled device (CCD) camera in order to capture the projection of the laser beam on the body of the surface in order to implement the profiling mechanism [40]. By using both LVS and a camera, calibration techniques are needed in order to maintain a high alignment with the profiling mechanism.

LVS systems require high precision calibration techniques in order to maintain a high ratio of precision in the profiling process. A black box approach calibration technique was devised at previously allocated stand-off locations. This technique disregards the need to measure the camera's intrinsic and extrinsic parameters [35]. The extrinsic parameters are the parameters of the focal lens of the camera in order to bring the image into the camera coordinate system whereas the intrinsic parameters are the internal parameters of the camera, both of which need calibration. Another technique was developed similarly to the black box approach but with the aid of using WT analysis in order to identify surface flaws [46]. The black box approach requires a huge amount of previously allocated information due to the stand-off distances. Also, this approach has not been tested for dimensional accuracy with previously prescribed inputs. Another method uses a calibration technique that captures both the camera and laser plane parameters in a single image [47, 48]. On a further note, simulations showed that both approaches; black box and simple approaches capabilities in measuring and evaluating calibration of the LVS [49]. Moreover, the camera resolution plays a major part in the laser peak detection. Any inaccuracy in the two dimensional image coordinates magnifies based on a scaling factor in the world coordinates [50, 51].

1.5.2 Microwave non-destructive testing

Due to its strong potential in surface profiling, Microwave Non-Destructive Testing (NDT) has been the focus of various research topics. Microwaves, depending on the distance between the source and receiving source, can act differently. The region in which the NDT can be performed is the near field. The waves that are reflected back from any surface in the near field are rich waves and contain a huge amount of information about the surface properties. Though most researchers have discussed the possibility of using this topology in everyday use, direct implementation of the microwave technology is still young for commercial purposes. Most of the research done discusses the possibility of microwave imaging in detecting micro-cracks that fall within the equivalent wave-length range of the microwave [52].

The voltage and phase coming from the reflected wave need to be decoded using non-linear methodologies, such as neural networks, and can give information about the surface properties such as type of material, cracks and or rigidity. Since the system is non-linear, the system must be trained to understand the raw voltage data coming from the signal and transfer it into surface measurements based on many criteria such as

distance between source and surface, permittivity and permeability of the surface [53-55].

Chapter 2: System Overview

The portable surface profiling system consists of two main units: The position tracking unit, and the detection unit as shown in Figure 2.1. The position tracking unit is made of an IMU sensor that integrates a tri-axial accelerometer along with a tri-axial gyroscope. The detection unit, however, is made of any profiling system. The methodology introduced will target the algorithm needed to calculate the position of the detection unit by using the position tracking unit.

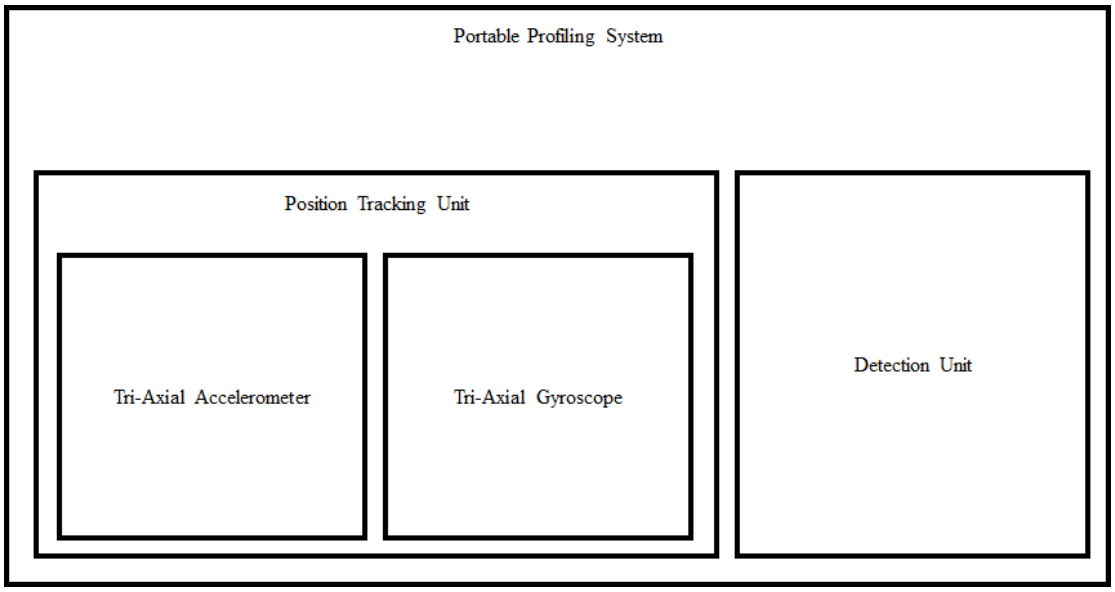

Figure 2.1: System Block Diagram

Knowing the location of the detection unit data in space removes the necessity for using large and bulky systems leading to reduction in cost. Two main detection units are investigated in this research; Laser Vision Sensor profiling system and Microwave NDT profiling system. The main criterion needed for portability is to establish a system that can travel in all axis and rotate freely around the sample profiled. To acquire this freedom in movement, coordinate system transformation must be accounted for.

2.1 Coordinate System Transformation

Transformation (**H)** occurs between different coordinate systems as the system is travelling in space. This movement can be subdivided into two main types of transformation; Rotation (**R)** (3×3) and Translation (**T)** (3×1).

$$\mathbf{H} = \begin{bmatrix} \mathbf{R} & \mathbf{T} \\ \mathbf{0^T} & 1 \end{bmatrix} \tag{2.1}$$

To keep the mathematical model homogeneous, a transposed vector of zeroes and a 1 is needed in order to keep the Transformation a homogenous matrix (4×4).

2.1.1 Orientation adjustment theory

General body motion is usually accompanied with changes in orientation. Any vector rotated along two or more axis introduces components. Figure 2.2 shows a very basic and simple orientation change along both *y* and *z* axes.

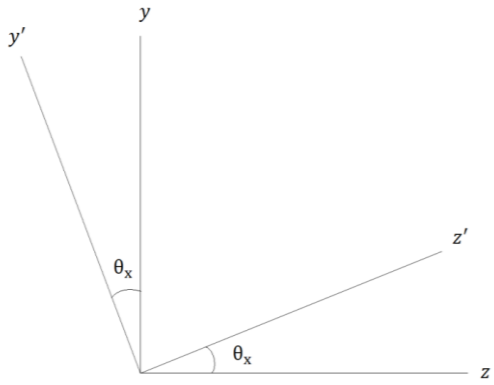

Figure 2.2: Rotation along two axis

If analyzed in three dimensions, the theta corresponding to this change can be expressed as one of the Euler angles of the body. Rotation has to be maintained before translation in order to ensure that the vector being translated is in the same coordinate system of interest. This is done using Euler angles which are obtained in all three axes. Figure 2.3 demonstrates the three Euler angles corresponding to their respective axis.

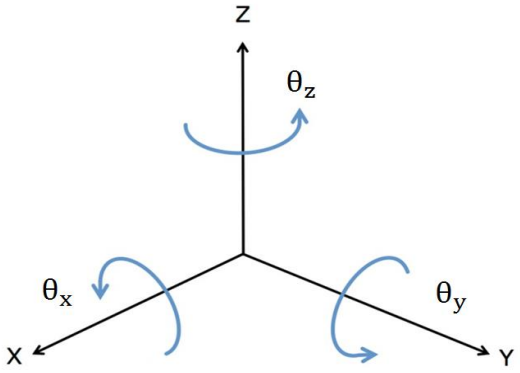

Figure 2.3: Euler Angles

Once those angles are known, a 3×3 rotation matrix is developed for each angle, thus allowing the axis to be rotated from the coordinate system they exhibit into a new coordinate system.

$$\begin{bmatrix} x' \\ y' \\ z' \end{bmatrix} = \mathbf{R}(\theta_x) \begin{bmatrix} x \\ y \\ z \end{bmatrix} \tag{2.2}$$

$$\begin{bmatrix} x' \\ y' \\ z' \end{bmatrix} = \mathbf{R}(\theta_y) \begin{bmatrix} x \\ y \\ z \end{bmatrix} \tag{2.3}$$

$$\begin{bmatrix} x' \\ y' \\ z' \end{bmatrix} = \mathbf{R}(\theta_z) \begin{bmatrix} x \\ y \\ z \end{bmatrix} \tag{2.4}$$

Each of those matrices corresponds to a compounding of components that can occur depending on the angle. Any change in the angle corresponding to the *x*-axis (Roll) causes the vector to have a change in its *y* and *z* components with the *x* component constant. However, any change in the angle corresponding to the *y*-axis (Pitch) causes a change in the *x* and *z* components of the vector with the y component constant. Along the same lines, any change to the angle corresponding to the *z*-axis (Yaw) causes a change in the *x* and *y* components of the vector and the z component constant. In detail, each rotation matrix is shown in Eq. (2.5-2.7).

$$\mathbf{R_x} = \mathbf{R}(\theta_x) = \begin{bmatrix} 1 & 0 & 0 \\ 0 & cos(\theta_x) & sin(\theta_x) \\ 0 & -sin(\theta_x) & cos(\theta_x) \end{bmatrix} \tag{2.5}$$

$$\mathbf{R_y} = \mathbf{R}(\theta_y) = \begin{bmatrix} cos(\theta_y) & 0 & -sin(\theta_y) \\ 0 & 1 & 0 \\ sin(\theta_y) & 0 & cos(\theta_y) \end{bmatrix} \tag{2.6}$$

$$\mathbf{R_z} = \mathbf{R}(\theta_z) = \begin{bmatrix} cos(\theta_z) & sin(\theta_z) & 0 \\ -sin(\theta_z) & cos(\theta_z) & 0 \\ 0 & 0 & 1 \end{bmatrix} \tag{2.7}$$

Since matrix multiplication is not commutative, each sequence of multiplication of those matrices results in a new 3×3 rotation matrix. The selection of the sequence is restricted in the transformation needed and depends on the angle reference. Using the complement of the angle allows the rotation to take place in the opposite direction. Since the data is discrete and is subject to change as a function of time, each vector in the three axis is rotated in order to ensure that all the data is transformed into the coordinate system of interest.

Two sequences are of interest, rotating from the coordinate system *x y z* to coordinate system *x' y' z'* and vise-versa. Eq. (2.8) demonstrates the sequences needed respectively:

$$\mathbf{R}_{\mathbf{xyz}}^{\mathbf{x'y'z'}}(\theta_x, \theta_y, \theta_z) = \mathbf{R}(\theta_x)\mathbf{R}(\theta_y)\mathbf{R}(\theta_z) \tag{2.8}$$

$$\mathbf{R}^{\mathbf{xyz}}_{\mathbf{x'y'z'}}(\theta_{x'}, \theta_{y'}, \theta_{z'}) = \mathbf{R}(-\theta_z)\mathbf{R}(-\theta_y)\mathbf{R}(-\theta_x) \tag{2.9}$$

The matrix resulting in Eq. (2.9) is mathematically the inverse of the matrix in Eq. (2.8) since the determinant of the matrices is equal to 1. Once the rotation transformation is imposed, the data can then be translated to the point of interest.

2.1.2 Translation theory

Since the system is moving, along with rotation, translation takes place as shown in Figure 2.4. The airplane shown travels in one axis in a simple translation.

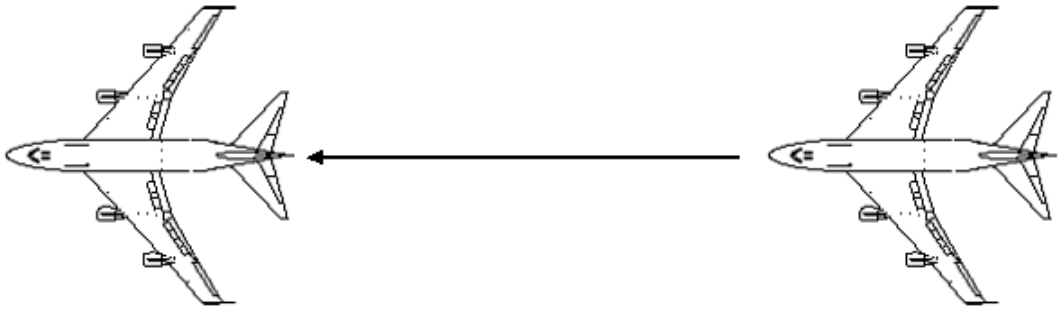

Figure 2.4: Translation

Therefore, another mathematical model is derived in order to compensate for the translation taking place. This is either the movement of the body or a known spacing between the body and another in terms of distance denoted as r.

$$\mathbf{T} = \begin{bmatrix} r_x \\ r_y \\ r_z \end{bmatrix} \tag{2.10}$$

Each component in **T** stands for the change in position or transformation in the same coordinate system.

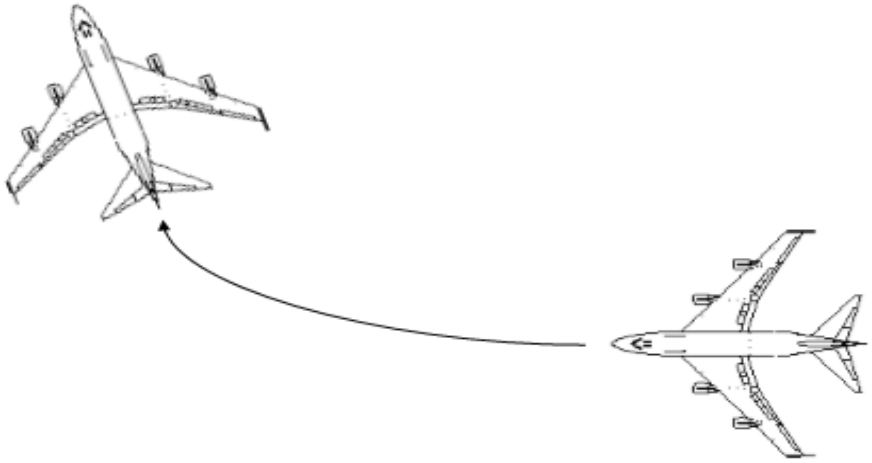

Figure 2.5: Transformation including Translation and Rotation

2.2 Position Tracking Sensor Characteristics

Accelerometers and gyroscopes, like any other sensors, have characteristics that determine the accuracy and viability of the data based on a certain application. In this application, low range due to the small position tracking needed along with high sensitivity with very low noise floor are required.

2.2.1 Dynamic range

Range in any sensor plays a very big role. The range of the data to be acquired for any set of electronics factor out the type of signals is required to be inputted to the sensor. If the range suits the application, the SNR of the device allows the signal to be acquired by the accelerometer and gyroscope. Otherwise, if the signal is too faint, the signal will be seen as noise. Relatively, if the signal is too high, the sensor output will be nonlinear and will eventually output high amplitude data with no meaning. For acquiring distance in centimeter range, a low range sensor is required in order to read the faint signal coming from the hand movement. An accelerometer range is defined by the multiples of gravity it can read.

2.2.2 Sensitivity

Accelerometers measure acceleration as a form of vibration in piezoelectric devices or as a measure of capacitance in capacitive devices which is later calibrated across voltage in the device. Therefore, the sensitivity of the device is a very important aspect to notice when selecting the accelerometer is needed. Sensitivity is a measure of the change in acceleration in terms of vibration or capacitance in ratio with the change of voltage corresponding to it. The higher the sensitivity of the device, the better the device is at monitoring small changes in acceleration. Moreover, to capture higher resolution data relative to small acceleration changes, a higher sensitivity accelerometer is required. Also, the sensitivity and SNR in the gyroscope is required to be extremely high, mainly due to the small changes in the angles per second in the measurement.

2.3 Integration of the System

The coordinate systems play the main role in orienting the data from the detector sensor to the reference point in the world frame coordinate system. The detection data is relative to the detection sensor body frame. The transformation technique discussed previously is required to bring this data from the detection coordinate system into the IMU sensor coordinate system. Once this is maintained, another transformation

technique is implemented to bring the IMU sensor coordinate system into the world coordinate system relative to the user. The overall transition between the coordinate system is summarized in Eq. (2.11).

$$\begin{bmatrix} x_d \\ y_d \\ z_d \\ 1 \end{bmatrix} = \Phi(\mathbf{I}|\mathbf{0})\ \mathbf{H_s^d}\ \mathbf{H_w^s} \begin{bmatrix} x_w \\ y_w \\ z_w \\ 1 \end{bmatrix} \tag{2.11}$$

Those transformations will be analyzed in depth. The $\mathbf{H_w^s}$ is a 4×4 matrix in Eq. (2.11) which represents the transformation needed on the data coming from the IMU sensor and the transformation needed to bring the data from the IMU sensor coordinate system into the world coordinate system representing the reference point. On the other hand, $\mathbf{H_s^d}$ represents a 4×4 matrix which is used to maintain the transformation needed to bring the IMU sensor coordination system to the detection coordinate system, depending on the geometry of the system and the spacing between both units. This transformation, unlike the first transformation, is a fixed transformation with time because the units are not changing orientation or distance in reference to each other. Another factor is the correction factor Φ which is a 3×3 matrix involving the characteristics of the detection sensor. It varies from one detection sensor to another. Chapter 3 will discuss the world to IMU sensor conversions which are time varying and chapter 4 will discuss the transformation from IMU sensor to detection sensor coordinate systems which are fixed along with the correction factors involved based on the system of detection being used.

2.4 The Kalman Filter

The Kalman Filter is an extremely strong tool that compares the calculated data across the measured data and outputs the optimal values based on the Kalman Gain. The Kalman Gain in turn changes accordingly based on what to trust from the predicted or measured data. The predicted data is the integration of the gyroscope angular rate whereas the measured data is the accelerometer angle calculations. As the gain changes, the Kalman Filter decides on what data to trust and output the results with the minimal data bias available. This is done by estimating the error and trying to reduce it from the system as a Gaussian white noise. This will allow the angular position estimation to take advantage of both the gyroscope and accelerometer measurements with less noise contribution [18, 56-68].

The Kalman Filter is a mathematical model that allows the system to reduce the noise on the assumption that the noise is Gaussian. Given that *k* is the time step of the scan, the Kalman Filter's main equations depend on $\mathbf{w}(k)$ which is the noise in the process variable and $\mathbf{v}(k)$ which is the noise in the measurement variable, both of which are white.

$$\hat{\mathbf{x}}(k) = \mathbf{A}\mathbf{x}\,(k-1) + \mathbf{B}\,\mathbf{u}(k) + \mathbf{w}(k) \tag{2.12}$$

$$\mathbf{z}(k) = \mathbf{H}\,\hat{\mathbf{x}}(k) + \mathbf{v}(k) \tag{2.13}$$

The Kalman Filter's main focus is to reduce those noises and estimate the best fitting state of the system. The Kalman Filter operates based on two layers; the time update layer and the measurement update layer. The time update layer works as a predictor in which the calculations take place while the measurement update layer works as a corrector and a comparator that compares between the predicted value and the measurement value coming directly from the measurements.

2.4.1 Time update layer

The time update layer tries to estimate the state of the system based on the physical behavior of the system. The state $\hat{\mathbf{x}}$ is estimated based on the control variable $\mathbf{u}$ and the previous state value $\mathbf{x}\,(k-1)$ by using the system physical matrices $\mathbf{A}$ and $\mathbf{B}$ for the system and control respectively.

$$\hat{\mathbf{x}}(k) = \mathbf{A}\mathbf{x}\,(k-1) + \mathbf{B}\,\mathbf{u}(k) \tag{2.14}$$

Therefore, an initial value for the state $\mathbf{x}\,(0)$ must be known beforehand to guide the process in later stages. Based on the known initial value and its certainty, the initial value for the error $\mathbf{P}(0)$ must also be set. This value depends highly on how accurate the initial value is. For example, if the initial value is not a good guess, then the error vector $\mathbf{P}(0)$ should be high and vise-versa. As a result, the new error vector is estimated based on how far the estimation is from the previous state. This depends highly on the expected value of the Gaussian noise w(k) and its expected value [13, 62].

$$\mathbf{E}[\mathbf{w}(k)\mathbf{w}^{\mathbf{T}}(k)] = (0, \mathbf{Q}) \tag{2.15}$$

$$\widehat{\mathbf{P}}(k) = \mathbf{A}\,\mathbf{P}(k-1)\,\mathbf{A}^{\mathbf{T}} + \mathbf{Q} \tag{2.16}$$

Once the estimated state and error vectors are calculated for the new time step, the update layer takes control of the process. In turn, $\mathbf{Q}$ is the covariance in the process noise.

2.4.2 Measurement update layer

Based on how good the estimation was in the previous layer, the update layer or correction part of the filter takes action into trying to compare and correct the estimations. This mainly rotates around the Kalman Gain which is a function of the error vector and the expected value of the noise in the measurement data $\mathbf{v}(k)$.

$$\mathbf{E}[\mathbf{v}(k)\mathbf{v}^{\mathbf{T}}(k)] = (0, R) \tag{2.17}$$

This in turn leads to the calculation of the Kalman Gain.

$$\mathbf{K}(k) = \widehat{\mathbf{P}}(k)\,\mathbf{H}\left(\mathbf{H}\,\widehat{\mathbf{P}}(k)\,\mathbf{H}^{-\mathbf{1}} + R\right) \tag{2.18}$$

The Kalman Gain in turn directs the system into choosing which values to trust. In other words, the system has to choose whether to trust the estimation or the measurement based on the noise available in both the process and measurement noise variables. Before referring to the Kalman Gain's influence, the measurement comes from two places; either from the estimation values or another source of measurement. If there is no measurement source, the measurement values corresponding to $\mathbf{z}(k)$ are calculated using the estimated state at the current time step.

$$\mathbf{z}(k) = \mathbf{H}\,\hat{\mathbf{x}}(k) \tag{2.19}$$

The measurement values can come from two sources; either an external measurement taken by another technique or a computed measurement. This in turn proves to be more accurate because the filter deals with an external source to validate its estimations.

$$\mathbf{z}(k) = e(k) \tag{2.20}$$

Once the measurement update is calculated, the Kalman Gain acts as a guidance to the difference between the estimation and the measurement, and it superimposes it on the estimation.

$$\mathbf{x}(k) = \hat{\mathbf{x}}(k) + \mathbf{K}\big(\mathbf{z}(k) - \mathbf{H}\,\hat{\mathbf{x}}(k)\big) \tag{2.21}$$

Moreover, the Kalman Filter prepares itself to the next time step by calculating the new error vector which replaces the previous error vector. The new error vector depends on the old one along with the Kalman Gain.

$$\mathbf{P}(k) = (\,\mathrm{I} - \mathbf{K}\,\mathbf{H}\,)\,\widehat{\mathbf{P}}(k) \tag{2.22}$$

Figure 2.6 shows the algorithm that the Kalman Filter uses for a better estimation of the system state.

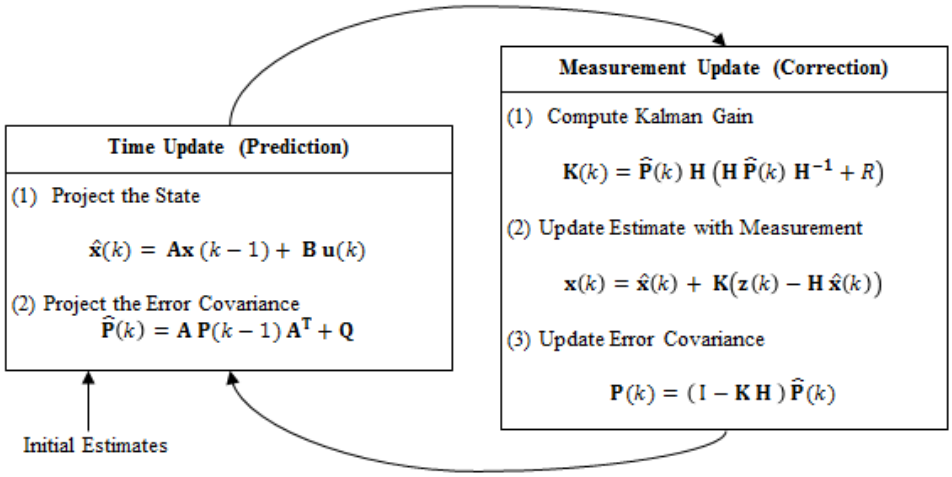

Figure 2.6: Kalman Filtering Algorithm

Chapter 3: Position Tracking

Position Tracking Unit is made up of the IMU sensor which is an integrated sensor made up of a tri-axial accelerometer along with a tri-axial gyroscope. The tri-axial accelerometer inputs data as raw accelerations in all three axes, whereas the gyroscope measures the angular rate of the system.

The position tracking algorithm consists of many subsections based on extraction of data from both sensors, allocating the orientation which pours into the rotation matrices associated with the algorithm to calculate the position and estimate the location of the sensor at any given time (k). Therefore, this chapter will tackle the algorithm associated in order to estimate:

1. Orientation
2. Gravity Calculation
3. Gravity Removal
4. Acceleration Rotation and Position Estimation

The tracking algorithm can be summarized in the flow chart presented in Figure 3.1.

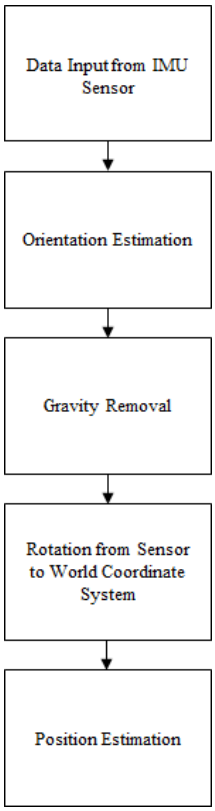

Figure 3.1: Position Tracking

3.1 IMU Sensor Input Data

Given the fact that gravity acts as an acceleration that is fixed in magnitude but can subdivide into components, the accelerometer will measure it along with the movement acceleration of the system. Therefore, an algorithm is required to remove the gravity components in order to end up with the acceleration due to dynamic movement of the sensor.

$$\mathbf{a_s} = \mathbf{a_{sm}} + \mathbf{a_{sg}} \tag{3.1}$$

$$\boldsymbol{\omega_s} = \begin{bmatrix} \omega_{sx} \\ \omega_{sy} \\ \omega_{sz} \end{bmatrix} \tag{3.2}$$

The vector $\mathbf{a_s}$ corresponds to the total acceleration coming from the accelerometer in the IMU sensor coordinate system with subscript s. The vector $\mathbf{a_{sm}}$ corresponds to the acceleration due to the body movement in the IMU sensor coordinate system. The vector $\mathbf{a_{sg}}$ refers to the acceleration due to the gravity components in the IMU sensor coordinate system. The vector $\boldsymbol{\omega_s}$ corresponds to the total angular rate relative to the angular position change of the sensor in the IMU sensor coordinate system.

$$\mathbf{a_{sm}} = \begin{bmatrix} a_{smx} \\ a_{smy} \\ a_{smz} \end{bmatrix} \tag{3.3}$$

$$\mathbf{a_{sg}} = \begin{bmatrix} a_{sgx} \\ a_{sgy} \\ a_{sgz} \end{bmatrix} \tag{3.4}$$

To locate the position of the sensor, $\mathbf{a_{sm}}$ needs to be extracted in an algorithm that depends on sensor fusion between the accelerometer and gyroscope. Also, some filtering techniques will be discussed to enhance the algorithm proposed along with other mathematical derivations to reduce the noise associated with the measurements coming from both sensors due to their high bias drift.

3.2 Orientation

The orientation of the system can be measured using both the accelerometer and gyroscope data, and also by using a technique called sensor fusion to calculate a more accurate result. In this section, a simple measurement was done to demonstrate the different techniques and compare them versus each other. The measurement was taken as the IMU sensor was rotated 80 degrees around the *y*-axis, i.e. Pitch.

3.2.1 Accelerometer orientation algorithm

Since gravity components exist in the acceleration with a resultant equal to Earth's gravity which equals $9.81\ \mathrm{m/s^2}$, the system orientation can be calculated using the accelerometer acceleration values that correspond to the gravity components. The gravity components in turn determine the orientation of the system in space and therefore the corresponding angles at which the sensor is oriented with. However, these angles are only limited to the angles along the *x* and *y* axes (Roll and Pitch) whereas the angle along the *z*-axis (Yaw) can have infinitely many solutions keeping in mind that gravity components will not change based on the rotation along the *z*-axis. This is in line with the fact that gravity exists only in the z axis in the world coordinate system.

$$\mathbf{a_{wg}} = \begin{bmatrix} 0 \\ 0 \\ -g \end{bmatrix} \tag{3.5}$$

The vector $\mathbf{a_{wg}}$ is a vector corresponding to the gravity acceleration in the world coordinate system. The rotation across any axis as a result is as shown in Eq. (3.6).

$$\mathbf{a_{sg}} = \mathbf{R_w^s}(\theta_x, \theta_y, \theta_z)\mathbf{a_{wg}} = -g \begin{bmatrix} -sin(\theta_y) \\ sin(\theta_x)cos(\theta_y) \\ cos(\theta_x)cos(\theta_y) \end{bmatrix} \tag{3.6}$$

Given that the accelerometer supplies the data as a linear combination between the movement acceleration and gravity acceleration, it is extremely hard to decompose the values of gravity components from the acceleration input. Luckily, since gravity exists, nevertheless, a digital low pass filter can decompose the signal into gravity and movement but more on that will be touched in later sections of this chapter. The following equations can derive the Roll and Pitch angles directly from the accelerometer readings using the nonlinear functions S_x and S_y. The angles will be represented with a subscript **a** in order to distinguish them from the angles to be calculated from the gyroscope.

$$\theta_{xa} = S_x(a_{sx}, a_{sy}, a_{sz}) = tan^{-1}\left(\frac{a_{sy}}{a_{sz}}\right) \tag{3.7}$$

$$\theta_{ya} = S_y(a_{sx}, a_{sy}, a_{sz}) = tan^{-1}\left(\frac{a_{sx}}{\sqrt{{a_{sy}}^2 + {a_{sz}}^2}}\right) \tag{3.8}$$

Once Roll and Pitch are calcualted using Eq. (3.7-3.8), a digital low pass filter is introduced to the angles calculated in order to remove the noise and the movement acceleration. Figure 3.2 summarizes the algorithm required in order to calculate the orientation based on the accelerometer acceleration data.

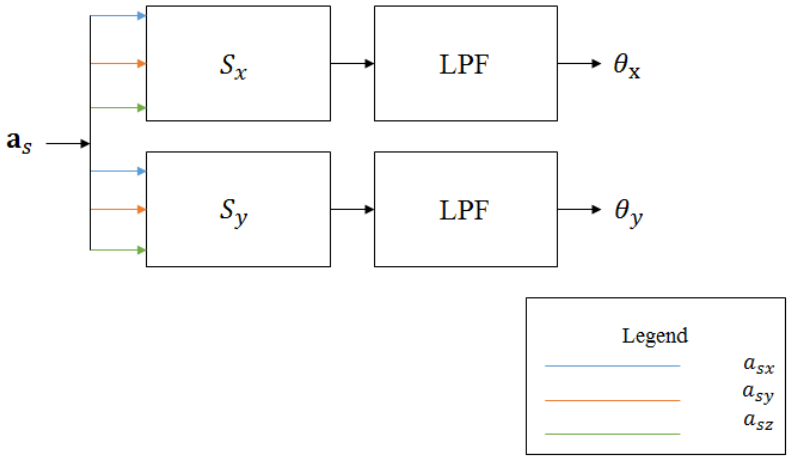

Figure 3.2: Accelerometer Orientation Algorithm

The accelerometer maintains a good accuracy in orientation calculation. However, the angles are extremely noisy on the short run. However, the longer the run of the accelerometer, the better the estimation fo the orientation calculation of the acceleroemter [3, 16-18, 20, 59, 62, 65, 67, 69].

3.2.2 Gyroscope orientation algorithm

The gyroscope as mentioned previously measures the revolution speed of the system in all three axes, therefore integrating the angular speed results in the angular position which is translated to the Euler angles across all three angles; Roll, Pitch and Yaw.

$$\theta = \int \omega \, dt \tag{3.9}$$

This statement is correct if the system is rotating along one axis only. However if the system is rotating along different axes at the same instant, a rotation technique **D** is required in order to change the angular speed from the IMU sensor coordinate system into the world coordinate system. This rotation is summarized in Eq. (3.10) [13].

$$\boldsymbol{\omega_s} = \begin{bmatrix} \omega_{wx} \\ 0 \\ 0 \end{bmatrix} + \mathbf{R}(\theta_x) \begin{bmatrix} 0 \\ \omega_{wy} \\ 0 \end{bmatrix} + \mathbf{R}(\theta_x)\mathbf{R}(\theta_y) \begin{bmatrix} 0 \\ 0 \\ \omega_{wz} \end{bmatrix} \tag{3.10}$$

As Eq. (3.10) suggests, the *x*-axis rotational speed is aligned with the world coordinate system, however for *y*-axis and *z*-axis, that does not hold and is subject to the rotations that are occurring in the other axis, such as y depends on rotation made in *x* and *z* depends on rotations made in *x* and *y* as well. The inverse of Eq. (3.10) is present in Eq. (3.11).

$$\boldsymbol{\omega_w} = \mathbf{D}(\theta_x, \theta_y)\boldsymbol{\omega_s} = \begin{bmatrix} 1 & sin(\theta_x)tan(\theta_y) & cos(\theta_x)tan(\theta_y) \\ 0 & cos(\theta_x) & -sin(\theta_y) \\ 0 & \frac{sin(\theta_x)}{cos(\theta_y)} & \frac{cos(\theta_x)}{cos(\theta_y)} \end{bmatrix} \begin{bmatrix} \omega_{sx} \\ \omega_{sy} \\ \omega_{sz} \end{bmatrix} \quad (3.11)$$

Once this is achieved, the rotational speeds are now ready to be integrated in order to calculate the world coordinate Euler angles in all three axes. Since the rotation matrix $\mathbf{D}(\theta_x, \theta_y)$ is dependent on Roll and Pitch, the angles calculated from the previous iteration are substituted into the rotation in order to calculate the new angles. This method has some error due to using the previous angles. However, based on the high sampling frequency, the previous angles are most likely extremely close to the new angles being calculated. Once the angular speed in the world coordinate system is calculated, integrating the data is done using the First Order Forward Finite Difference Method as in Eq. (3.12).

$$\theta(k+1) = \theta(k) + \Delta t \times \boldsymbol{\omega}(k) \quad (3.12)$$

$$\Delta t = T_s = {}^{1}/_{f_s} \quad (3.13)$$

Figure 3.3 summarizes the algorithm required to calculate the orientation based on the gyroscope data. Due to the integration associated with the algorithm, a huge bias drift error results as the system is running and angles calculated with the gyroscope alone are extremely inaccurate. Therefore, on the long run, a gyroscope alone fails to sustain reasonable measurements of the angles of orientation [70].

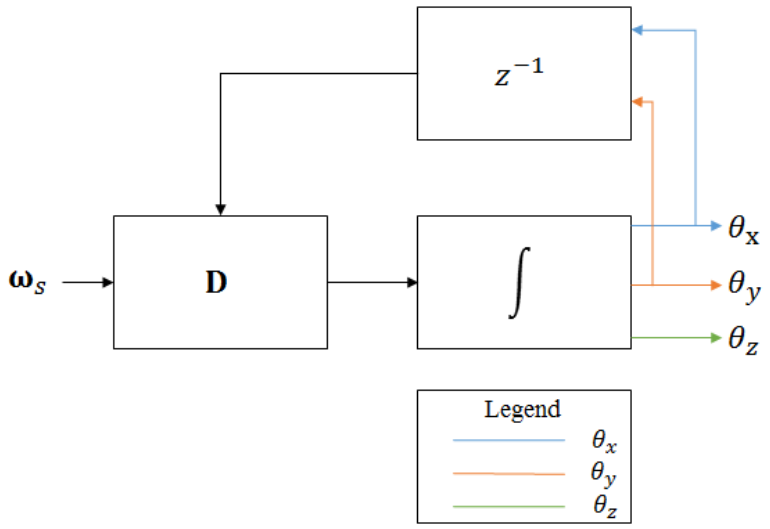

Figure 3.3: Gyroscope Orientation Algorithm

The subscript g refers to the angles calculated from the gyroscope data. Given the problems available in both the gyroscope and accelerometer orientation calculations, sensor fusion has been viable with high success and accuracy.

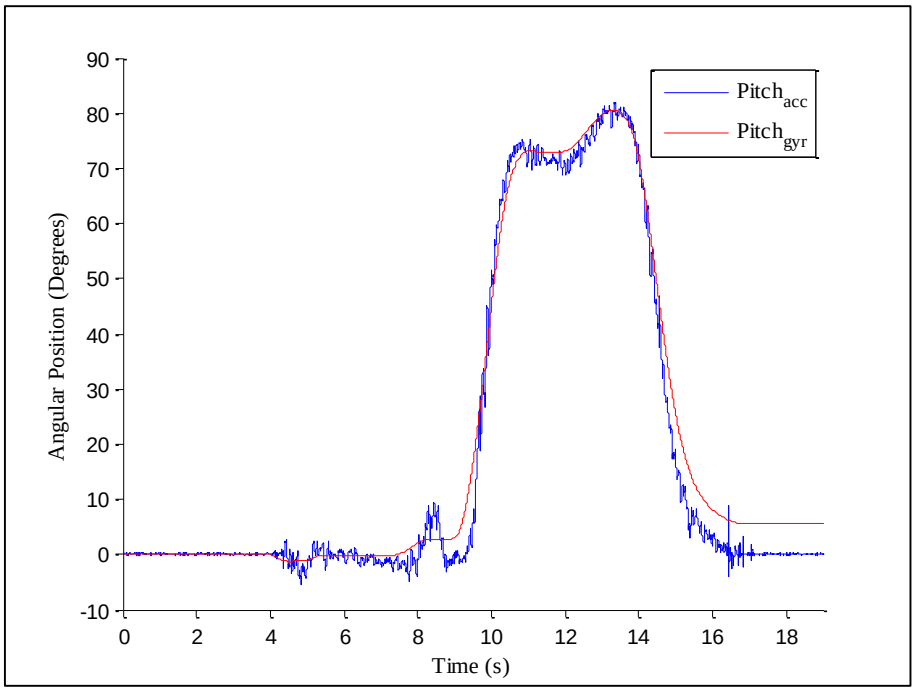

Figure 3.4: Gyroscope vs. Accelerometer Orientation in Pitch

Figure 3.4 compares the Roll values coming from the accelerometer versus those from the gyroscope integration. As shown, the accelerometer data are less stable when compared to the gyroscope data. However, the accelerometer Roll is precise whereas the gyroscope data is drifting with time and deviating from the true values as shown at the end of the measurement.

3.2.3 Sensor fusion: orientation accuracy

Sensor Fusion can be achieved by introducing a type of filtering that can compare both sources of angles i.e. accelerometer and gyroscope calculated angles. Unfortunately, since Yaw cannot be calculated using the accelerometer data, the error in Yaw is reduced poorly when compared to both Roll and Pitch. Sensor fusion can be maintained in two main methodologies; Kalman and Complementary Filtering.

3.2.3.1 Orientation Kalman Filter

The state matrix simplifies, as shown in Eq. (3.14) to unity whereas the control state matrix is the time step of the system. The measured variable is the angular velocity coming from the orientation matrix $\mathbf{D}(\theta_x, \theta_y)$ as per Eq. (3.15).

$$\mathbf{A} = 1 \tag{3.14}$$

$$\mathbf{B} = \Delta t \tag{3.15}$$

The estimated values $\mathbf{x_k}$ correspond to the angles being calculated using the state equations. Since the Kalman Filter can input and output one axis, three Kalman Filters are imposed on the system in order to estimate and predict the changes in all three angles. However, the three filters have to be integrated together in order to allow for $\mathbf{D}(\theta_x, \theta_y)$ to rotate the angular velocities from the IMU sensor coordinate system to the world coordinate system. The control variable $\mathbf{u_k}$ corresponds to the angular velocities coming from gyroscope data after the rotation process.

$$\hat{x}_x(k) = x_x(k-1) + \Delta t\, \omega_{wx}(k) \tag{3.16}$$

$$\hat{x}_y(k) = x_y(k-1) + \Delta t\, \omega_{wy}(k) \tag{3.17}$$

$$\hat{x}_z(k) = x_z(k-1) + \Delta t\, \omega_{wz}(k) \tag{3.18}$$

The measured data is the angle as per the accelerometer data. However, for the Yaw calculations since the accelerometer data cannot be transformed into Yaw domain, the measured data is correspondent to the gyroscope Yaw calculations. The state matrix for the measured variable **H** is equal to unity as well.

$$\mathbf{H} = 1 \tag{3.19}$$

The measured variable, on the other hand, is the angles calculated from the accelerometer readings as shown in section 3.2.1.

$$z_x(k) = \theta_{ax}(k) \tag{3.20}$$

$$z_y(k) = \theta_{ay}(k) \tag{3.21}$$

$$z_z(k) = \theta_{gz}(k) \tag{3.22}$$

To start the iterations across the filter, other parameters are needed to take care of the Gaussian noise assumed. Two noise parameters, which correspond to the process noise and measurement noise covariance, are involved. The measurement noise covariance corresponds to the signal coming from the accelerometer.

$$R = {\sigma_a}^2 \tag{3.23}$$

Based on the standard deviation of the angular rate, the process noise distribution on the angle calculation Q is dependent upon the standard deviation of the angular rate, however since the angular position of the Euler angles is integral of angular rate. The following relationship is applied.

$$\mathbf{Q} = {\sigma_\omega}^2 \Delta t \tag{3.24}$$

Figure 3.5 shows the algorithm used for the Kalman Filter by combining both the accelerometer and the gyroscope inputs. This flow chart is per step unit of time and the cycle repeats for newer inputs.

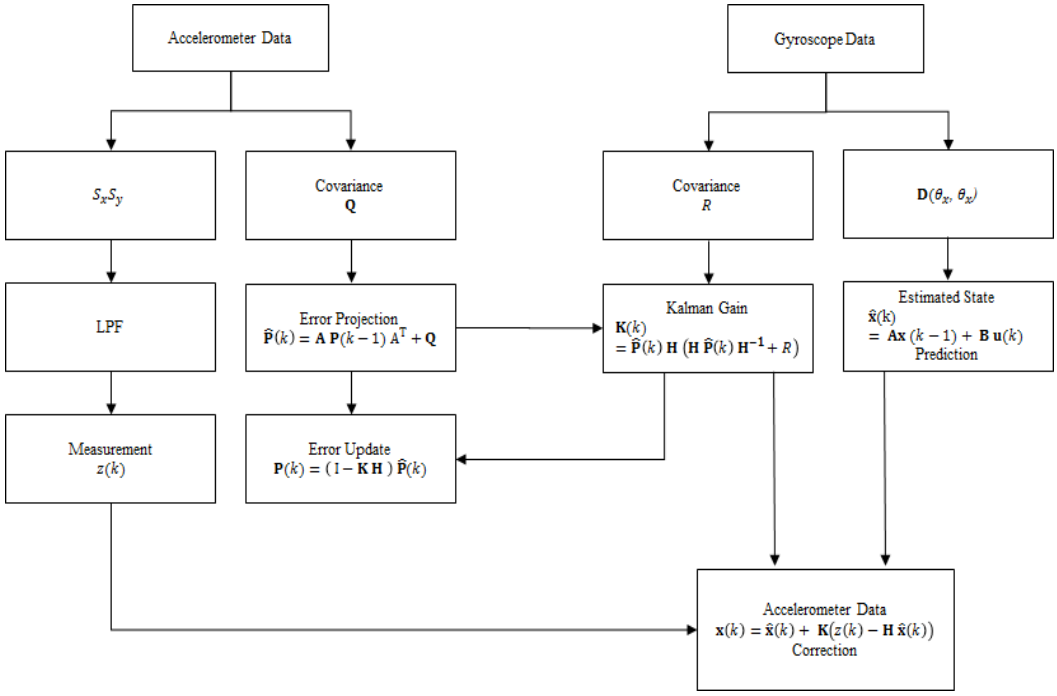

Figure 3.5: Sensor Fusion: Kalman Filter

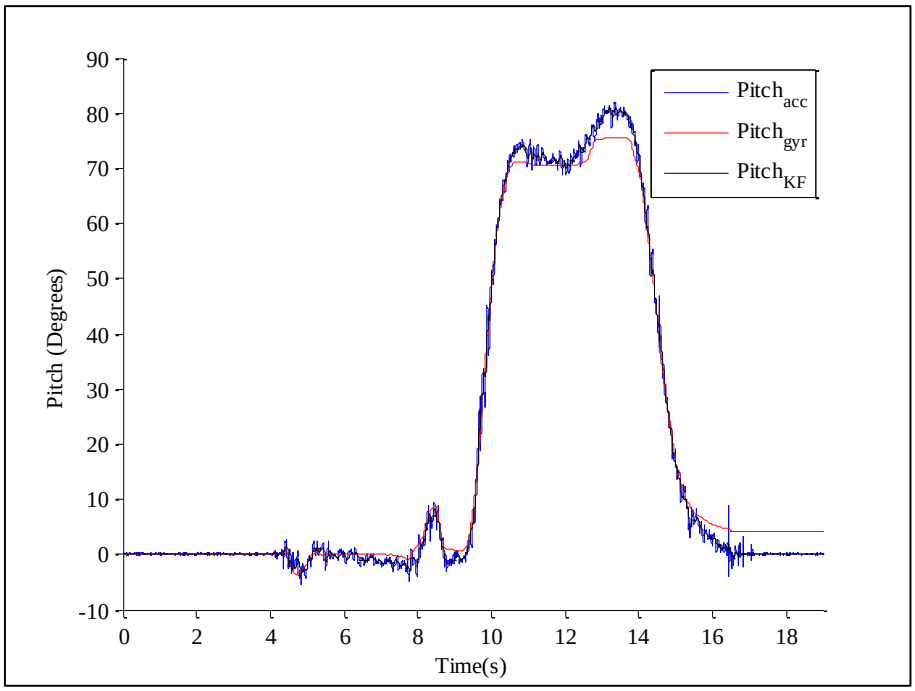

Figure 3.6: Accelerometer & Gyroscope vs. Kalman

As Figure 3.6 shows, the Kalman Filter managed to take the best out of both readings. The Kalman output signal (in black) did not drift with time and is less noisy than that of the accelerometer Roll values.

3.2.3.2 Orientation Complementary Filter

The Complementary Filter is another filter that can be imposed on the orientation algorithm to allow for a less noise response and a more accurate output with the minimal drift bias error. Unlike the Kalman Filter, this filter is simpler both computationally and analytically, however, with less accurate results when compared to the Kalman Filter. Based on the fact that accelerometer's data being accurate on the long run and the gyroscope data being accurate on the short run. The Complementary Filter allocates the weights according to the time that the system has been running for [69, 71, 72]. Figure 3.7 demonstrates the algorithm associated.

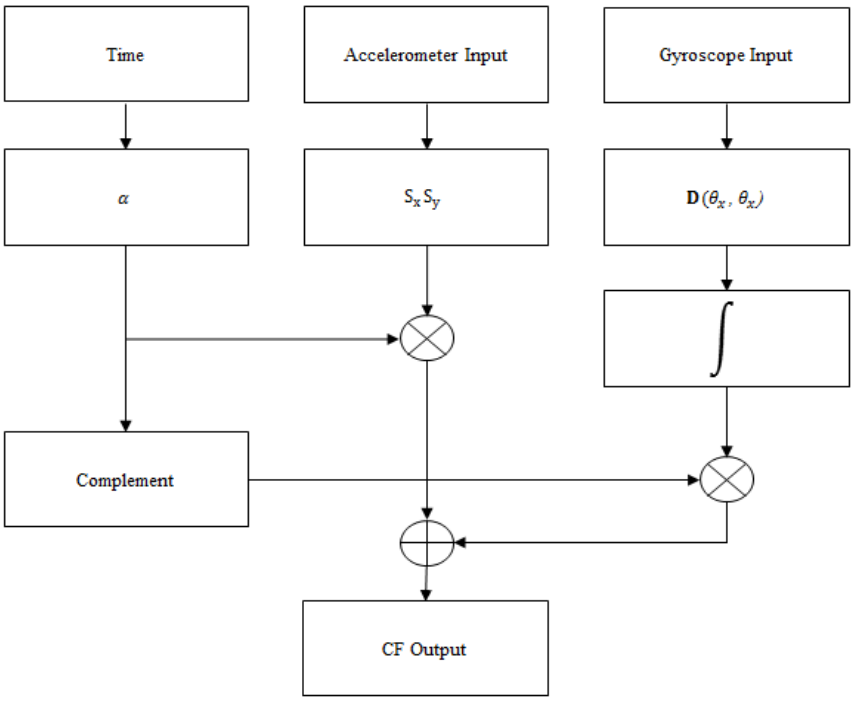

Figure 3.7: CF Block Diagram

However, the complementary filter cannot be imposed on the Yaw readings mainly due to a lack of another source other than the gyroscope. The Complementary Filter's weight α is defined in Eq. (3.26).

$$L\,(k) = L\,(k-1) + \Delta t \tag{3.25}$$

$$\alpha = \frac{Total\ Time}{Total\ Time + L\,(k)} \tag{3.26}$$

The total output of the Complementary Filter is a combination between both angle calculations.

$$\theta_{CFx} = \alpha\,\theta_{gx} + (1-\alpha)\theta_{ax} \tag{3.27}$$

$$\theta_{CFy} = \alpha\,\theta_{gy} + (1-\alpha)\theta_{ay} \tag{3.28}$$

Similar to the Kalman Filter, each filter can calculate only one angle at a time, therefore two Complementary Filters are imposed on the system in order to calculate Roll and Pitch. In the case for Yaw, since the accelerometer cannot supply a Yaw orientation due to the gravity components not being dependent on it, the gyroscope calculation is taken as the only measurement. Also, the Complementary Filter depends on iterations in time domain, however does not depend on the values of error from the previous step but rather combines the gyroscope and accelerometer data rather simply with reasonable estimations that are of extreme accuracy. The advantage that the Complementary Filter presents is the simplicity in the algorithm reducing the computational expense and lag of the system. Figure 3.8 shows how the weight shifts the accelerometer angle calculations and gyroscope angle calculations into the output. The weights being dependent on the time gives priority to the gyroscope data and reducing it to half by the end of the measurement.

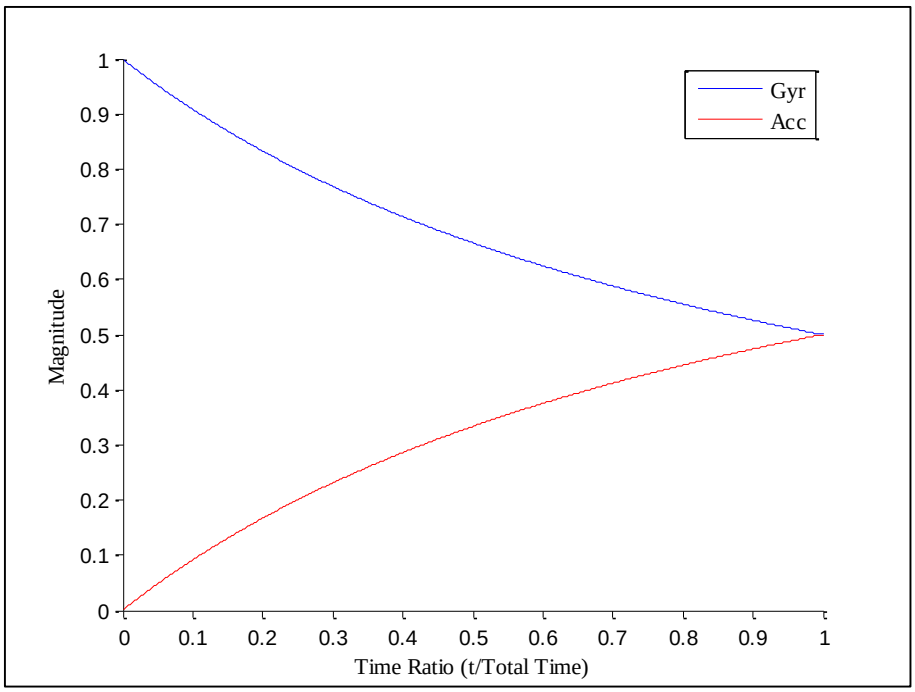

Figure 3.8: Dependency on Values from Gyroscope and Accelerometer CF

Complementarily, the accelerometer angles increase in weight to half at the end of the measurement. The Complementary Filter output managed to combine the less

noisy signal from the gyroscope and a close to zero bias drifting capabilities of the accelerometer data to a more accurate and less noisy output as shown in Figure 3.9.

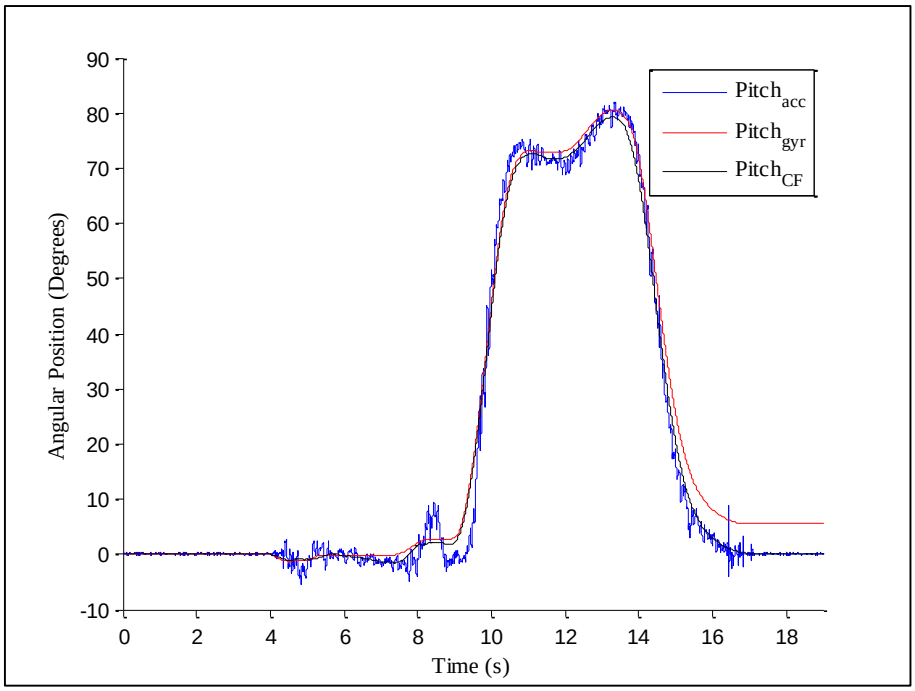

Figure 3.9: CF vs. Accelerometer and Gyroscope

3.2.3.3 Orientation filtering comparison

When compared to the Kalman filter, the Complementary Filter depends only on the time elapsed on the sensor and changes the weights exponentially, whereas the Kalman filter chooses automatically the best fitting data. Therefore, for a very lengthy run of the sensor, the Kalman filter is a better approach than the complementary filter.

Table 3.1: Comparison: Orientation Assisting Filtering Techniques

	Complementary Filter	**Kalman Filter**
Error	High in Yaw	Low in Yaw
Roll	Very accurate	Very accurate
Pitch	Very accurate	Very accurate
Yaw	High Bias	Bias exists but reduced noise
Computational Cost	Low due to Simplicity	High

Also, the Kalman filter estimates yaw more accurately than the complementary filter because it removes the assumed Gaussian noise whereas the complementary filter

has the gyroscope data as its only input. A comparison drawn between both methods is shown in Table 3.1 in terms of error, corresponding angles, and computational costs.

3.2.4 Reference orientation calculations

The reference point is the point that the sensor starts from ($k = 0$). Given that the sensor could be at any random orientation, this orientation needs to be corrected for in order to accurately transform the data from the sensor coordinate system into the world coordinate system. Though the reference point holds accelerations equal to zero, gravity components will still be present in different weighted coefficients in the three axis unlike in the world coordinate system where gravity is only present in one axis.

Initially at the reference point, the accelerometer will record acceleration data purely due to the gravity components present due to the orientation of the sensor when the scan starts.

$$\mathbf{a_s}(0) = 0 + \mathbf{a_{sg}}(0) = 0 + \begin{bmatrix} g_x \\ g_y \\ g_z \end{bmatrix} \tag{3.29}$$

Since the gyroscope measures the change of the orientation, it assumes that the starting point is always at zero and therefore shows only the deviation. However, the accelerometer can be used to calculate the orientation at the starting point due to the gravity components presence. One problem faced though, is that the Yaw cannot be calculated from the accelerometer. Another sensor is required in order to calculate the initial Yaw angle. The magnetometer is used to calculate Yaw in the literature by using the polarity of the sensor in reference to the Earth's North Pole. However, in the presence of any magnetic material such as motors or generators, the magnetometer fails tremendously. Also, another problem that the magnetometer imposes to the application intended in this research is the fact that the Earth's North Pole should be known prior to running the profiling sequence. In most cases, knowing the direction of the North Pole is not only inaccessible but is also meaningless. Therefore, the referencing point to the system in Yaw will be set to zero and the change in the orientation is calculated on forth.

$$\theta_x(0) = tan^{-1}\left(\frac{a_{sy}(0)}{a_{sz}(0)}\right) \tag{3.30}$$

$$\theta_y(0) = tan^{-1}\left(\frac{a_{sy}(0)}{\sqrt{a_{sy}(0)^2 + a_{sz}(0)^2}}\right) \tag{3.31}$$

$$\theta_z(0) = \text{Based on the Starting Yaw Inputted by the User} \tag{3.32}$$

Once all the angles at the reference point are calculated, the orientation that the sensor started from is formulated and each new orientation that the sensor takes throughout the measurement can be corrected by the reference angles.

3.3 Gravity Estimation

The Euler angles at every point in time are known to the system which allows the system to extract the gravity components from the acceleration values coming from the accelerometer. Moreover, having the Euler angles at every time step locates the orientation of the sensor. This however requires a good estimate of the Euler angles along with a mechanism in order to reduce the noise present in the accelerometer's readings. Two main ways to estimate gravity present in the acceleration data come from the IMU sensor.

3.3.1 Gravity estimation using rotation calculations

Once the Euler angles are calculated from the gyroscope, the acceleration data is cleaned from the gravity components. To do so, the gravity components in the IMU sensor coordinate system needs to be estimated at every time step. Hence, the world gravity vector $\mathbf{a_{wg}}$ consisting of only one gravity component only present in the *z*-axis is rotated into the sensor coordinate system at every time step and subtracted from the accelerometer data as shown in Eq. (3.33).

$$\mathbf{a_{sg}} = \mathbf{R_w^s}(\theta_x, \theta_y, \theta_z)\mathbf{a_{wg}} \tag{3.33}$$

The result of this is $\mathbf{a_{sg}}$ representing a matrix that represents all the gravity components coming from the accelerometer in all axis.

3.3.2 Gravity estimation using LPF

Going back to Eq. (3.1), in order to extract $\mathbf{a_{sg}}$, a closer look is required on the Fourier of the signal coming from the accelerometer.

$$\mathbf{A_{sg}}(f) = H_{LPF}(f)\,\mathbf{A_s}(f) \tag{3.34}$$

Since gravity exists in every coordinate system, the frequency that its magnitude appears at is at a very low value. Therefore, a LPF is required in order to extract the gravity components present in the sensor coordinate system as shown in Figure 3.10. In contrary, the movement of the sensor signal is present at higher frequencies and thus a HPF is required.

In the following spectrum analysis, Fourier Transform was calculated for the data coming from the accelerometer. The measurement was divided into three main stages. The data was sampled at a frequency of 100 Hz by using the mobile phone accelerometer sensor. The range of the mobile accelerometer is $+/-\ 5g$ present in iPhone 5S. The average of the frequency response of all 10 trials was taken and plotted in Figure 3.11 and are summarized in Table 3.2.

Table 3.2: Trial Based Validation

	Gravity in X	**Gravity in Y**	**Gravity in Z**	**Random**
Trials	10	10	10	10
Orientation	Constant	Constant	Constant	Variable
Movement	Automated	Automated	Automated	Manual

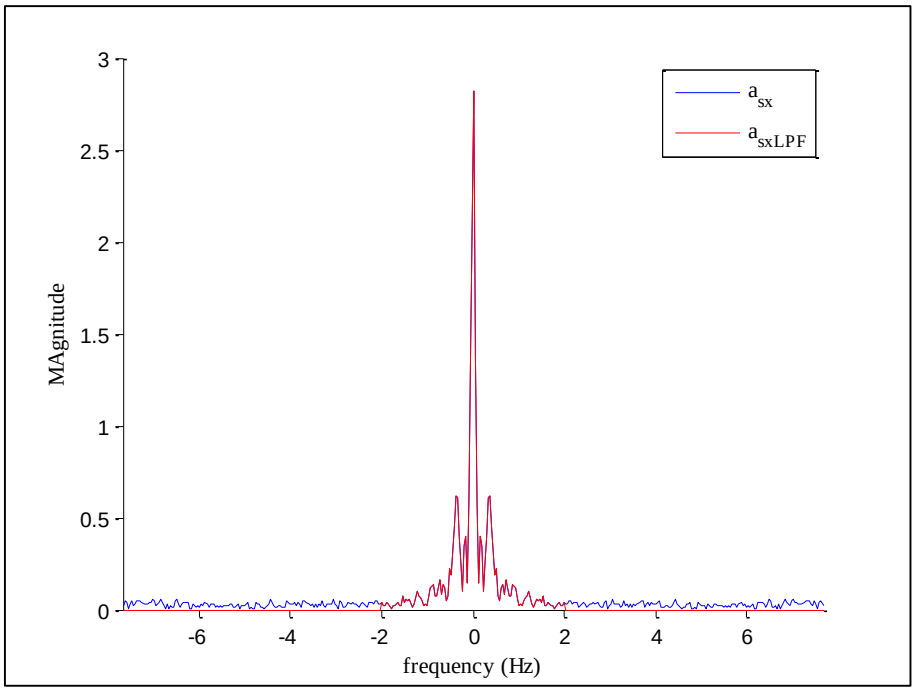

Figure 3.10: Frequency Spectrum for Gravity Components

The test has shown that gravity is dominant at low frequencies whereas any motion acceleration that is introduced on the system exhibits higher frequencies which in turn attributes that gravity always exhibits low frequencies in the spectrum of the acceleration data.

The gravity component showed dominance at 0 Hz are summarized in Table 3.3. The sensor was moved in the *x* direction where Table. 3.3 shows that it had the

lowest peak value at low frequencies. This in turn allows the reduction of error bias that also exists at low frequencies.

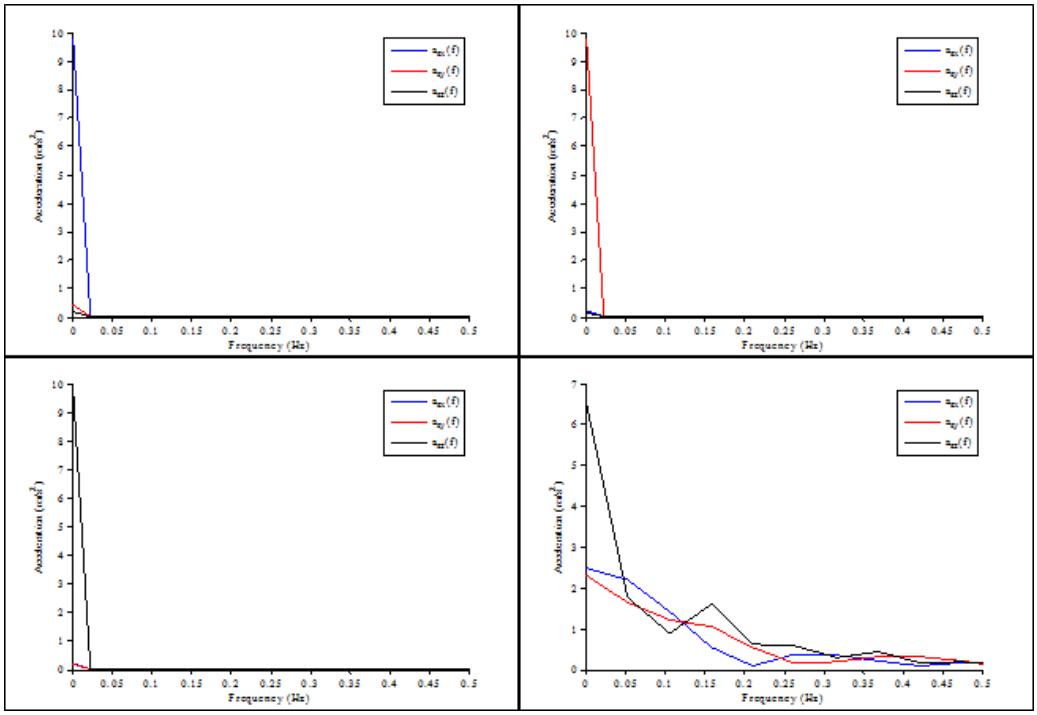

Figure 3.11: Positive Frequency Spectrum for Gravity Component
in (top left) *x*-axis (top right) *y*-axis (bottom left) *z*-axis (bottom right) random

Table 3.3: Peak Values for DC Components

$@\ f = 0\ Hz$		**Peak Values** (m/s^2)
Gravity in *x*-axis	$\lvert a_{sx}(f) \rvert$	9.78
	$\lvert a_{sy}(f) \rvert$	0.41
	$\lvert a_{sz}(f) \rvert$	0.19
Gravity in *y*-axis	$\lvert a_{sx}(f) \rvert$	0.22
	$\lvert a_{sy}(f) \rvert$	9.75
	$\lvert a_{sz}(f) \rvert$	0.16
Gravity in *z*-axis	$\lvert a_{sx}(f) \rvert$	0.21
	$\lvert a_{sy}(f) \rvert$	0.19
	$\lvert a_{sz}(f) \rvert$	9.78
Random	$\lvert a_{sx}(f) \rvert$	2.49
	$\lvert a_{sy}(f) \rvert$	2.30
	$\lvert a_{sz}(f) \rvert$	6.49

While the calculation method estimates gravity relatively accurately, it does not in turn account for bias drift. As a result, a combined mechanism is introduced to take the advantages of both methodologies.

3.3.3 Combining both methods

The previous methods that estimate the gravity components in the IMU sensor coordinate system are both combined to produce the best possible outcome in terms of better accuracy and less both bias and noise errors. Using an averaging method between the two produces the best fit data.

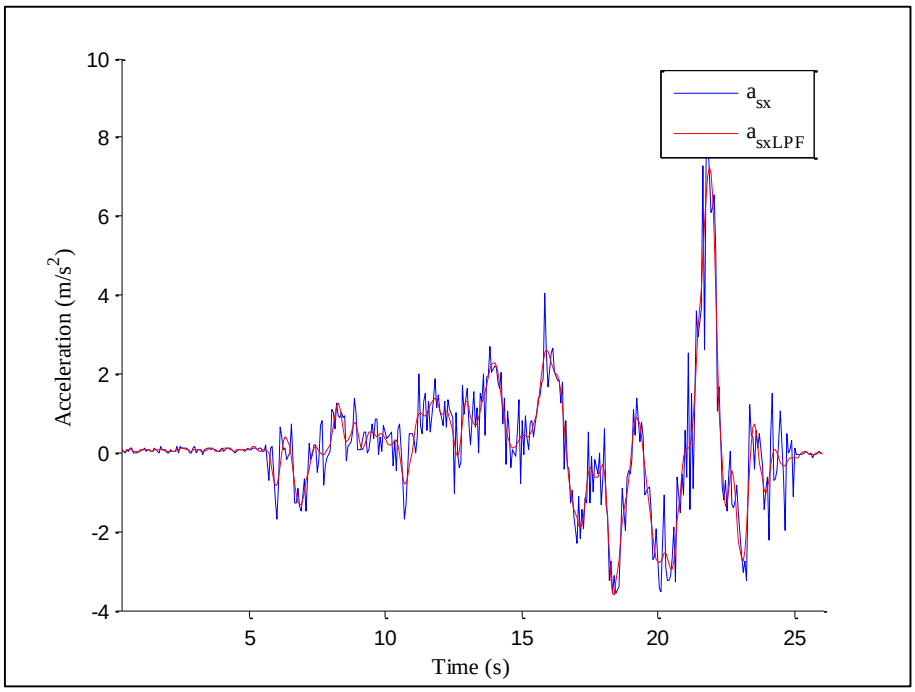

Figure 3.12: Gravity Extraction: Signal vs. LPF

Figure. 3.12 shows the output from using both methods to estimate the gravity components in the IMU sensor coordinate system. As shown, the results are extremely close with the LPF output being a little higher in amplitude. This is because some of the error is extracted, and as can be seen, most of the error accumulates as time is increasing mainly due to the motion that has occurred.

3.4 Gravity Removal

Once gravity components in the sensor coordinate system are estimated, they are removed from the original signal since the only acceleration needed to calculate the distance covered is resembled within the motion acceleration. The acceleration data coming from the accelerometer is a linear superposition as shown in Eq. (3.1). Thus, a

linear subtraction is needed to remove the gravity components. However, since the gravity components are a good estimate, what is left is the motion acceleration along with noise and bias drift.

3.4.1 Motion acceleration using rotation calculations

Neglecting the noise and bias drift data, the subtraction performed to remove the gravity components is as follows.

$$\mathbf{a_{sm}} = \mathbf{a_s} - \mathbf{a_{sg}} \tag{3.35}$$

Once this is performed, what is left is a good estimate of the motion in all three axes in the IMU sensor coordinate system. In later sections, the coordinate system is rotated to estimate position relative to the use, i.e. the world coordinate system.

3.4.2 Motion acceleration using HPF

A complement methodology to the one used to extract gravity components from the original signal $\mathbf{a_s}$ is by using a HPF. A HPF can extract the motion acceleration from the input data coming from the accelerometer at high frequencies as shown in Figure 3.13. Similar to the extraction of the gravity components, the motion acceleration exhibits the IMU sensor coordinate system.

$$\mathbf{A_{sm}}(f) = H_{HPF}(f)\,\mathbf{A_s}(f) \tag{3.36}$$

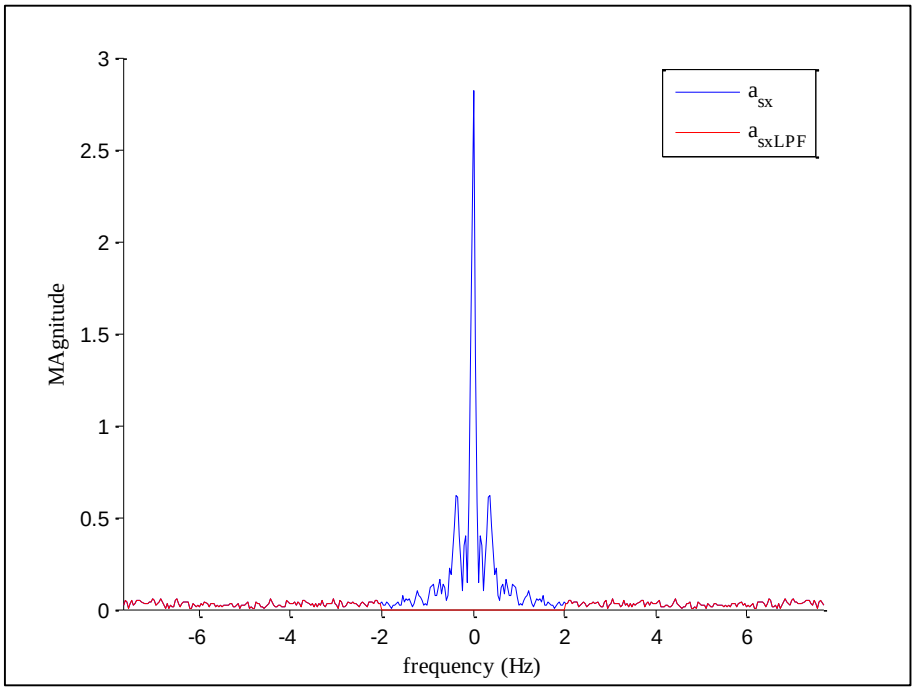

Figure 3.13: Frequency Spectrum for motion acceleration

The advantage of using a HPF is the noise reduction it can impose on the acceleration values. Frequencies that are high correspond to the movement acceleration

made by a hand or a motor movement. Since acceleration of the proposed system can never achieve values higher than that of gravity.

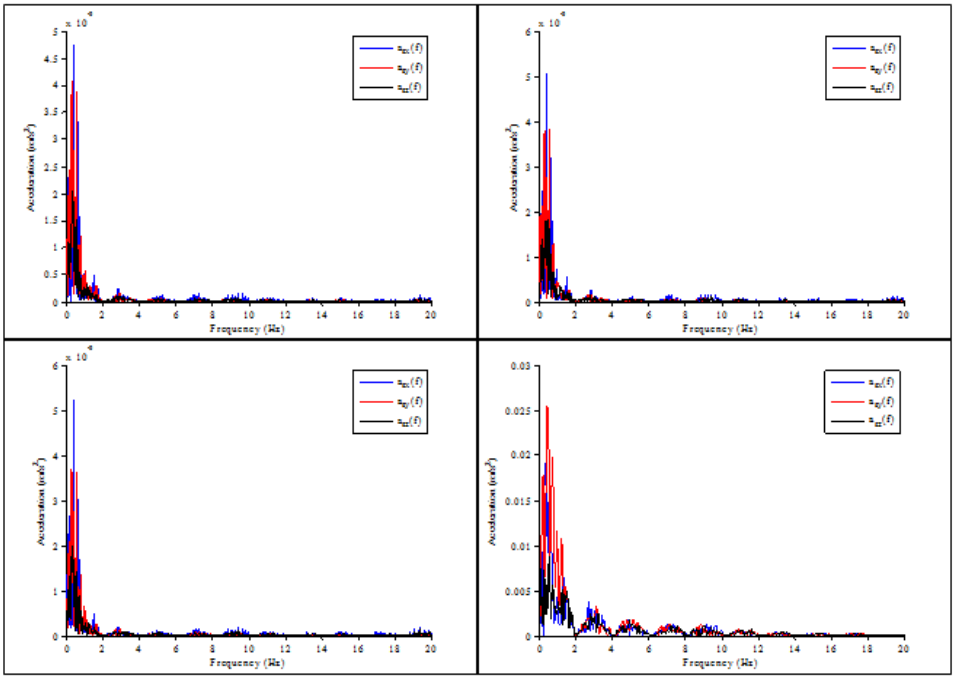

Figure 3.14: Positive Frequency Spectrum for Gravity Component in (top left) *x*-axis (top right) *y*-axis (bottom left) *z*-axis (bottom right) random after motion calculations and removal of gravity

Table 3.4: Peak Values for DC Components

$@\ f = 0\ Hz$		**Peak Values** (m/s^2)
Gravity in *x*-axis	$\lvert a_{sx}(f)\rvert$	1.73 e -18
	$\lvert a_{sy}(f)\rvert$	1.58 e -17
	$\lvert a_{sz}(f)\rvert$	3.75 e -17
Gravity in *y*-axis	$\lvert a_{sx}(f)\rvert$	3.78 e -20
	$\lvert a_{sy}(f)\rvert$	2.33 e -20
	$\lvert a_{sz}(f)\rvert$	5.63 e -16
Gravity in *z*-axis	$\lvert a_{sx}(f)\rvert$	5.23 e -17
	$\lvert a_{sy}(f)\rvert$	1.21 e -17
	$\lvert a_{sz}(f)\rvert$	1.66 e -18
Random	$\lvert a_{sx}(f)\rvert$	2.14 e -17
	$\lvert a_{sy}(f)\rvert$	1.02 e -16
	$\lvert a_{sz}(f)\rvert$	7.69 e -17

The same test was applied to the accelerometer's readings, but with a hand movement on it. After calculating the rotation and removal of the gravity components, the magnitudes of the DC values are recorded in Table 3.4 and shown in Figure 3.14. As shown, the DC values were removed completely from the signal and the small magnitudes that are at higher frequencies which were negligible due to high magnitudes from gravity in the frequency domain are now visible and contain he motion of the sensor.

3.4.3 Combining both methods

The dominating high magnitudes coming from the gravity components are removed from the signal as shown in Figure 3.15. Estimating the motion acceleration by using a HPF reduces the noise in the signal but also allows for reduced magnitudes and loss of some of the signal whereas the calculation method gives out a more accurate signal, with high bias error. Therefore, combining both results in a better output in both accuracy and noise ratios.

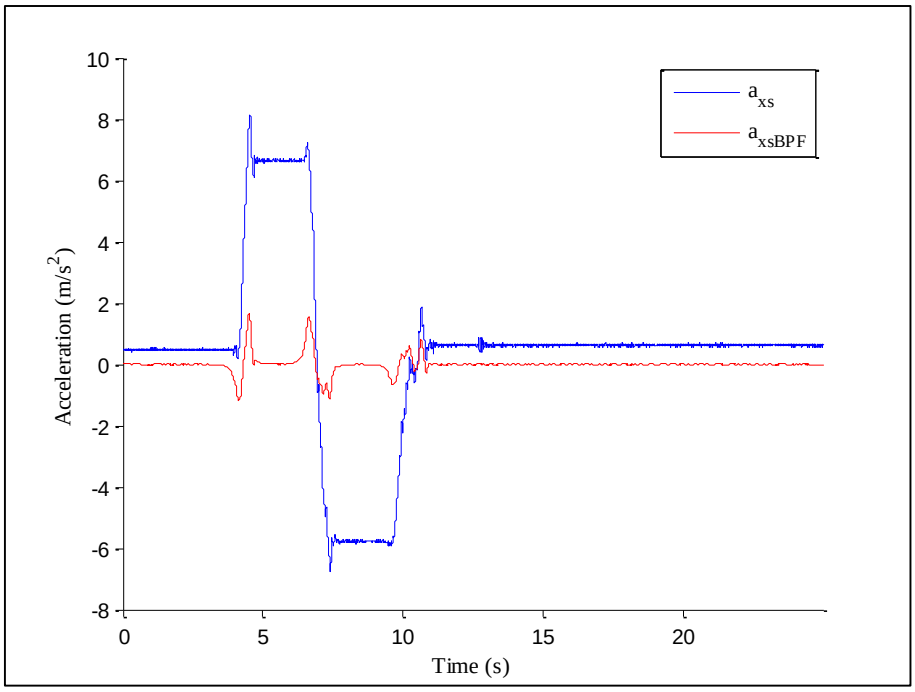

Figure 3.15: Motion Extraction: Calculated vs. HPF *x*-axis

3.5 Velocity and Position Estimation

Since the gravity is removed, the acceleration values represented in $\mathbf{a_{sm}}$ are then transformed into the world coordinate system in order to calculate the displacement

over the time that the sensor has travelled. This is performed by using the inverse of the rotation matrix used to calculate the gravity components as shown in Eq. (3.37).

$$\mathbf{a_{wm}} = \mathbf{R_s^w}(\theta_x, \theta_y, \theta_z)\mathbf{a_{sm}} \tag{3.37}$$

The acceleration of the movement is rotated into the world coordinate system. The acceleration data represented in $\mathbf{a_{wm}}$ which is a matrix consisting of 3 rows corresponds to the axis accelerations and columns equal to the time steps of the scan. The acceleration values in the world frame coordinate system go into displacement calculations similarly to how the angles were calculated, however with the use of double integration in this case since the displacement is the second derivative of acceleration.

$$r = \int \int a\, dt^2 \tag{3.38}$$

Likewise, the integration used in order to calculate the displacement is a finite difference time domain.

$$\mathbf{v}(k) = \mathbf{v}(k-1) + \Delta t \times \mathbf{a}(\mathrm{k}) \tag{3.39}$$

$$\mathbf{r}(k) = \mathbf{r}(k-1) + \Delta t \times \mathbf{v}(\mathrm{k}) \tag{3.40}$$

$$\Delta t = T_s = {}^{1}/_{f_s} \tag{3.41}$$

Since the reference point is the point the sensor started from, the initial displacement in all three axes is equal to zero and thus the displacement is a function of the acceleration made in all three axes in the world coordinate frame system.

$$\mathbf{v}(0) = 0 \tag{3.42}$$

$$\mathbf{r}(\mathrm{k}) = 0 \tag{3.43}$$

3.5.1 Position Kalman Filter

The state matrix simplifies as shown in Eq. (3.44) whereas the control state matrix is equal to zero. The measured variable is the motion acceleration in the world coordinate system.

$$\mathbf{A} = \begin{bmatrix} 1 & \Delta t & \Delta t^2 \\ 0 & 1 & \Delta t \\ 0 & 0 & 1 \end{bmatrix} \tag{3.44}$$

The estimated values $\mathbf{x_k}$ correspond to the state being calculated using the state equations. Since the Kalman Filter can input and output one axis, three Kalman Filters are imposed on the system in order to estimate and predict the changes in all three position.

$$\mathbf{x_k} = \begin{bmatrix} r(k) \\ v(k) \\ a_w(k) \end{bmatrix} \tag{3.45}$$

The control variable $\mathbf{u_k}$ is zero in this system.

$$\hat{x}_x(k) = \mathbf{A}x_x(k-1) \tag{3.46}$$

$$\hat{x}_y(k) = \mathbf{A}x_y(k-1) \tag{3.47}$$

$$\hat{x}_z(k) = \mathbf{A}x_z(k-1) \tag{3.48}$$

The measured data is the estimated acceleration

$$\mathbf{H} = [0 \quad 0 \quad 1] \tag{3.49}$$

The measured variable, on the other hand, is the acceleration coming from the accelerometer in the world coordinate system.

$$z_x(k) = a_{wx}(k) \tag{3.50}$$

$$z_y(k) = a_{wy}(k) \tag{3.51}$$

$$z_z(k) = a_{wz}(k) \tag{3.52}$$

To start the iterations across the filter, other parameters are needed to take care of the Gaussian noise assumed. Two noise parameters which correspond to the process noise and measurement noise covariance are involved. The measurement noise covariance corresponds to the signal coming from the accelerometer.

$$\mathrm{R} = {\sigma_a}^2 \tag{3.53}$$

Based on the standard deviation of the acceleration, the process noise distribution on the state calculation Q is dependent on the standard deviation of position which in turn is dependent on the acceleration standard deviation. The following relationship is applied.

$$\mathbf{Q} = {\sigma_a}^2 \begin{bmatrix} \frac{\Delta t^5}{20} & \frac{\Delta t^4}{8} & \frac{\Delta t^3}{6} \\ \frac{\Delta t^4}{8} & \frac{\Delta t^3}{3} & \frac{\Delta t^2}{2} \\ \frac{\Delta t^3}{6} & \frac{\Delta t^2}{2} & \Delta t \end{bmatrix} \tag{3.54}$$

3.6 Position Tracking Overall Algorithm

Figure 3.16 summarizes the whole algorithm in the block diagram it presents starting from the input data coming from both the accelerometer and the gyroscope ending up with position estimation of the sensor.

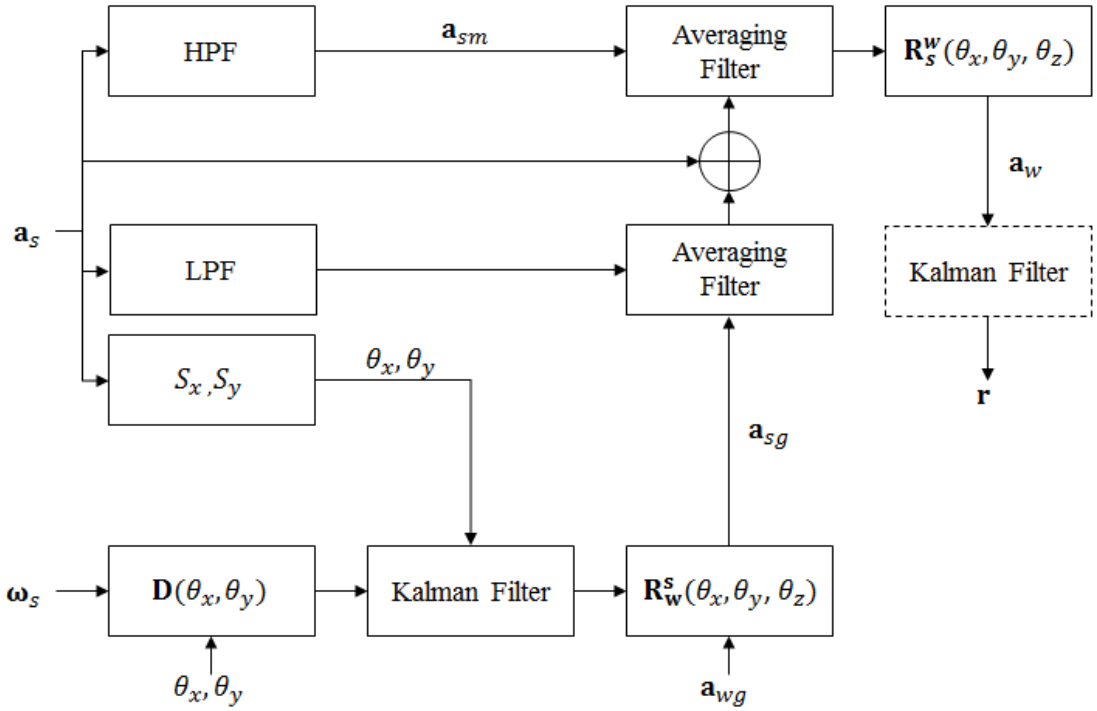

Figure 3.16: Position Tracking System Block Diagram

Chapter 4: Detection Unit Sensor

Microwaves are electromagnetic waves that are restricted by a bandwidth in the frequency spectrum. Microwaves like any waves are subject to both space and time domains. Also, the interaction between two mediums leave its print on the waves propagating. After analyzing mediums and their effects on microwaves, it has come to light that due to medium interactions with the wave, certain mediums can be characterized thoroughly. In this research, surfaces with conductive characteristics are chosen solely due to the fact that they act as short circuits to the microwave trying to propagate in them. This eases the assumption of simple or not simple media and simplifies the matter drastically. The mathematical model of this profiling technique depends on the location of the detection unit. Due to reasons that will be covered later, the microwave detection unit needs not only to be in the near field but also exactly perpendicular to the surface of profile. This simplifies the mathematical model associated to a unity matrix since the calibration is done independently from the system mechanism, however a transformation from the 4D to 3D is required since the detection unit must be perpendicular to the area of interest which is available as it is from the **(I|0).**

$$\Phi = \begin{bmatrix} 1 & 0 & 0 \\ 0 & 1 & 0 \\ 0 & 0 & 1 \end{bmatrix} \tag{4.15}$$

4.1 Theory

Microwaves can be used in certain circuits which allow them to propagate with minimum power loss, i.e. waveguides and co-axials. In this research, the circuit that the microwave is propagating in will act as an antenna in the near field to ensure the minimal loss when the signal is reflected due to the conductive surface. Each medium can be characterized by its intrinsic impedance; a value assigned based on the electric and magnetic characteristics of the material. The reflection coefficient is a measurement of how much of the magnitude of the signal has been reflected back. The reflection coefficient depends completely on the characteristics of the two media and in turn their intrinsic impedances η.

$$\Gamma = \frac{\eta_2 - \eta_1}{\eta_2 + \eta_1} \tag{4.16}$$

In the case of a conductor, the intrinsic impedance of the conductor is equal to zero, i.e. referred to as short circuit and therefore $\Gamma = -1$. When the reflected signal is very close in magnitude to the transmitted signal, a DC offset will emerge as the superposition between both signals. Microwaves are known to have extremely high frequencies i.e. gigahertz and the result is a DC value. As illogical as it may seem, the reflected wave coming back meets the transmitted wave and therefore a constructive or destructive phenomena occurs. Given the fact that the conductive surface reflects all the signal back in theory, the reflected signal meets the transmitted signal and a phenomena called the Standing Wave emerges. The ratio of reflection depends on many factors but those of interest are the distance to the surface, angle at which the profiling occurs, and the shape of the surface.

4.2 Technique

The proposed circuit for microwave profiling mechanism is summarized in Figure 4.1 where the microwave signal is generated by the Gunn-Diode passing through a circulator to maintain the direction of propagation in the circuit which does not allow the reflected signal to go to the source. The signal later passes through the Transmission Line (TL) being a waveguide or a co-axial into the surface.

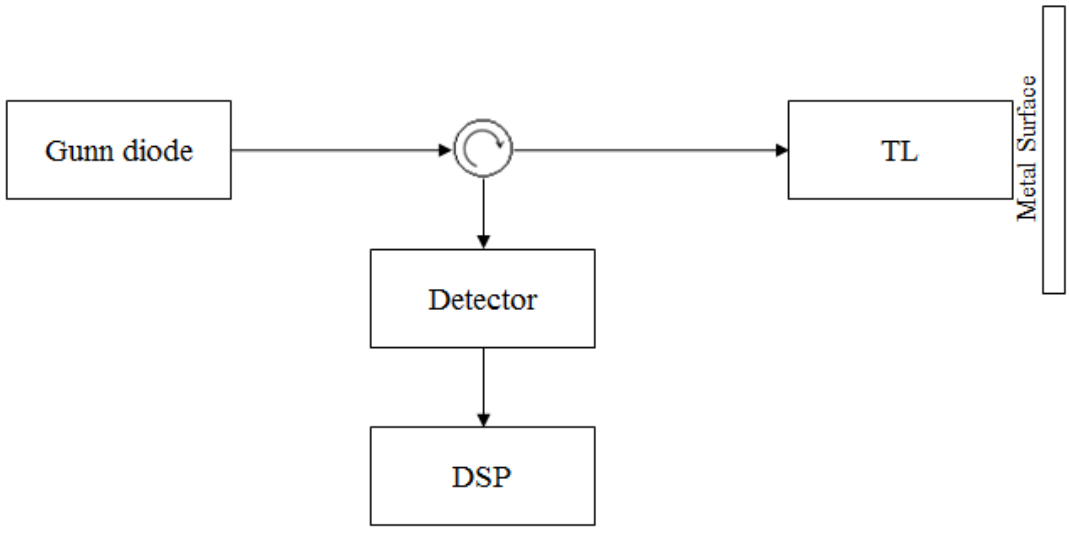

Figure 4.1: Microwave NDT Block Diagram

Depending on the surface that the signal first hits being a conductor or not, some or most of the signal might be reflected back due to the change in characteristics between free space (waveguide or co-axial) and the other media being a conductor or

any surface. The advantage present with having a conductor is that close to all the signal is reflected back into the Waveguide/Co-axial. Once the signal enters the circuit again this time as an input, it goes back through the circulator which guides it into the diode detector. The diode detector acts as a demodulator or LPF which extracts low frequencies and then feeds them into the DSP section.

4.3 Characteristics of the Technique

The sensor must be perpendicular to the surface profiled or else the reflected signal will not be measured. Therefore, an oblique angle is not recommended at the interface for the signal will not be captured by the Waveguide/Co-axial. Another main configuration required is the distance to the surface; for the sensor must be in the near field. The near field of the detection unit is calculated based on the frequency used which is in turn relative to the wavelength of the antenna i.e. Waveguide/Co-axial.

$$d < \frac{2\,D^2}{\lambda} \tag{4.17}$$

Where D is the largest dimension of the antenna and λ is the wavelength of the antenna corresponding to the frequency of operation. Therefore, d must be less in order for the antenna to operate in the near field. Another criterion required is the transformation between the Microwave detection unit and the IMU sensor unit $\mathbf{H_s^d}$. The whole algorithm is summarized in Eq. (4.18).

$$\begin{bmatrix} x_u \\ y_u \\ 1 \end{bmatrix} = \Phi(\mathbf{I}|\mathbf{0})\mathbf{H_s^d} \begin{bmatrix} x_s \\ y_s \\ 0 \\ 1 \end{bmatrix} \tag{4.18}$$

Where the transformation matrix also depends on rotation and translation.

$$\mathbf{H_s^d} = \mathbf{H_s^m} = \begin{bmatrix} \mathbf{R_s^m} & \mathbf{T_s^m} \\ \mathbf{0^T} & 1 \end{bmatrix} \tag{4.19}$$

This matrix will vary significantly if the detection is based on a Waveguide detection methodology or a Co-axial detection methodology. That is mainly due to the physical differences between the two detection methodologies.

4.4 Detection Data and Analysis

The data detection was done using a K-band waveguide which was automatically moved across a metal bar with three smooth horizontal cracks. The data was taken in one axis across the bar vertically. As shown in Figure 4.2, the data can

locate the crack or change of surface heights and the difference is quite visible. When the crack is first noticed by the waveguide, an overshoot in the magnitude of the voltage difference between the transmitted and reflected waves. This is due to the sudden change in depth that the wave is seeing at the beginning of the crack. As the waveguide moves along the crack, this high magnitude then reduces to a lower magnitude indicating that the waveguide is sensing the bottom of the crack. This in turn will induce close to full reflection and a DC output. However, this DC magnitude is still larger than the values appearing when the crack is not visible. This is due to the depth of the crack being farther away from the waveguide when compared to the metal surface with no crack.

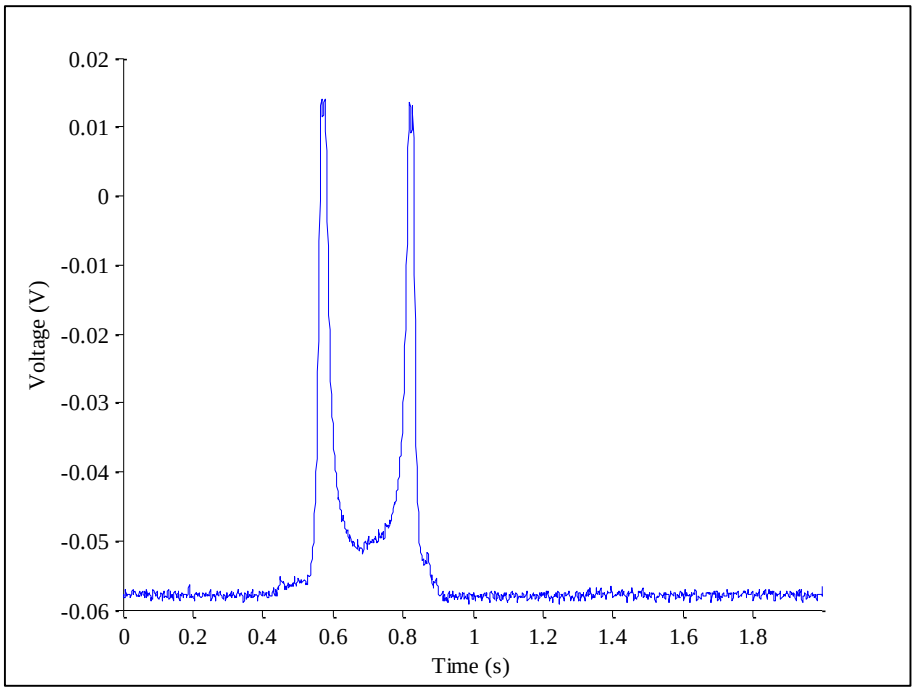

Figure 4.2: Microwave NDT Signal Output for Crack Detection

Microwave NDT was tested for crack detection in this experiment, however, as the plot shows, it is capable of showing a change in surface height along with width and also ultimately change of surface material along the scan. This can also be used in the process of profiling.

Chapter 5: Application of Position Tracking

Using the mathematical models presented in chapter 3, the sensor predicts the initial orientation angles present in the system and rotates the measured accelerations accordingly into the world coordinate system to extract the position measurements. In this chapter, the IMU sensor was operated on the basis of three main approaches summarized in Table 5.1. Each approach is divided into different initial orientations to ensure consistency in the results. The three approaches are done by moving the IMU sensor by using a scanner motor, and using a servo setup.

Table 5.1: Experimental Program

Setup Approach	**Motion**	**Objective**
Scanner Motorized	Motorized	Translation
Angular Position	Manual	Rotation and Translation

The IMU sensor used for the testing is the ADIS16362BMLZ with sampling frequency equal to 819 Hz. Another feature is its low range allowing the slow movement coming from the scanning methodology to be captured.

5.1 Scanner Motorized Movement

To test the translation capabilities of the algorithm, a motorized methodology is required to be carried. The motorized motion is needed to compare the overall displacement of the sensor to the overall displacement of the setup in all three axes.

5.1.1 Equipment and program

The scanner is made up of three identical motors - National Instruments Model AKM21C-ANBNC-00 - and three controllers to control it – National Instruments Model UMI-7774. The scanner is programmed using LabVIEW allowing the three motors to operate in all three axes independently of each other. Program specifications are altered allowing the controllers to guide the scanner in a specific motion pattern. The coordinate system of the scanner is aligned with the world coordinate system but mismatched with the polarity in both *x* and *z* axes.

$$\begin{pmatrix} x_{sc} \\ y_{sc} \\ z_{sc} \end{pmatrix} = \begin{pmatrix} -x_w \\ y_w \\ -z_w \end{pmatrix} \tag{5.1}$$

5.1.2 Scanning motion pattern

The overall pathway for the scan is a $2 \times 6 \times 4$ cm grid, with 2 cm indexes in all axes. The motion starts with consecutive increments in the *x*-axis followed by increments in the *y*-axis. Once the overall distance covered in the *y*-axis is 6 cm, the scanner goes back to the starting point and increments in the *z*-axis to repeat the process. Upon covering an overall distance of 4 cm in the *z*-axis, the scanning ends as shown in Figure 5.1.

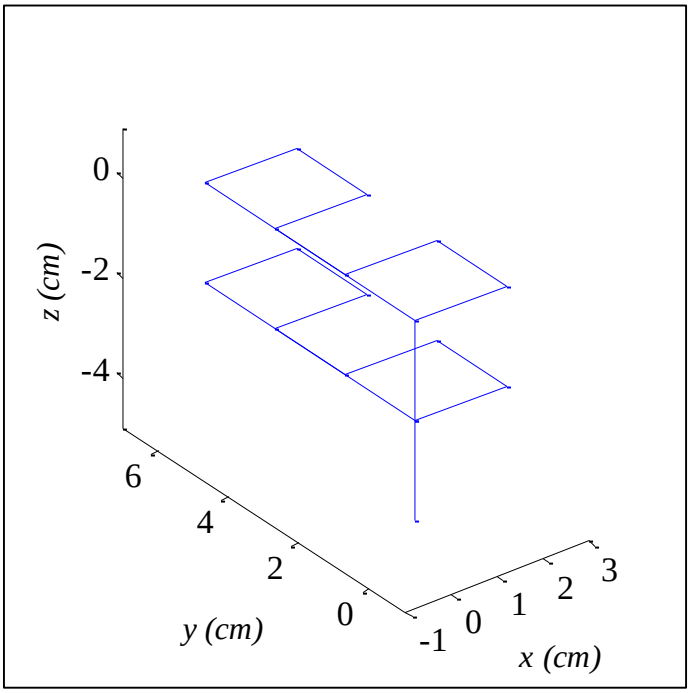

Figure 5.1: Expected Scanning Pattern

A top view of the motion pattern, as shown in Figure 5.2, offers an insight into the pattern in the *x*-*y* plane. Illustration is expected to show an identical overlap with regards to the *z*-axis, demonstrating that motion in both *x*-*y* planes is identical. The scanning pattern has 8 increments in the *x*-axis with half being positive and the other half being negative. Similarly, it had 8 increments in the *y*-axis, yet 2 only were negative with triple the increment size and 6 were standard 2 cm increments. Finally, 2 increments in the negative *z*-axis were included in the scan.

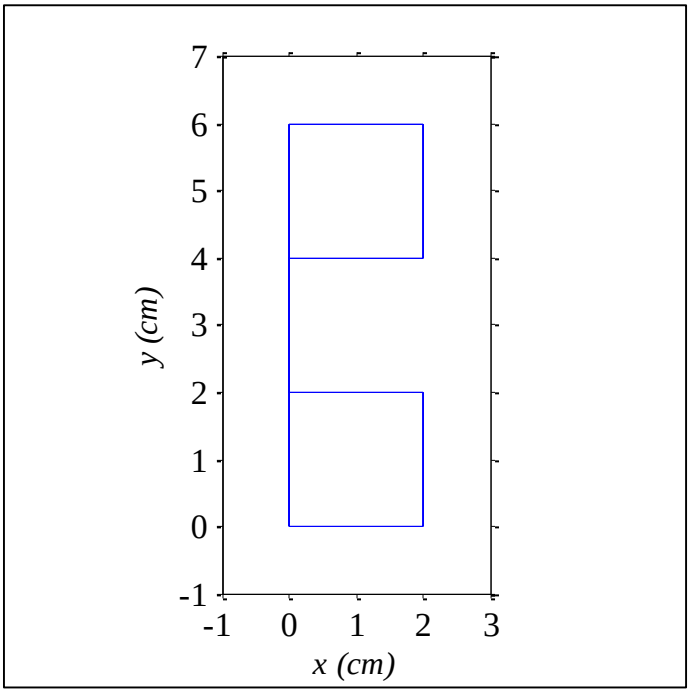

Figure 5.2: Ideal *x*-*y* Plane Scanning Pattern

It is important to note that there is no orientation change while the scanning is performed, i.e. the gyroscope readings will be close to zero. This, however does not mean that the initial rotational angles are also zeroes but depend on the orientation of the IMU sensor in space in reference to the gravity with the axes of the sensor. Table 5.2 summarizes the measurements taken.

Table 5.2: Experimental Program for Scanner

	Trials
Gravity in *x*-axis	10
Gravity in *y*-axis	10
Gravity in *z*-axis	10
Anonymous Orientation	10

The reason behind this setup is to test the accuracy of translation in all three axes. The scanner motors are maintained at 2000 rpm each and the initial position for all scans is identical to maintain consistency in the measurements. The overall error of the results is calculated based on the final destination that the sensor reaches in reference to the expected final destination of the scan.

5.1.2.1 Scanning with sensor mounted with gravity in *x*-axis

Position tracking is tested by orienting the IMU sensor such that gravity is solely present in the *x*-axis of the sensor. The sensor orientation can be seen in Figure 5.3.

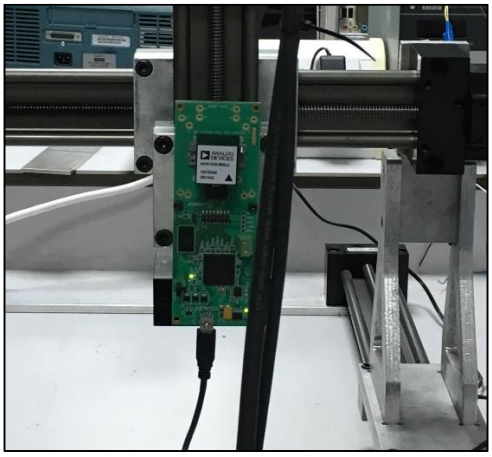

Figure 5.3: Initial Orientation of gravity in *x*-axis

In theory, gravity only exists in the *z*-axis of the world coordinate system, therefore, its existence in any other axis in regards to the sensor coordinate system entails the need for rotation. Despite the axes alignment in both coordinate systems, the axes direction is mismatched.

$$\begin{pmatrix} x_s \\ y_s \\ z_s \end{pmatrix} = \begin{pmatrix} z_{sc} \\ -x_{sc} \\ -y_{sc} \end{pmatrix} = \begin{pmatrix} -z_w \\ x_w \\ -y_w \end{pmatrix} \tag{5.2}$$

In turn, this induces a shift in the Euler angles of the system, which needs to be determined in order to achieve the rotation needed to match the axes. For the above setup, the Euler angles are calculated to be:

$$\begin{pmatrix} \theta_x \\ \theta_y \\ \theta_z \end{pmatrix} = \begin{pmatrix} 0 \\ -90 \\ -90 \end{pmatrix} \tag{5.3}$$

Upon commencing the scanning process, the IMU sensor captures the acceleration of the scanner motors in all three axes. In Figure 5.4, the captured acceleration data from the IMU sensor are presented. As expected, the sensor *x*-axis captured most of the gravity components with some existing in the other axes due to physical misalignment. This however is corrected for by the system using the acquired magnitudes of the acceleration using the equations governing the angle calculations.

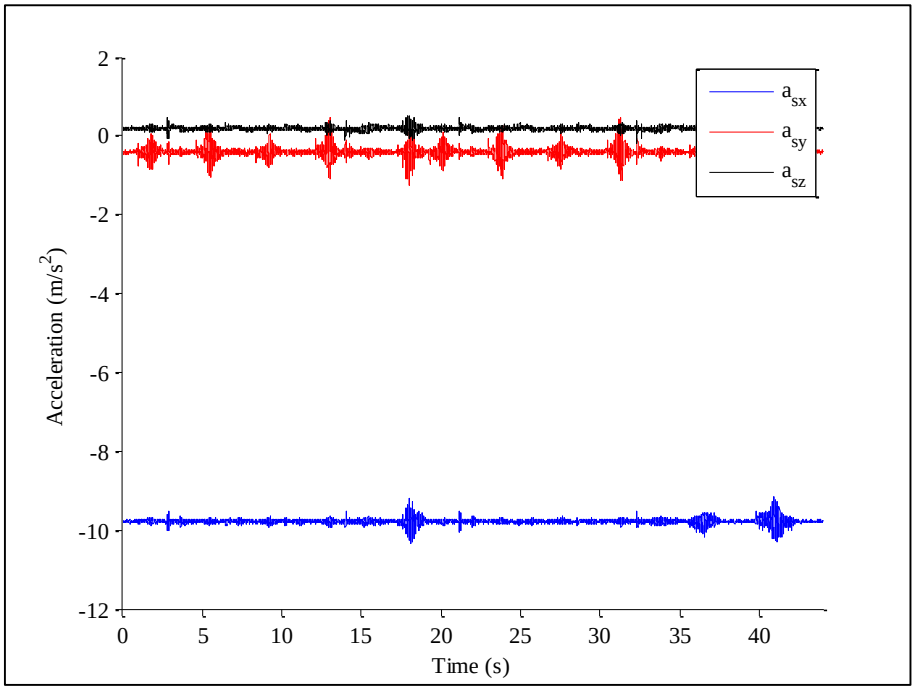

Figure 5.4: IMU raw data for gravity in *x*-axis scan

After correcting for the mismatch using rotation, the gravity components are cleaned and the acceleration is rotated to the world coordinate system shown in Figure 5.5. The acceleration magnitudes present in the *y*-axis, *x*-axis, and *z*-axis in Figure 5.4 are now residing in the *x*-axis, *z*-axis, and *x*-axis respectively in Figure 5.5. This is followed by removal of gravity components.

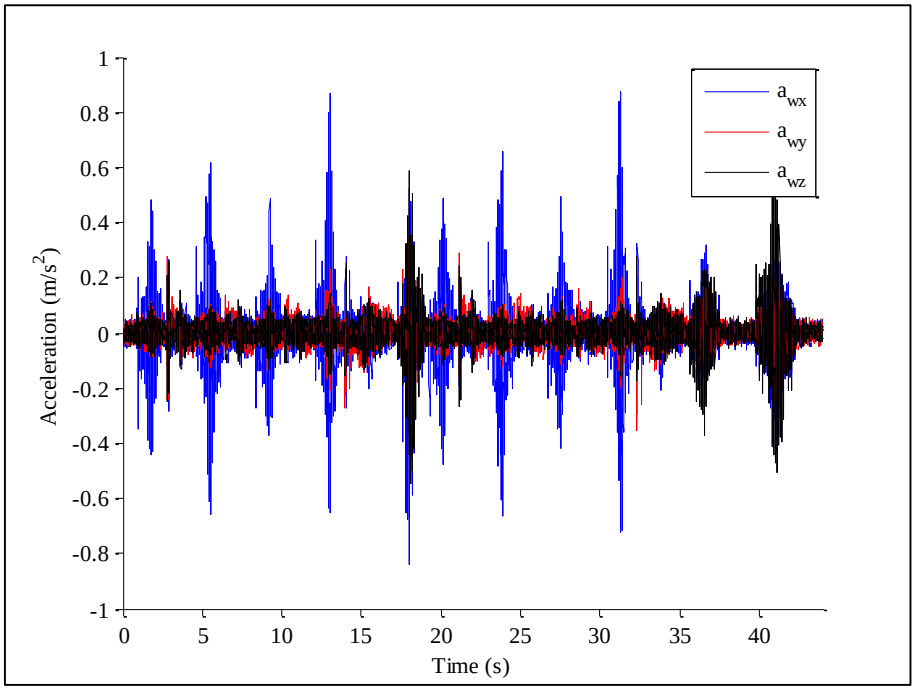

Figure 5.5: Rotated Accelerations for gravity *x*-axis scan

In an identical approach, all different trials are corrected and integrated to acquire position measurements. The average of all trials as a function of distance is shown in Figure 5.6.

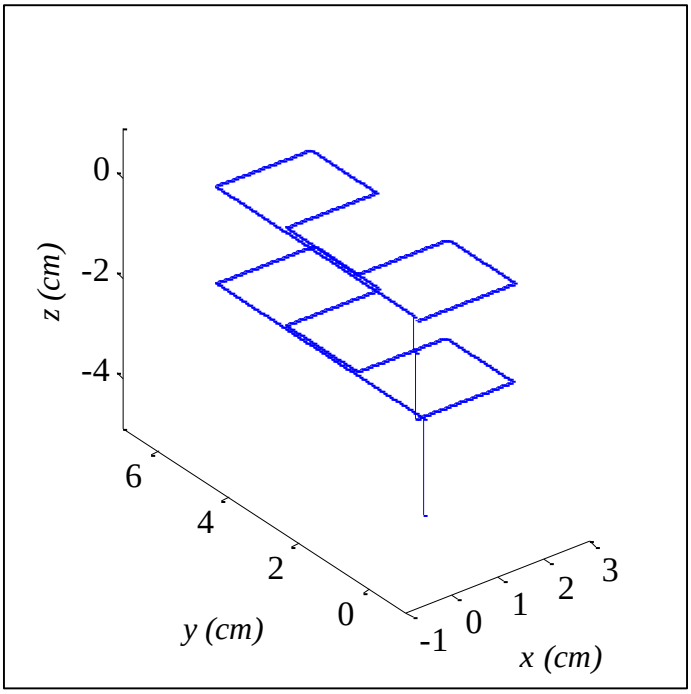

Figure 5.6: *x*-axis scans Position Output Average

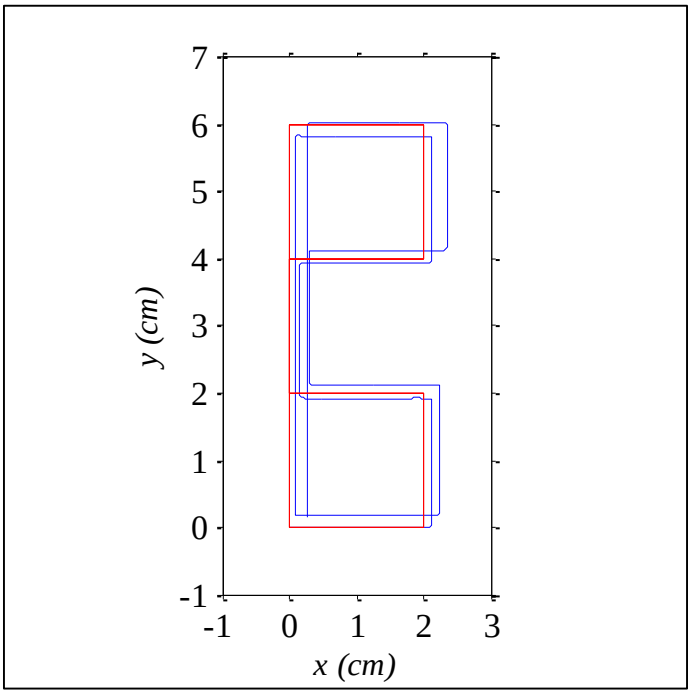

Figure 5.7: *x*-axis Position Average *x*-*y* Plane

The attained distance pattern in 3D in Figure 5.6 and the *x*-*y* plane in Figure 5.7 is similar to the expected pattern. Increments in all axes were fully captured by the system with uncertainty in the millimeter range. The overall displacement of the scanning pattern was recovered from the sensor data. The position measurements demonstrated precise locations of the sensor in the scanning process, i.e. not only at the starting and ending points of the scan. This methodology is capable of extracting position calculations with extremely low drifts providing an accurate representation of the displacement pattern of the sensor with overall errors calculated in the millimeter range as provided in Table 5.3.

Table 5.3: *x*-axis Error calculations for measurements

	x (mm)	***y (mm)***	***z (mm)***
Theoretical	0	0	-40
Measured Accuracy	2.56	1.50	-40.33
Precision	4.13	5.30	1.47
Overall Distance	160	240	40
Absolute Error	1.60 %	0.63 %	0.83 %

The accuracy of the position data is quantified in terms of the overall error average of all the runs along with the standard deviation present. It is noticeable that the error involved in the system is very small compared to the overall displacement. The absolute error is the difference between the measured and the accurate in ratio with the full displacement.

Table 5.4: *x*-axis Error calculations for each increment in every axis

	x (mm)		***y (mm)***		***z (mm)***
Direction	Positive	Negative	Positive	Negative	Negative
Theoretical	20	-20	20	-60	-20
Meas. Accuracy	20.07	-20.71	19.46	-57.62	-20.17
Precision	1.40	1.44	1.36	3.90	1.34

Table 5.4 summarizes the average measurements average accuracy and precision in all 10 runs for their increments in the positive and negative directions.

5.1.2.2 Scanning with sensor mounted with gravity in *y*-axis

The same type of measurement is also taken however with the IMU sensor's *y*-axis parallel to the gravitational force. The sensor orientation can be seen in Figure 5.8.

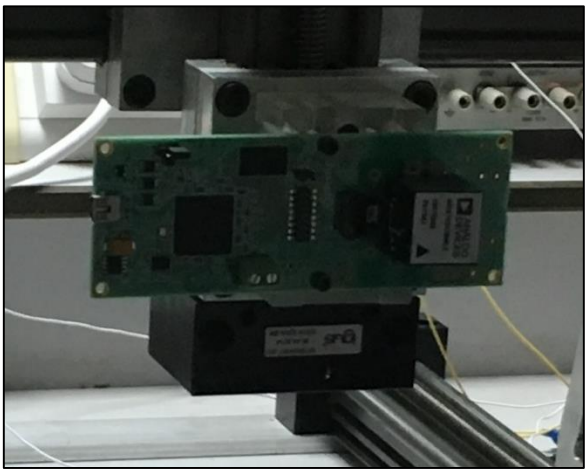

Figure 5.8: Initial Orientation of gravity in *y*-axis

Likewise, gravity can only exist in the *z*-axis and therefore rotation needs to take place in order for the position estimation to be accurate in reference to the user. Similar to the previous set of measurements, the axes of the sensor are aligned with the axes of the scanner and in turn aligned with the world coordinate system howver with a mismatach. The sensor coordinate system are thererfore:

$$\begin{pmatrix} x_s \\ y_s \\ z_s \end{pmatrix} = \begin{pmatrix} -x_{sc} \\ z_{sc} \\ -y_{sc} \end{pmatrix} = \begin{pmatrix} x_w \\ -z_w \\ y_w \end{pmatrix} \tag{5.4}$$

Likewise, this induces a a shift in the Euler angle system in reference to the world coordiante system. Though the angles do not change as a function fo time nor space, the initial angles are not equal to zero either due to the mismatch.

$$\begin{pmatrix} \theta_x \\ \theta_y \\ \theta_z \end{pmatrix} = \begin{pmatrix} -90 \\ 0 \\ 0 \end{pmatrix} \tag{5.5}$$

The acceleration data collected from the IMU sensor as predicted were mostly captured in the *y*-axis. Since the *y*-axis of the IMU sensor is directed in the same direction as gravity, the polarity of the gravity acceleration is positive as shown in Figure. 5.9.

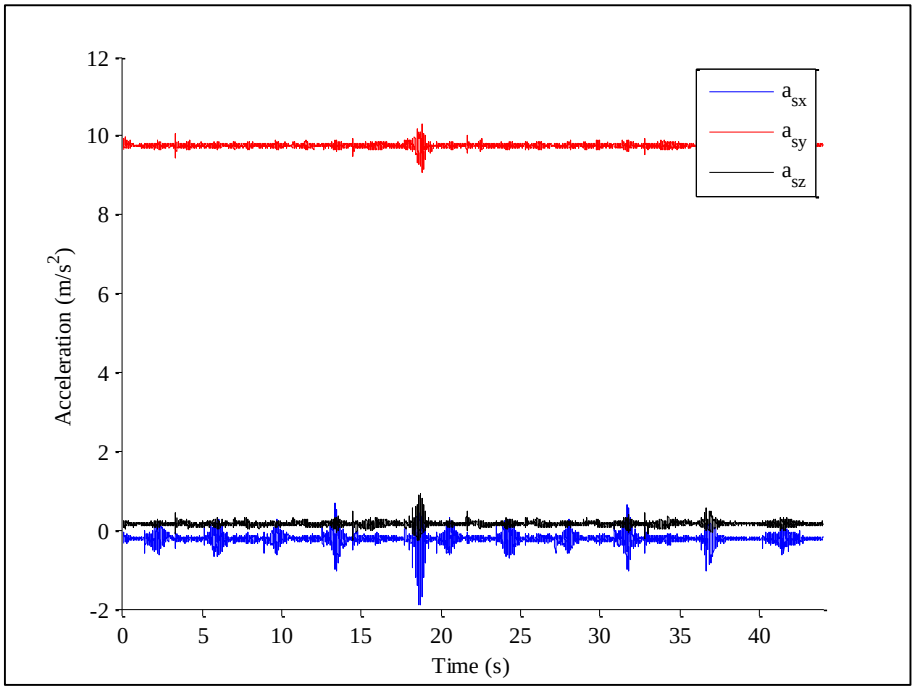

Figure 5.9: IMU Raw Data for gravity in the *y*-axis

After rotation, the acceleration magnitudes were converted to the world coordiante system with no mismatch between axes. In comparison to Figure 5.9, Figure 5.10 shows that the accelerations in the *x*-axis, *y*-axis, and *z*-axis in the sensor coordiante system are now residing in the *x*-axis, *z*-axis, and *y*-axis respectively in the world coordiante system. Also, gravity was removed from the *z*-axis.

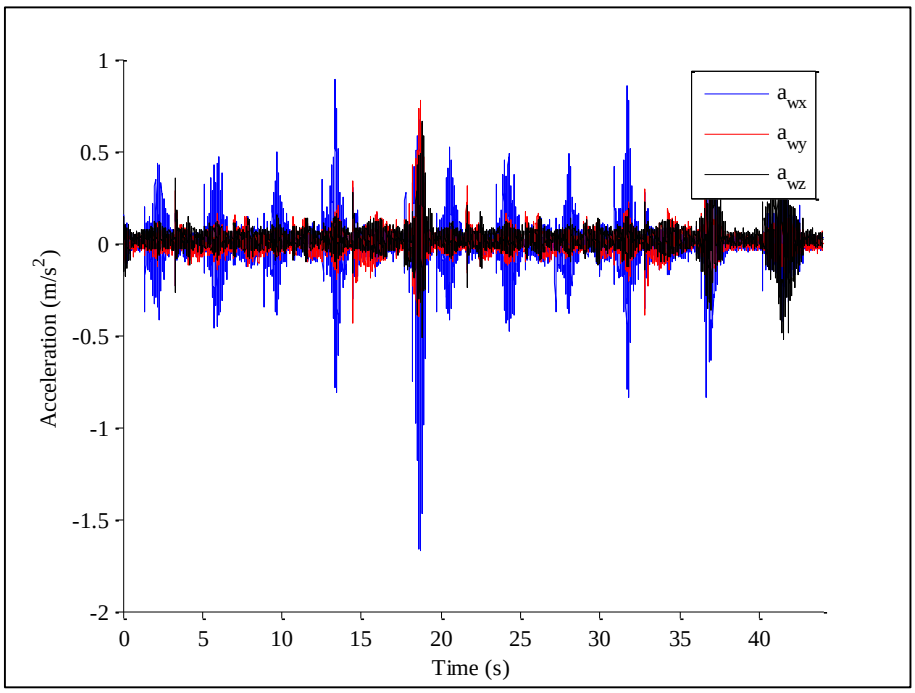

Figure 5.10: Rotated Accelerations for gravity in the *y*-axis scans

Similarly to the previous measurements, after the accelerations are rotated and cleaned from gravity, the data is integrated to calcualte position. More runs were taken for the same measurement system. The average of all runs as functions of position are shown in Figure 5.11 in all three axes.

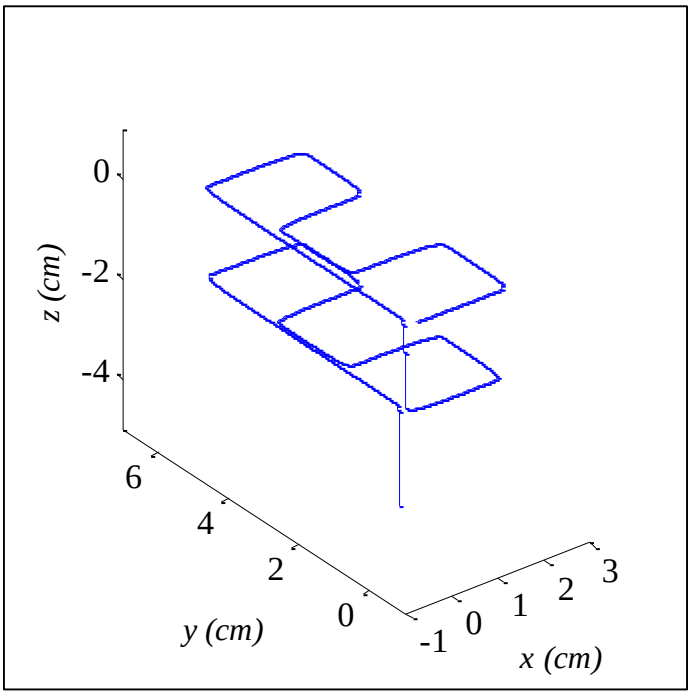

Figure 5.11: *y*-axis scans Position Output Average

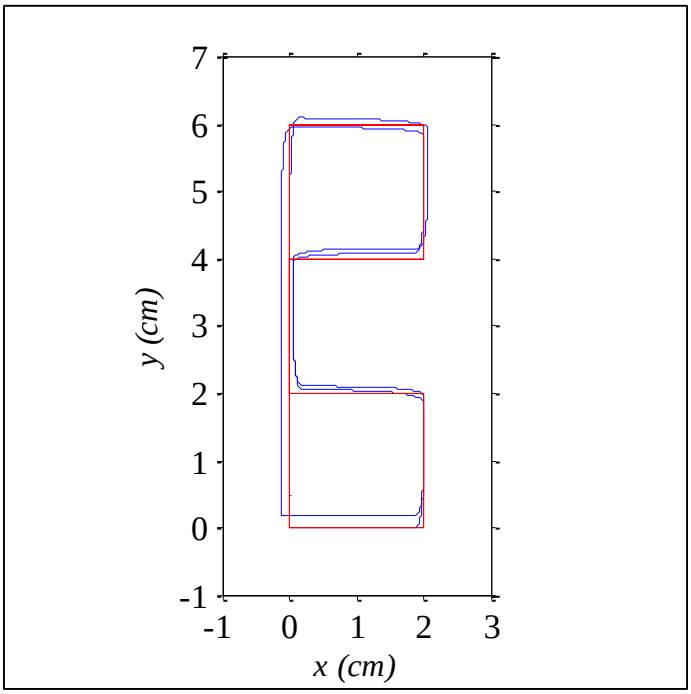

Figure 5.12: *y*-axis Position Average *x*-*y* Plane

The position pattern was fully captured as shown in Figure 5.11 for the 3D pattern and Figure 5.12 for the 2D *x*-*y* plane pattern. The overall displacement was also visible by the readings and the algorithm recovered the position precisely. All increments in the *x*, *y* and *z*-axis were all captured.

Table 5.5: *y*-axis Error calculations for measurements

	x (mm)	***y (mm)***	***z (mm)***
Theoretical	0	0	-40
Measured Accuracy	0.27	5.09	-40.81
Precision	3.97	5.64	1.40
Overall Distance	160	240	40
Absolute Error	0.17 %	2.01 %	2.03 %

The bias drift was extremely low in comparison to the overall displacement summarized in Table 5.5 in the absolute error calculations. Considering the overall pattern of the sensor, the overall errors are considerably small leading to inaccuracy in the range of a few millimeters in the *y*-axis and less than 1 millimeter in the *x* and *z* axes. These results show that the system is capable of recovering the location of the sensor all around the path and recover the pathway with minimal errors in reference to Table 5.5.

Table 5.6: *y*-axis Error calculations for each increment in every axis

	x (mm)		***y (mm)***		***z (mm)***
Direction	Positive	Negative	Positive	Negative	Negative
Theoretical	20	-20	20	-60	-20
Meas. Accuracy	20.04	-20.06	19.76	-56.89	-19.59
Precision	1.77	1.90	1.77	3.58	1.23

Table 5.6 summarizes the increment measured values for positive and negative increments in every axis. All increments in the 10 runs were averaged based on their axis and direction.

5.1.2.3 Scanning with sensor mounted with gravity in *z*-axis

The most orthodox methodology to the scan is to place the sensor not only in an alignment with the world coordinate system but also to match the axes as shown in Figure 5.13.

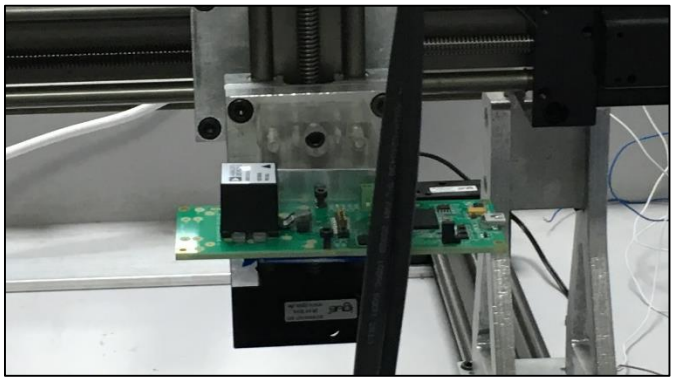

Figure 5.13: Initial Orientation of gravity in *z*-axis

In this setup, gravity will appear in the *z*-axis of the sensor which also matches the world coordinate system assumption. The sensor coordinate system in reference to the scanner coordinate system and world coordinate system is thus as follows:

$$\begin{pmatrix} x_s \\ y_s \\ z_s \end{pmatrix} = \begin{pmatrix} -x_{sc} \\ y_{sc} \\ -z_{sc} \end{pmatrix} = \begin{pmatrix} x_w \\ y_w \\ z_w \end{pmatrix} \tag{5.6}$$

The fact that all three axes are matched suggests in theory that no rotation is needed and all Euler angles are zeros. In this setup, though no change in orientation is occurring but also the initial angles of the system are also zero. This suggests that the data the sensor captures are in the matched axis.

$$\begin{pmatrix} \theta_x \\ \theta_y \\ \theta_z \end{pmatrix} = \begin{pmatrix} 0 \\ 0 \\ 0 \end{pmatrix} \tag{5.7}$$

All rotation matrices are identity matrices and no rotation is induced on the system. The data collected from the sensor in one run of measurements is shown in Figure 5.14.

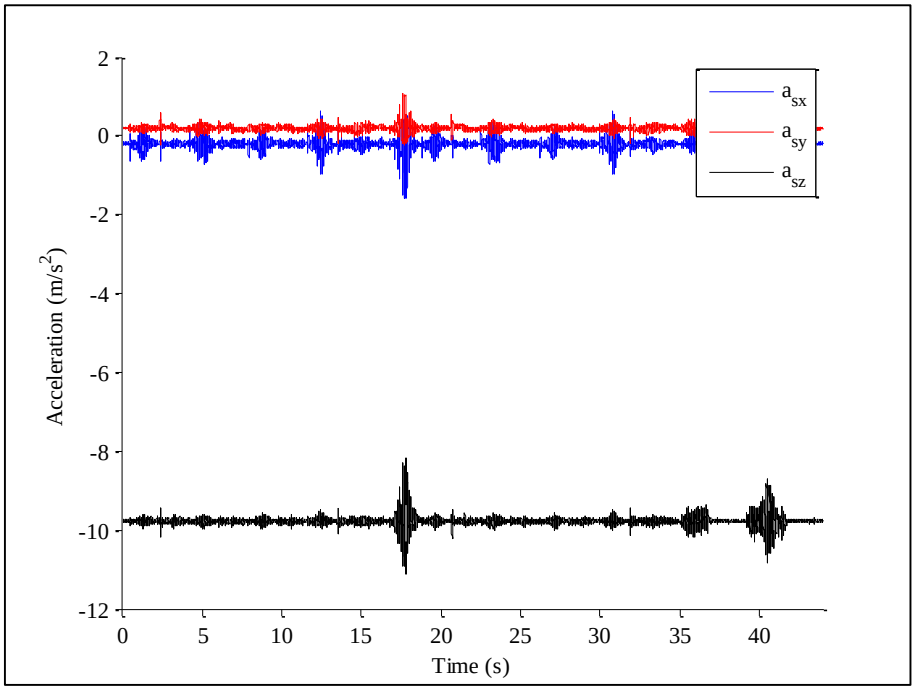

Figure 5.14: IMU Raw Data for gravity in the *z*-axis

Gravity is only residing in the *z*-axis of the sensor raw data in Figure 5.14, thus the world coordinate system accelerations are supposed to have an identical measurement. Gravity is then removed from the system's *z*-axis and the result is shown in Figure 5.15. All axes maintained their magnitudes and the pattern of the increments is identical in all axes in both Figures 5.14 and 5.15.

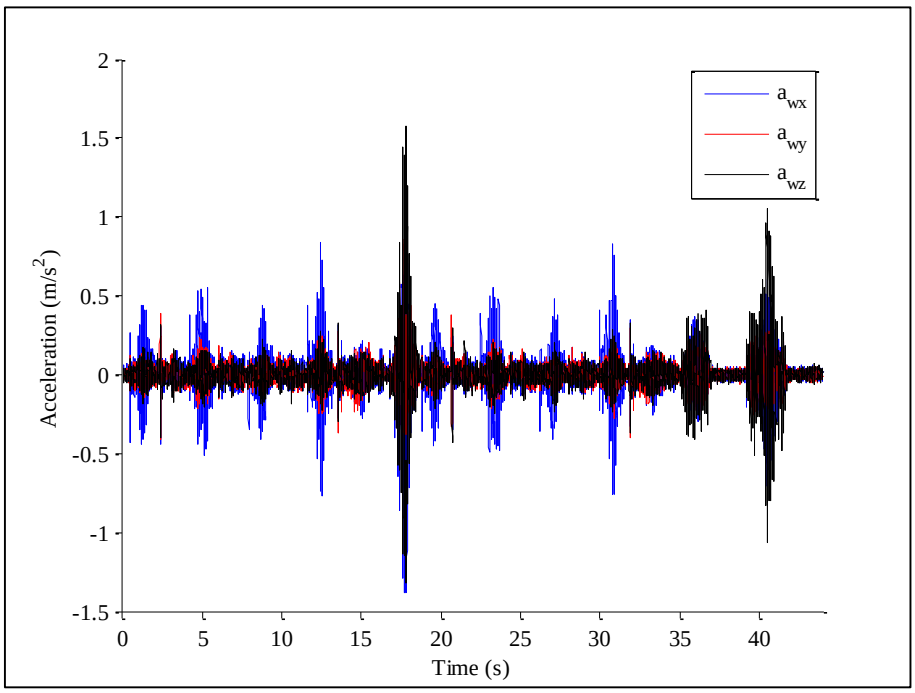

Figure 5.15: Rotated Accelerations for gravity in the *z*-axis scans

Integrations is imposed, and position radings are outputted. Figure 5.16 shows the position pattern of the sensor over the average of all 10 runs.

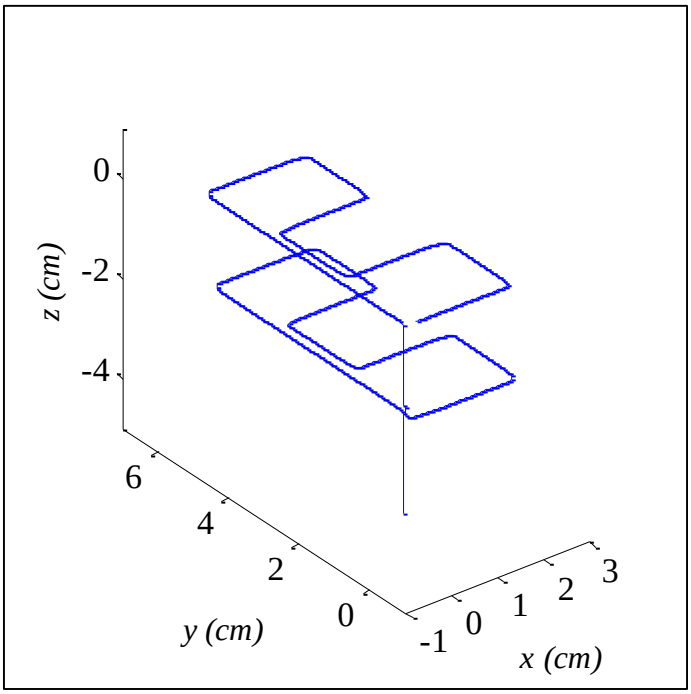

Figure 5.16: *z*-axis scans Position Output Average

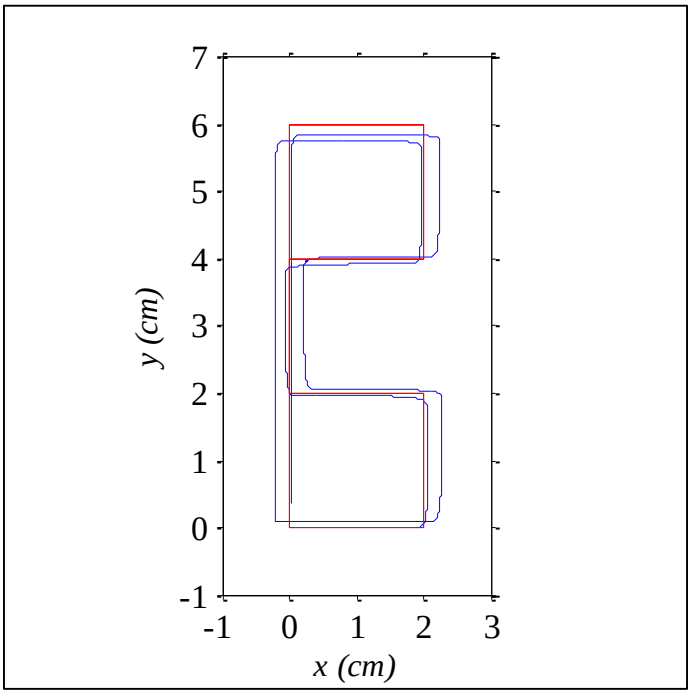

Figure 5.17: *z*-axis Position Average *x*-*y* Plane

Figure 5.16, showing the position pathway in 3D and Figure 5.17, showing the position pathway in the *x*-*y* plane demonstrate the pattern of the scan coming from the

psotion calcualtions. As shown, the pathway of the sensor in space was recovered completely. The increments in all axes were captured and outputted. The final location of the sensor was comapred to the expected final location to calcualte the uncertainity in all axes as shown in Table 5.7.

Table 5.7: *z*-axis Error calculations for measurements

	x (mm)	***y (mm)***	***z (mm)***
Theoretical	0	0	-40
Measured Accuracy	0.17	3.61	-39.91
Precision	6.20	5.96	1.93
Overall Distance	160	240	40
Absolute Error	0.11 %	1.50 %	0.18 %

The absolute error for all runs for this type of measurements are considerably lower than the errors present in the previous measurements, this is partially due to the initial angle calculations not altering any rotation on the system. The measured error present in the system is also in the millimeter range. This proves the strength of this algorithm in the Translation movement of the system along all three axes. Similar to the previous measurements, the algorithm recovered the pathway of the sensor in the scanning process with marginally low uncertainties.

Table 5.8: *z*-axis Error calculations for each increment in every axis

	x (mm)		***y (mm)***		***z (mm)***
Direction	Positive	Negative	Positive	Negative	Negative
Theoretical	20	-20	20	-60	-20
Meas. Accuracy	21.30	-21.35	19.25	-55.94	-19.97
Precision	1.49	3.38	1.42	2.88	1.41

Similarly, all increments positive and negative in every axis were analyzed. The analysis present in Table 5.8 summarizes the average measurements and standard deviation.

5.1.2.4 Scanning with sensor mounted with gravity in a random orientation

To prove the compatibility of this algorithm to translation even further and deepen its strengths in translation, the sensor is mounted on the scanner in a random

initial orientation as opposed to the known orientations in the previous measurements. The axes of the sensor are neither aligned nor matched with the axes of the scanner coordiante system which in turn leading to a misalignment and mismatch with the world coordiante system. This in turn does mean that the euler angles are also random. In these measurements, the algorithm capabilities are tested in predicting the euler angles and correcting the mismatch introduced to the system. The overall goal is to achieve the same pattern regardless of the orientation of the sensor. Figure 5.18 shows the acceleration raw data captured by the sensor. Though the orientation was random, the acceleration in the *z*-axis in the sensor coordiante system was close to zero meaning that no gravity components were present in the *z*-axis.

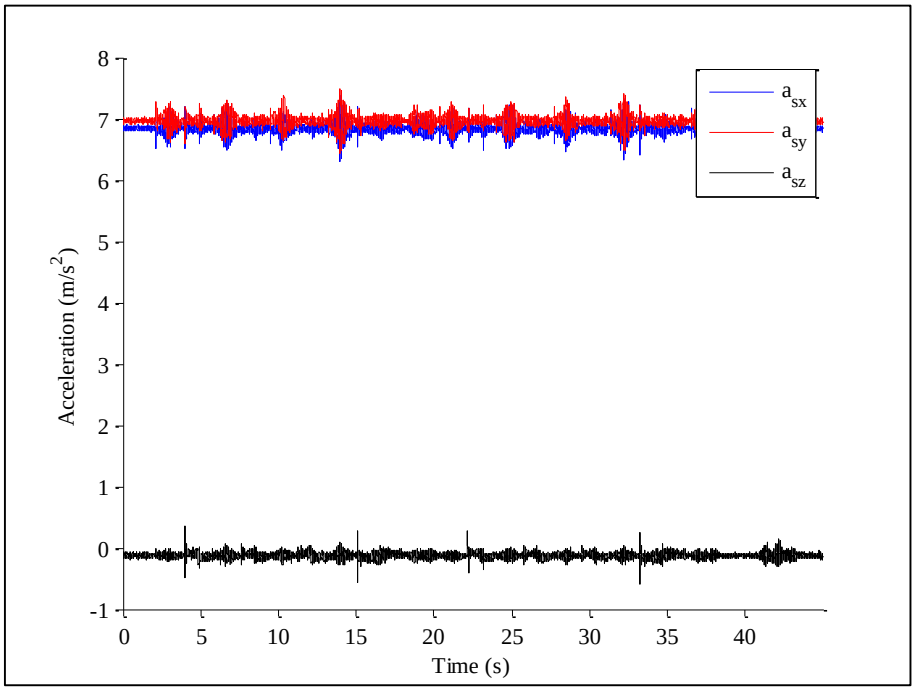

Figure 5.18: IMU Raw Data for random initial orientation

Figure 5.19 demonstrates the accelerations after rotation and cleaning of the gravity components. It is noticeable that the pattern present in the world coordiante system accelerations is similar to all the previous runs on the scanner. This shows clear potential in the rotation mechanism that the algorithm is providing to the data.

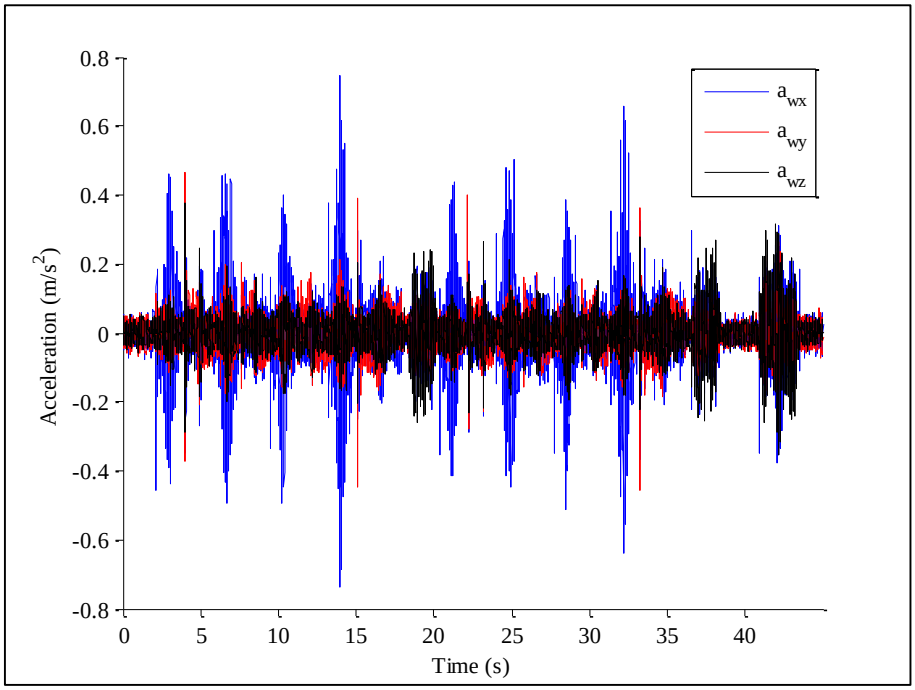

Figure 5.19: Rotated Accelerations for random initial orientation scans

The data is integrated twice to calcualte for the position. The overall position pattern for all 10 runs in 3D is shwon in Figure 5.20.

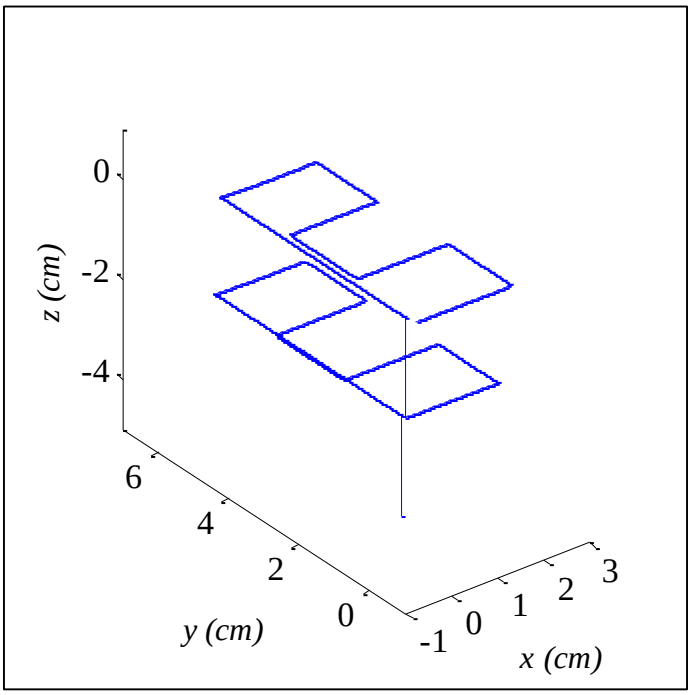

Figure 5.20: Random Initial Orientation Position Output Average

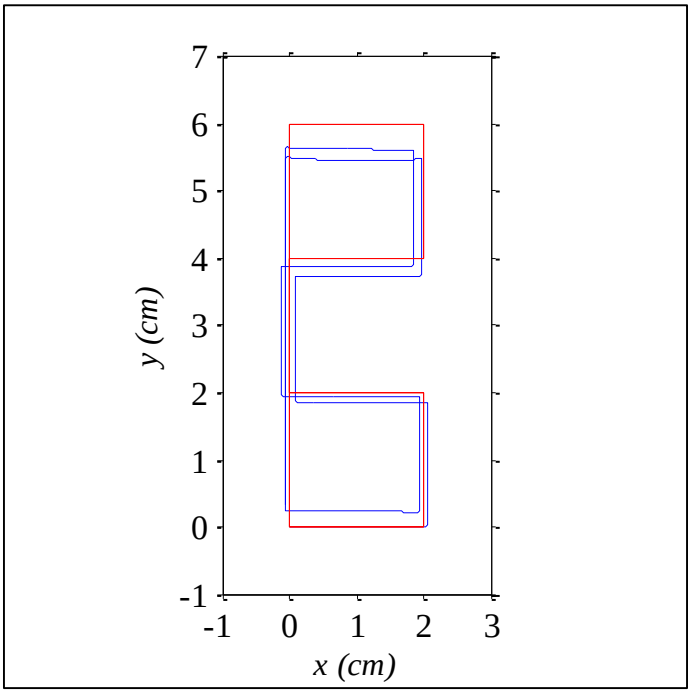

Figure 5.21: Random Initial Orientation Position Average *x*-*y* Plane

The position pathway was recovered as shown in both Figure 5.20 in 3D and Figure 5.21 in the *x*-*y* plane by the algorithm. The increments in all axes were also captured by the algorithm as well. The overall displacement and the errors involved are shown in Table 5.9.

Table 5.9: Random Orientation Error calculations for measurements

	***x* (mm)**	***y* (mm)**	***z* (mm)**
Theoretical	0	0	-40
Measured Accuracy	-0.54	3.32	-40.12
Precision	4.11	8.90	3.27
Overall Distance	160	240	40
Absolute Error	0.34 %	1.36 %	0.29 %

Although the orientation was completely random, the algorithm captured position with very accuracy as well. The acceleration magnitudes were rotated and restored to the world coordinate system regardless of the orientation of the sensor. The algorithm demonstrated strengths in a considerably low drift bias error, i.e. a few millimeters in the *x*-axis along with smaller than 0.5 millimeters in the *y* and *z* axes.

Table 5.10: Random Orientation Error calculations for each increment

	x (mm)		***y (mm)***		***z (mm)***
Direction	Positive	Negative	Positive	Negative	Negative
Theoretical	20	-20	20	-60	-20
Meas. Accuracy	19.92	-19.78	18.11	-52.67	-20.06
Precision	2.05	1.77	2.55	7.23	1.82

Table 5.10 summarizes the data analysis for every type of increment. The increments were clustered based on their axis and direction. Averages and standard deviations were calculated based on the measurements.

5.1.2.5 Discussion and analysis for scanner measurements

All measurements were compared in terms of drift bias error due to its huge contribution in reducing the accuracy of the signal. If drift bias error is not treated, the position pattern is lost and so is the displacement of the sensor leading to corrupted estimation. This however was treated using the proposed algorithm and the final displacement values were precise and accurate with errors less than 5% not exceeding half a centimeter overall.

Whether the measurement is taken using known gravity components or being random in space, the proposed algorithm recovered the movement pattern with all increments in the three axes. This proves the translation transformation appearing in the scans. This however would not have been possible if the algorithm was not capable of estimating the initial orientation of the sensor in space and therefore proving its capabilities in rotation of the axes along a fixed orientation for the scan pattern overall.

In the transformation theory, translation does not cover the complete phenomena lacking a varying orientation throughout the scan. The next setup presented in Section 5.2 demonstrates the capabilities of the algorithm to adjust to a varying orientation.

5.2 Angular

In order to test for the rotational strengths of the system, the sensor along with the algorithm are tested versus a servo motor setup. However, due to physical limitations, the motor is removed and hand movement is introduced. In order to

maintain accuracy, an angular encoder is used to measure the rotational position of the sensor.

5.2.1 Equipment and program

The setup is composed of a circular metal piece that rotates freely around its axis which is connected to a Honeywell 600-128-CBL angular encoder. The encoder is a 128 pulse per revolution and is connected to a DAQ which in turn is operated using LabView as well to measure and store the data. The sensor is attached on the metal piece and rotated using hand movement. The setup is shown in Figure 5.22.

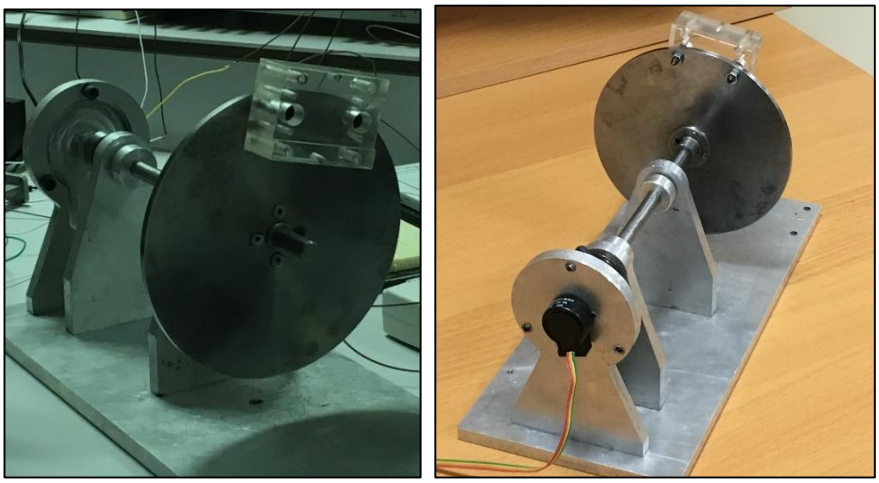

Figure 5.22: Angular Tests Setup: Circular Metal Piece and Encoder

5.2.2 Motion pattern

The tests will take place in two different setups summarized in Table 5.11. The two setups differ in the orientation of the sensor. Unlike the scanner methodology, the orientation of the sensor changes along the path, therefore, identifying the angle varying with motion is crucial to prove that the algorithm can provide the most accurate estimate regardless of which angle varying. This is due to the fact that the sensor orientation dictates completely different angles in the rotation.

Also, since gimbal lock is of an issue, the rotation is limited to an arc around the circular path. Therefore, limitations in the full pathway are imposed specifically in the pitch measurements. Gimbal lock will destroy the angle calculations done on the gyroscope data and impact the results of the rotation matrices leading to a miscalculation in motion and position along the measurements.

Thus, any pathway leading to pitch closing up to 90 degrees will be avoided in the following measurement sets.

Table 5.11: Experimental Program for Angular Position Tests

IMU sensor orientation	Trials
Rotation Methodology 1 (Known Orientation)	10
Rotation Methodology 1 (Random Orientation)	10
Rotation Methodology 2: Short Path	10
Rotation Methodology 2: Long Path	10

5.2.2.1 Rotation methodology 1: known initial orientation

The first measurement has the sensor attached to the circular metal piece as shown in Figure 5.23. The overall movement of the system is covering a third of the circumference only to ensure no gravity is occurring in the *x*-axis. This is done to maintain the pitch values between -45 and 45 degrees to ensure that the gyroscope data process does not fail due to the Gimbal lock effect.

Figure 5.23: Rotation Methodology 1: Known Orientation

The rotation of the metal will inflict a rotation around the *y*-axis, i.e. pitch will be varying. The encoder stores the values of the rotation which are considered as pitch values in this setup as well. After taking the measurements coming from the sensor and calculating pitch using the Kalman Filter, the values were compared versus the encoder

pitch angle measurements. Figure 5.25 shows a comparison between both the measurements and the calculations.

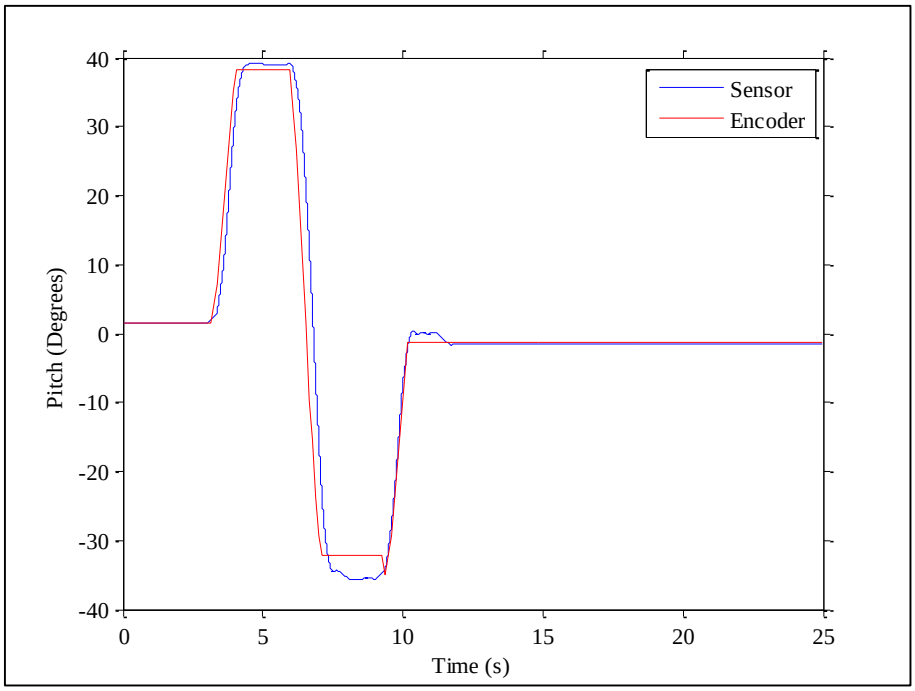

Figure 5.24: Pitch Angle Comparison between Kalman Filter and Encoder

At the end of the measurement, both values coming from Kalman Filter calculations and the Encoder are compared in Table 5.12 to show the error over the whole run. The error is extremely small being less than 2 degrees of error.

Table 5.12: Angular Position Comparison for Rotation Methodology 1

	Pitch (Degrees)
Sensor	-1.55
Encoder	-1.24
Total Angular Position	139.38
Absolute Error	0.22%

Based on the algorithm, once the Euler angles are estimated by the system, the acceleration data is then rotated to the world coordinate system, cleaned from any gravity components, then double integrated to calculate position.

Figure 5.25 demonstrates the average position path that the sensor undergoes in all trials.

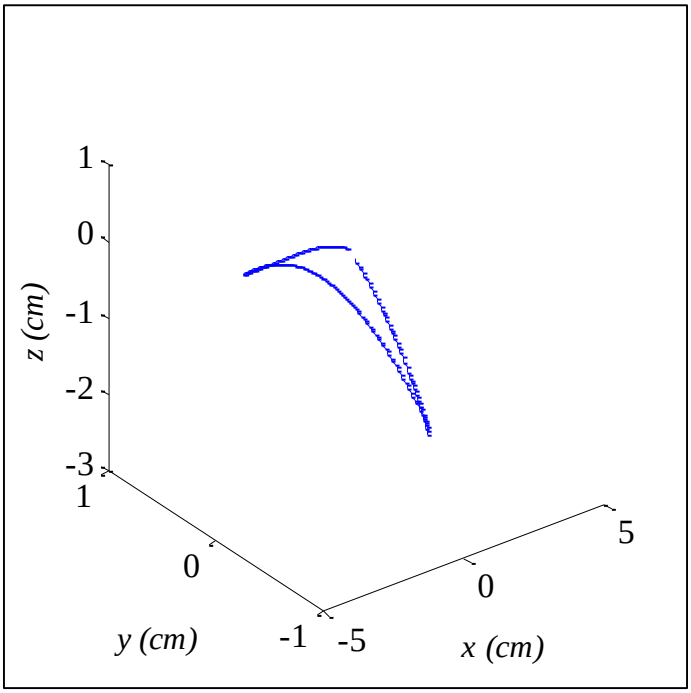

Figure 5.25: IMU sensor Position Output Average
for 10 runs for circular pathway (Methodology 1: Known Initial Orientation)

A better representation of the pathway is residing in the *x*-*z* plane since no motion was along the *y*-axis shown in Figure 5.26. As seen the estimated position calculations maintained the circular path anticipated from the rotation.

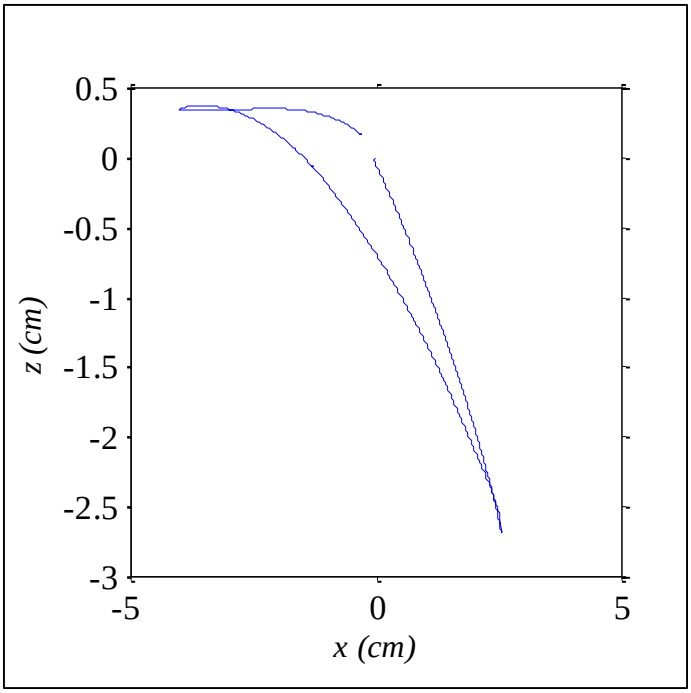

Figure 5.26: *x*-*z* plane of the position pathway of the sensor
(Methodology 1: Known Initial Orientation)

Moreover, the bias error did not drift but was kept at minimal as the sensor travelled back to a relatively close point to the initial point. The error in terms of translation was also calculated using the final destination of the sensor in reference to the initial point that the sensor started from. The overall uncertainty is less than 1 millimeter in all axes which shows extremely strong potential. The overall displacement, however was short mainly due to the physical limitation of the radius of the circular metal. The circular path was recovered with very low absolute errors in all axes. Table 5.13 summarizes the error calculations in all three axes.

Table 5.13: Error calculations for measurements using rotation methodology 1

	x (mm)	***y (mm)***	***z (mm)***
Theoretical	0	0	0
Measured Accuracy	-3.62	0	-0.29
Precision	5.53	0	3.57

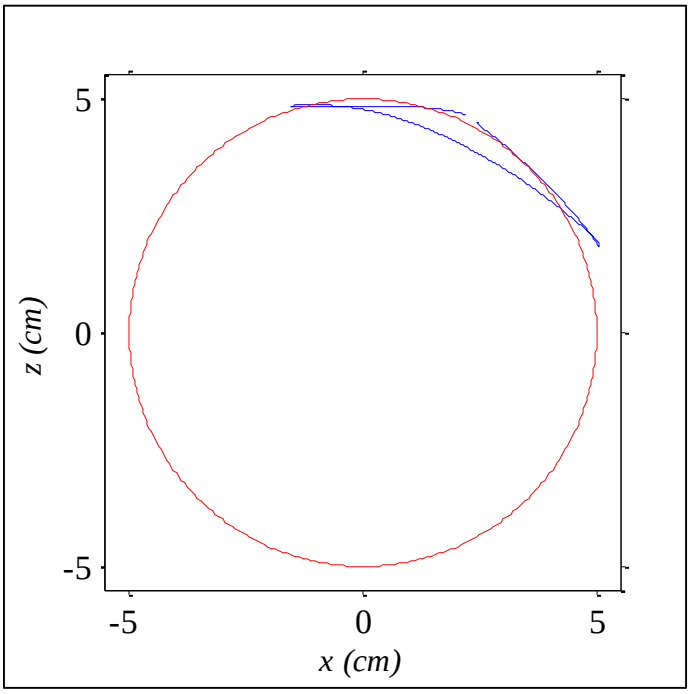

Figure 5.27: Measured Vs. theoretical Methodology 1 Known Orientation

Since the angular position calculations were close to the measured data coming from the encoder, the algorithm is to high certainties estimating the position, whether angular or translational, in a relatively accurate manner with errors not exceeding the 1

millimeter in all axes and 0.3 degrees in the angular position. Figure 5.27 shows the theoretical versus the measured values for position.

5.2.2.2 Rotation methodology 1: random initial orientation

In this set of measurements, the sensor is placed at a random orientation which is not matched with any of the three axes. The sensor however is placed at an opposite orientation in the *x*-axis to compare with the previous set of measurements as the position pathway is supposed to be equivalent in both sets. Figure 5.28 shows the sensor mounted on the circular metal.

Figure 5.28: Random Orientation Methodology 1

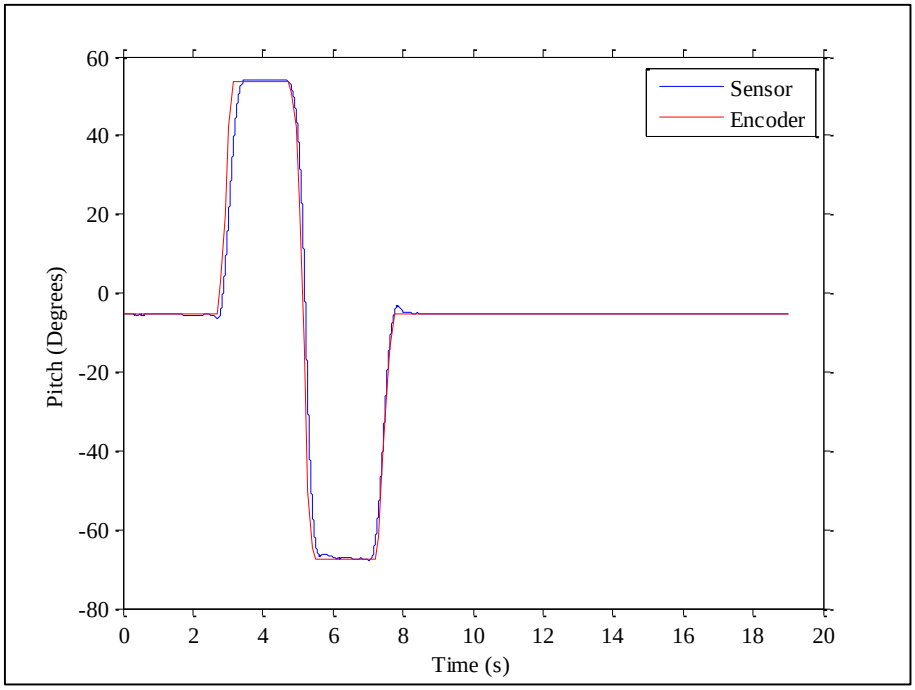

Figure 5.29: Pitch Angle Comparison between Kalman Filter and Encoder Methodology 1 Random

Similarly, pitch is the angle subject to variation in this setup. However, the axes of the gyroscope will all capture variation in the sensor coordinate system. The idea behind this set is to measure the accuracy of the rotation inflicted on the gyroscope data into the world coordinate system and compare it with the encoder values. Figure 5.29 shows the difference between them. Similar to the previous analysis, the angles are measured at the end of the scan to analyze the bias error available in the angles. Table 5.14 summarizes the errors and their average in all runs.

Table 5.14: Angular Position Comparison for Rotation Methodology 1 Random

	Pitch (Degrees)
Sensor	-5.14
Encoder	-5.49
Total Angular Position	241.86
Absolute Error	0.14%

Once the acceleration data is rotated to the world coordinate system, the data is double integrated to calculate for the position of the sensor in the world coordinate system in reference to the user.

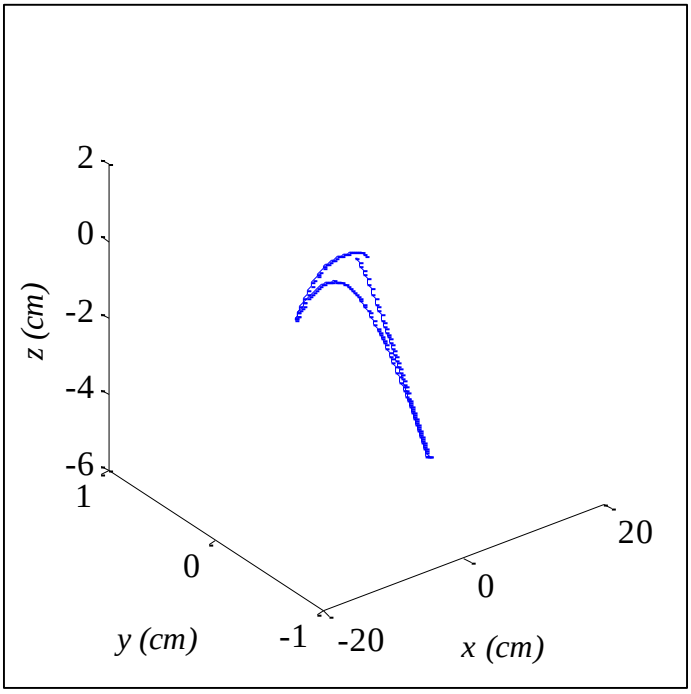

Figure 5.30: IMU sensor Position Output Average
for 10 runs for circular pathway (Methodology 1: Random Initial Orientation)

As Figure 5.30 shows, the position pathway is relatively close to that of the previous set, however the pattern does not look identical because there are some errors in the *y*-axis. The *x*-*z* plane shown in Figure 5.31 shows the pathway around the circumference of the metal circle.

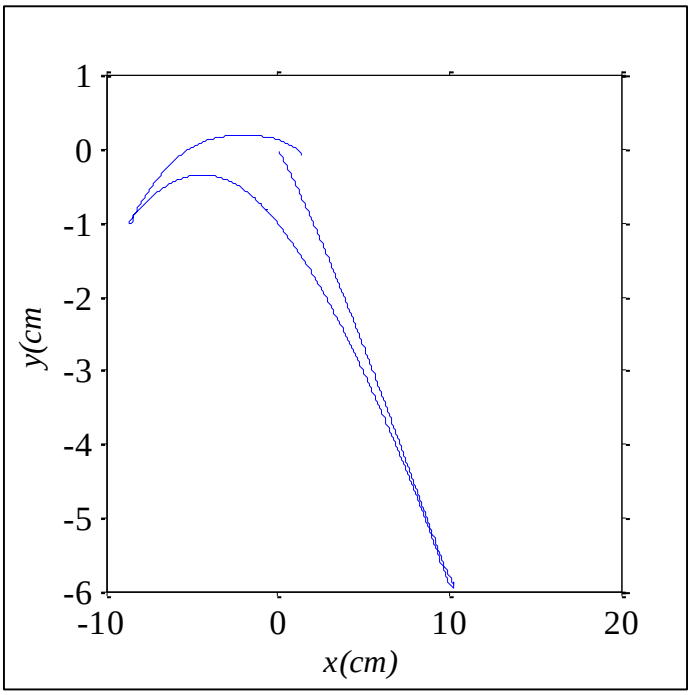

Figure 5.31: *x*-*z* plane of the position pathway of the sensor
(Methodology 1: Random Initial Orientation)

The circular path was captured by the sensor in the *x*-*z* plane. As expected the pathway took the opposite side of the circle as the sensor was in the opposite direction to the previous set. Unlike the previous set, there were some errors in the *y*-axis position calculations. Table 5.15 summarizes the errors involved for these sets.

Table 5.15: Error calculations for measurements using rotation methodology 1

	***x* (mm)**	***y* (mm)**	***z* (mm)**
Theoretical	0	0	0
Measured Accuracy	14.59	0	-2.18
Precision	11.82	0	5.17

The *x*-axis was the most inaccurate in the readings with close to 2 cm error which is considerably high. However, the pathway was close to the theoretical pathway showing a huge potential in capturing the position pathway for such methodologies.

Figure 5.32 shows the measured *x*-*z* plane versus the theoretical values based on the encoder angles and the radius of the circular metal piece.

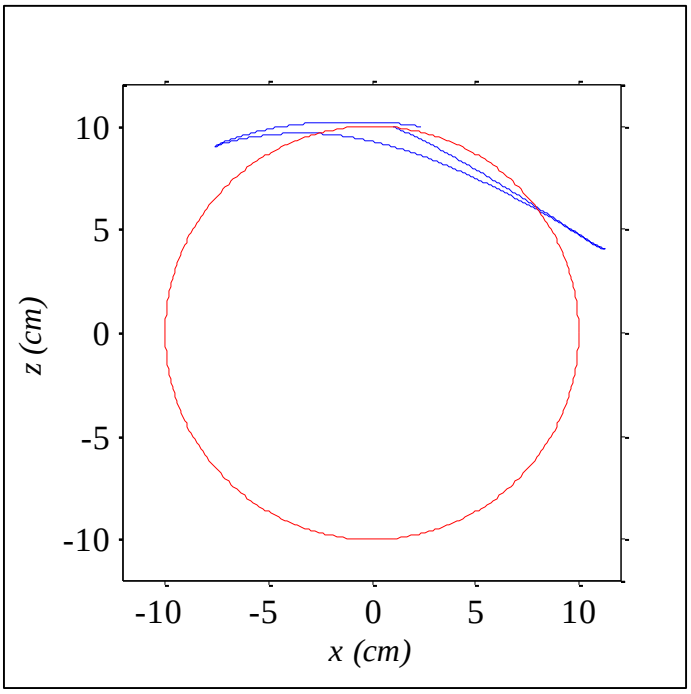

Figure 5.32: Theoretical Vs. Measured Methodology 1 Random

5.2.2.3 Rotation methodology 2: short path

This third set of measurements are based on the IMU sensor being oriented with its *x*-axis as normal and *y*-axis tangential to the center of metal circle, i.e. origin of rotational motion as shown in Figure 5.33. In this set however, the motion profile itself is changed to moving the sensor in a certain path and coming back only.

Figure 5.33: Rotation Methodology 2

The overall displacement of the test was a rotation of the metal piece to around one third of its circumference and a return to the initial point. Similar to the previous measurement set, the encoder stores the pitch values. Figure 5.34 shows a comparison between the pitch angle calculation from the algorithm versus the measurement of the encoder.

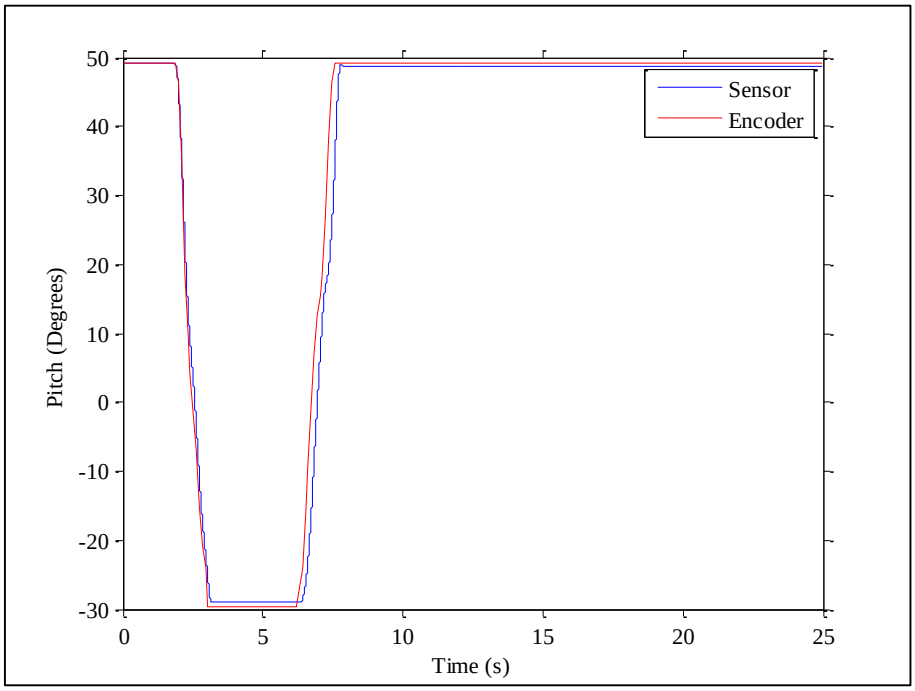

Figure 5.34: Pitch Angle Comparison between Kalman Filter and Encoder

At the end of the scan, the difference between the calculated angle coming from the Kalman Filter and the encoder measurement is close to 3 degrees. Tanle 5.16 demonstrates both angles and the difference between them for 10 runs. The overall bias drift error due to integration of the gyroscope readings along with the Kalman Filter successfully recovered the angular position pathway in regards to the encoder measurements for the trials.

Table 5.16: Angular Position Comparison for Rotation Methodology 2

	Pitch (Degrees)
Sensor	48.81
Encoder	49.21
Total Angular Position	157.50
Absolute Error	0.25%

Upon recovering the angular position of the measurements, the sensor coordinate system accelerations are rotated into the world coordinate system. Hence, the world coordinate system accelerations are double integrated to calculate position. The 3D position pattern shown in Figure 5.35.

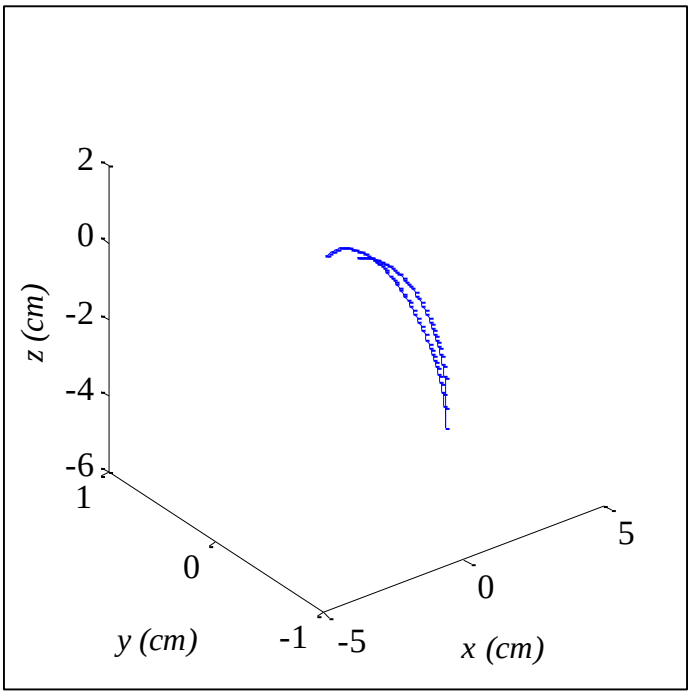

Figure 5.35: IMU sensor Position Output Average for 10 runs for circular pathway (Methodology 2)

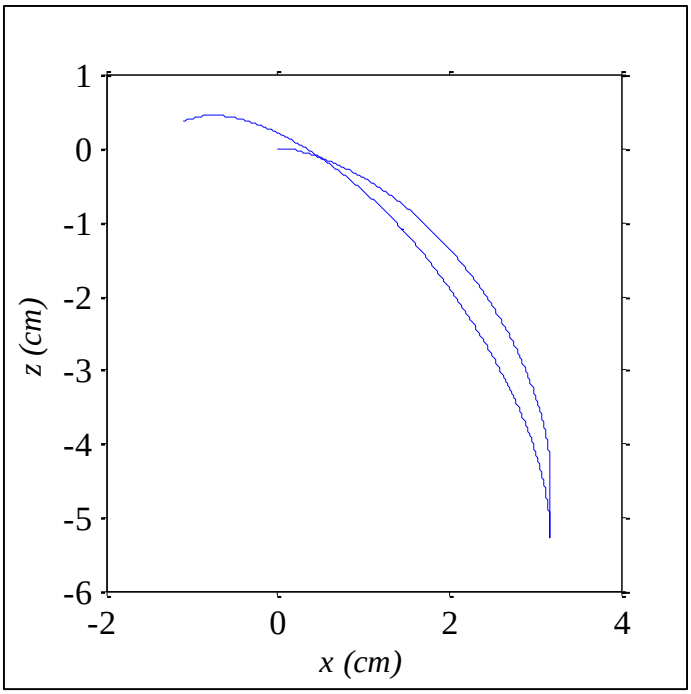

Figure 5.36: *x-z* plane of the position pathway of the sensor (Methodology 2)

Also, since the displacement is occurring in the *x* and *z* axes, Figure 5.35 shows the position profile in the *x*-*z* plane. The scan was rotated around the *y*-axis and returned to its initial position directly unlike methodology 1 which involved an extra distance travelled. As shown in Figure 5.36, the rotation movement was fully captured by the algorithm results and the final displacement is extremely close to the initial position. Since the rotation was returned to the initial position, the uncertainty similarly to the previous uncertainty calculations is the final point position in reference to the initial point. Table 5.17 summarizes the absolute error calculations. The uncertainty was in the millimeter range in all axes.

Table 5.17: Error calculations for measurements using rotation methodology 2

	x (mm)	***y (mm)***	***z (mm)***
Theoretical	0	0	0
Measured Accuracy	-11.02	0	9.59
Precision	3.31	0	5.53

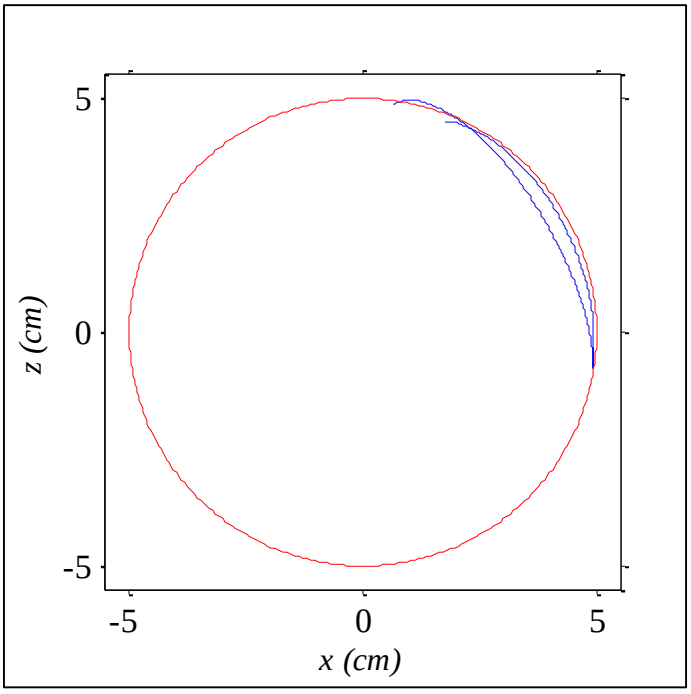

Figure 5.37: Theoretical Vs. Measured Methodology 2

The algorithm, yet again, recovered both rotation and translation from the data inputted to the sensor from the movement. The absolute error is less than 5% in all axes proving a strong potential in estimating transformation in space and capturing it in a

both effective and accurate pattern. The theoretical pathway versus the measured one is plotted in Figure 5.37.

5.2.2.4 Rotation methodology 2: long path

To understand the behavior of the algorithm without gravity present, the whole setup was placed vertically upwards, shown in Figure 5.38.

Figure 5.38: Sensor Orientation for Rotation Methodology 2: Long Path

Under this condition, regardless of the location of the sensor, gravity will only be present in the *z*-axis and the rotation will occur in yaw rather than pitch. The overall pathway taken by the sensor is a rotation along three quarters of the circle. Since the rotation is along yaw, the gimbal lock does not appear.

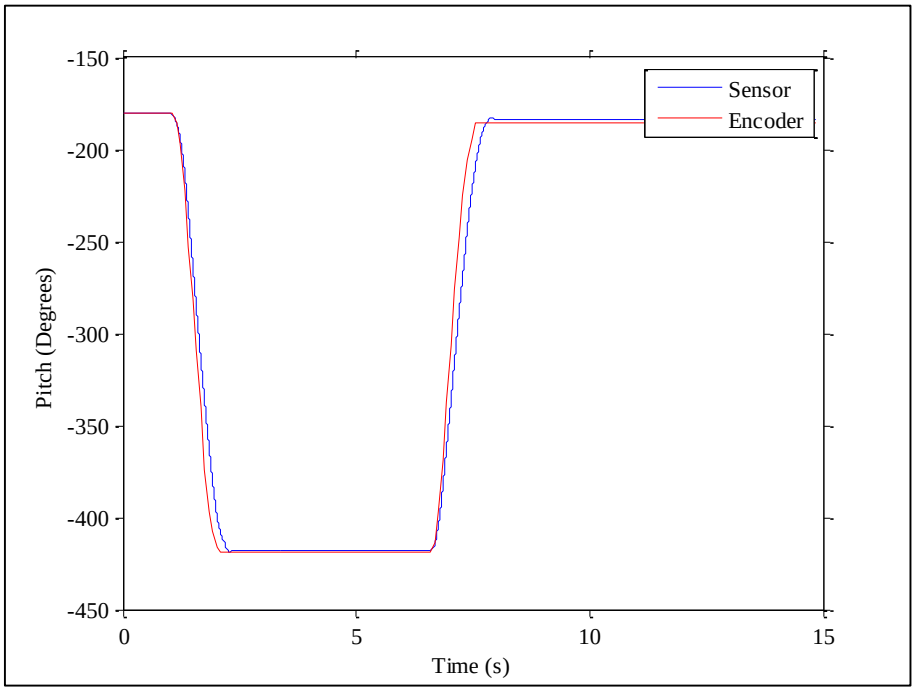

Figure 5.39: Yaw Angle Comparison between Kalman Filter and Encoder

Table 5.18: Angular Position Comparison for Rotation Methodology 2

	Pitch (Degrees)
Sensor	-183.70
Encoder	-185.60
Total Angular Position	472.60
Absolute Error	0.40%

A rotation of around 240 degrees was achieved, simulating close to two third a circle pathway. Figure 5.39 compares the yaw measurements between the IMU sensor Kalman filter and the encoder. Considering the unavailability of another method to calculate for yaw except from the gyroscope, the proposed algorithm was consistent in its measurements of yaw in comparison to the encoder. Table 5.18 summarizes the absolute error and the overall drift bias over the course of measurement.

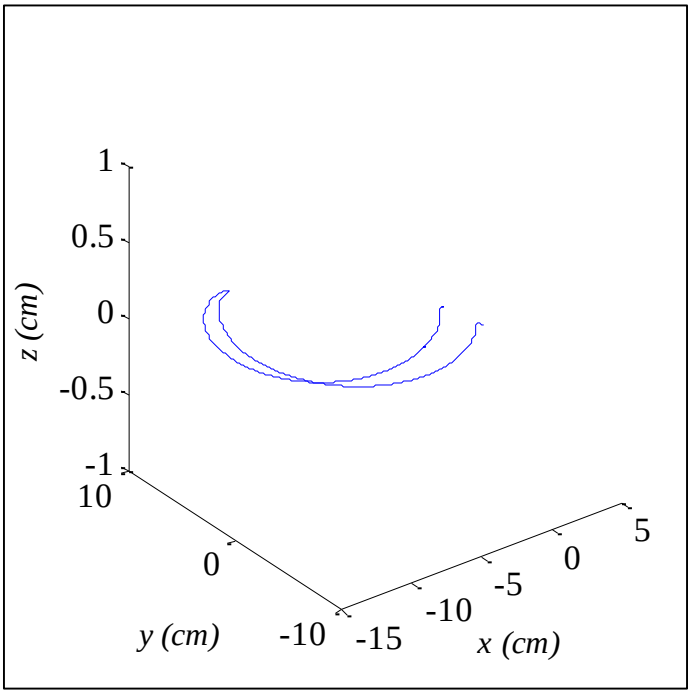

Figure 5.40: IMU sensor Position Output Average
for 10 runs for circular pathway (Methodology 2: Long Path)

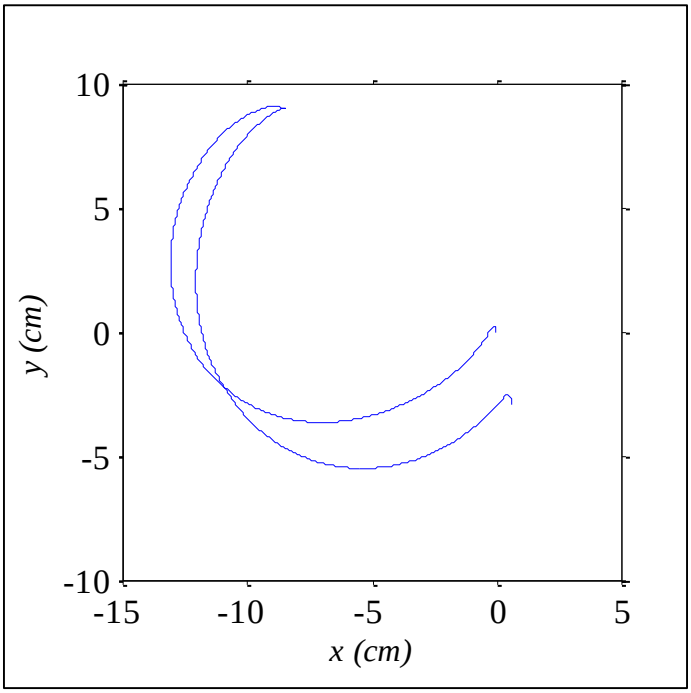

Figure 5.41: *x-y* plane of the position pathway of the sensor (Methodology 2: Long Path)

Similar to the previous approaches, the rotation is performed to transform the coordinate system of the data coming from the IMU sensor. After double integration is performed, the position is outputted by the algorithm as shown in Figure 5.40 in 3D in space. Figure 5.41 shows the x-y plane view of the position profile. The algorithm successfully extracted the pathway of the motion. To overrule the accuracy of the measurement, a reference point is needed for the comparison. Since the methodology dictates the sensor to move along the circular pathway and return to the initial point, the reference used is the initial point itself. This in turn allows for the calculation of the drift bias in the system. Table 5.19 summarizes the measurements and calculation.

Table 5.19: Error calculations for measurements using rotation methodology 2

	x (mm)	***y (mm)***	***z (mm)***
Theoretical	0	0	0
Measured Accuracy	3.70	-25.05	0
Precision	4.38	13.00	0

The position pathway was extracted using the proposed algorithm. To compare for the shape of the circular motion, the theoretical solution for the system is plotted versus the calculations coming from the algorithm as shown in Figure 5.42.

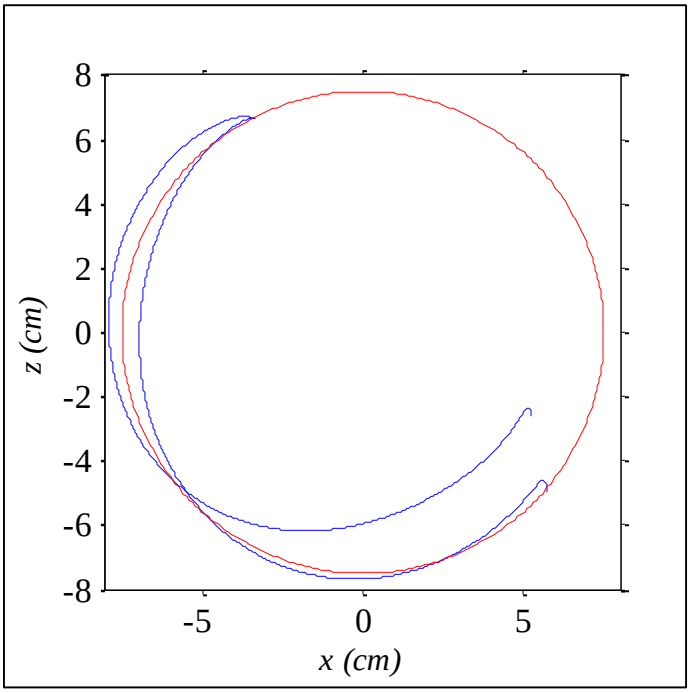

Figure 5.42: Theoretical Vs. Measured Methodology 2: Long Path

5.3 Comparison with Literature Drift Bias Error

This section holds a comparison done between the measurement accuracy obtained in this setup versus other setups from the imported from the literature available. Although the experimental setup is not the same for all the data presented in Table 5.20, however, in terms of drift bias error and its ratio to the total distance, the comparison holds showing the dominance of the proposed method.

Translation measurements were only compared between the proposed algorithm and the literature measurements. More inspection is required with the same experimental setup that the literature is offering to demonstrate the algorithm potential in comparison to the other methodologies.

The absolute error maintained by the proposed algorithm shows potential in terms of its small percentage in comparison with the other methods in three dimensional motion and consistence along all axes.

Table 5.20: Drift Bias Error Comparison

	Axes	Total Distance	Drift Bias Error	Absolute Error
[4]	1 D	2.40 m	0.18 m	7.50 %
[73]	1 D	120.00 m	2.28 m	1.90 %
[74]	2 D	10.00 m	2.00 m	4.00 %
		5.00 m	2.00 m	4.00 %
[75]	3 D	35.00 cm	0.20 cm	0.57 %
		4.00 cm	2.30 cm	57.5 %
		16.50 cm	-1.00 cm	6.06%
Proposed Algorithm	3 D	160.00 cm	2.56 cm	**1.60 %**
		240.00 cm	5.09 cm	**2.01 %**
		40.00 cm	0.81 cm	**2.03 %**

5.4 Profiling System Integration with Microwaves

The IMU sensor was attached to the waveguide and the distance covered was calculated using the algorithm. Figure 5.43 shows the juxtaposing of the voltage as a function of distance.

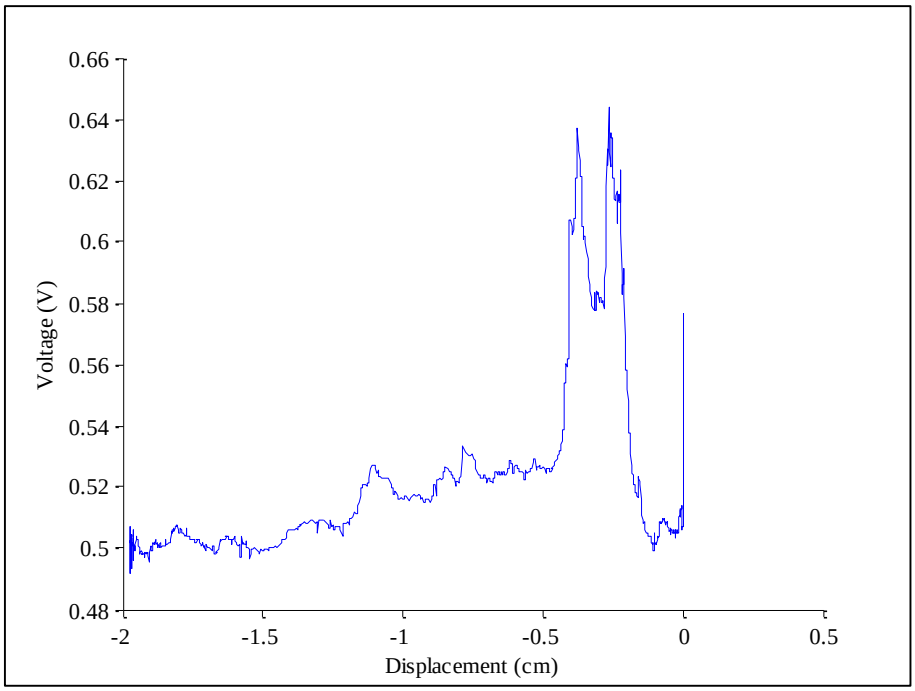

Figure 5.43: Integration of Microwave with Position Tracking

The scan route is along one axis and performed across a metal piece with an induced crack with known width and depth. Based on the microwave theory, the crack is detected by the waveguide. Usually, characterization is needed to capture the width and depth of the crack which is both time consuming and not always accessible.

The width of the jump in the signal should represent the crack width as per the motion, the overall increment in the axis was 2 cm and the crack width as per the IMU algorithm measured to be 1.74 mm whereas the accurate width for the crack is 1.70 mm.

Chapter 6: Conclusions and Future Work

6.1 Conclusions

A replacement for all measurement machines implemented in aid to the detection units whether being microwaves, laser vision systems or any other profiling methodology. The proposed technique can replace the bulky machines in charge of the scanning technique. Bulky scanners not only occupy a big grid of space but also are specifically tailored for specific scanning routes and criteria. The proposed technique does not need specific tailoring or algorithm, but can move freely in any scanning pattern. Moreover, the proposed technique requires a small budget in comparison to the scanning machines.

The proposed technique was tested along a scanning machine with a certain scanning route with small error and uncertainties. The results were analyzed on each index in any axis in 3D and the overall drift bias involved. Due to the usage of the proposed algorithm, the drift bias error usually in meters, was reduced to a few millimeters. The proposed algorithm not only critically reduces the drift bias error but also smoothens the data due to potential vibrations coming from the user as the scanning process is conducted.

Also, the orientation pathway was also tested using a servo motor setup, and not only did the proposed technique capture orientation but also captured the circular pathway along a defined radius. The measurements were extremely close to the theoretical solutions with minor uncertainties corresponding to the bias drift error and noise in the signal.

Given the high precision shown for the proposed algorithm, inspection units can be aided increasing the precision of the overall system and acquiring both realistic and accurate data in the profiling overall. The proposed technique managed to preserve its precision with the theoretical approaches and is on a challenging level with the uncertainty of the conventional bulky scanning measurement machines.

The overall performance of the system can also be further improved by introducing other filters that can further smoothen the input signal to reduce the overall noise that the system is capturing.

6.2 Future Work

The proposed technique was tested along translation in all three axes with various initial orientations. Moreover, the orientation tests were conducted along 2D planes only due to physical and time limitations. Orientation tests must include 3D planes along all axes in a different setup. 3D plane tests are critical due to user movement in free space.

Gimbal lock is a phenomenon that occurs mathematically when gravity is purely in the *x*-axis and the pitch angle values are close to 90 degrees. This however is treated by using a mathematical complex number representation of the angular revolution data called the quaternions. Quaternions are to be introduced to take care of the limitations of the gimbal lock. However, it was not dealt with because the scanning mechanisms do not require the sensor to be at 90 degrees with the surface it profiles in the pitch angle.

The integration of the detection unit with the sensor are yet to be complete as this study did not acquire data in this regards but focused on the position tracking unit only. More integration tests are required to show the compatibility of the system with any detection units.

References

[1] A. Godfrey, R. Conway, D. Meagher, and G. ÓLaighin, "Direct measurement of human movement by accelerometry," *Medical Engineering & Physics*, vol. 30, pp. 1364-1386, 2008.

[2] A. Godfrey, A. K. Bourke, G. M. Ólaighin, P. van de Ven, and J. Nelson, "Activity classification using a single chest mounted tri-axial accelerometer," *Medical Engineering & Physics*, vol. 33, pp. 1127-1135, 2011.

[3] M. A. Lele and J. Gu, "Evaluation of solid state accelerometer sensor for effective position estimation," in *Intelligent Control and Automation (WCICA), 2011 9th World Congress on*, 2011, pp. 959-964.

[4] H. H. S. Liu and G. K. H. Pang, "Accelerometer for mobile robot positioning," *Industry Applications, IEEE Transactions on*, vol. 37, pp. 812-819, 2001.

[5] R. Onodera and N. Mimura, "Stability and Error Analysis of A New 6 DOF Motion Sensor Using Multiple Accelerometers," in *Sensors, 2007 IEEE*, 2007, pp. 752-755.

[6] C. Hyunju, K. Sangchul, B. Jinsuk, and P. S. Fisher, "Motion recognition with smart phone embedded 3-axis accelerometer sensor," in *Systems, Man, and Cybernetics (SMC), 2012 IEEE International Conference on*, 2012, pp. 919-924.

[7] R. Ferrero, F. Gandino, B. Montrucchio, M. Rebaudengo, A. Velasco, and I. Benkhelifa, "On gait recognition with smartphone accelerometer," in *Embedded Computing (MECO), 2015 4th Mediterranean Conference on*, 2015, pp. 368-373.

[8] H. Jeon, S. K. Kim, B. Jeon, and P. Kwang Suk, "Distance estimation from acceleration for quantitative evaluation of Parkinson tremor," in *Engineering in Medicine and Biology Society, EMBC, 2011 Annual International Conference of the IEEE*, 2011, pp. 393-396.

[9] M. Patterson, D. McGrath, and B. Caulfield, "Using a tri-axial accelerometer to detect technique breakdown due to fatigue in distance runners: A preliminary perspective," in *Engineering in Medicine and Biology Society, EMBC, 2011 Annual International Conference of the IEEE*, 2011, pp. 6511-6514.

[10] B. Ying-Wen, Y. Chia-Hao, and W. Siao-Cian, "Using a three-axis accelerometer and GPS module in a smart phone to measure walking steps and distance," in *Electrical and Computer Engineering (CCECE), 2014 IEEE 27th Canadian Conference on*, 2014, pp. 1-6.

[11] K. Tumkur and S. Subbiah, "Modeling Human Walking for Step Detection and Stride Determination by 3-Axis Accelerometer Readings in Pedometer," in *Computational Intelligence, Modelling and Simulation (CIMSiM), 2012 Fourth International Conference on*, 2012, pp. 199-204.

[12] E. Beanland, L. C. Main, B. Aisbett, P. Gastin, and K. Netto, "Validation of GPS and accelerometer technology in swimming," *Journal of Science and Medicine in Sport*, vol. 17, pp. 234-238, 2014.

[13] J. Kowal, S. Blok, and A. Sioma, "Determining the orientation of a body in space using the Kalman filter," in *Carpathian Control Conference (ICCC), 2012 13th International*, 2012, pp. 376-381.

[14] J. Xunsheng, W. Shourong, X. Yishen, S. Qin, and X. Dunzhu, "Application of the Digital Signal Procession in the MEMS Gyroscope De-drift," in *Nano/Micro*

Engineered and Molecular Systems, 2006. NEMS '06. 1st IEEE International Conference on, 2006, pp. 218-221.

[15] J. F. Arrigo and P. M. Chau, "Power aware attitude computation during rapid rotational motion," *Instrumentation and Measurement, IEEE Transactions on,* vol. 55, pp. 63-69, 2006.

[16] W. Zongwei, Y. Minli, M. Hongguang, J. Weimin, and T. Fanghao, "Low-Cost Antenna Attitude Estimation by Fusing Inertial Sensing and Two-Antenna GPS for Vehicle-Mounted Satcom-on-the-Move," *Vehicular Technology, IEEE Transactions on,* vol. 62, pp. 1084-1096, 2013.

[17] J. Chao and B. L. Evans, "Online Camera-Gyroscope Autocalibration for Cell Phones," *Image Processing, IEEE Transactions on,* vol. 23, pp. 5070-5081, 2014.

[18] R. Bieda, R. Grygiel, and A. Galuszka, "Naive Kalman filtering for estimation of spatial object orientation," in *Methods and Models in Automation and Robotics (MMAR), 2015 20th International Conference on*, 2015, pp. 955-960.

[19] A. E. Barabanov and D. V. Romaev, "Adaptive filtering of tracking camera data and onboard sensors for a small helicopter autopilot," in *Control Applications, (CCA) & Intelligent Control, (ISIC), 2009 IEEE*, 2009, pp. 1696-1701.

[20] Z. Junchuan, E. Edwan, S. Knedlik, and O. Loffeld, "Low-cost INS/GPS with nonlinear filtering methods," in *Information Fusion (FUSION), 2010 13th Conference on*, 2010, pp. 1-8.

[21] X. Xingguo, W. Yu-Liang, and J. Wen-Ben, "Material Fatigue and Reliability of MEMS Accelerometers," in *Defect and Fault Tolerance of VLSI Systems, 2008. DFTVS '08. IEEE International Symposium on*, 2008, pp. 314-322.

[22] D. L. DeVoe and A. P. Pisano, "Surface micromachined piezoelectric accelerometers (PiXLs)," *Microelectromechanical Systems, Journal of,* vol. 10, pp. 180-186, 2001.

[23] R. Muscillo, M. Schmid, S. Conforto, and T. D'Alessio, "An adaptive Kalman-based Bayes estimation technique to classify locomotor activities in young and elderly adults through accelerometers," *Medical Engineering & Physics,* vol. 32, pp. 849-859, 2010.

[24] H. Yanling and L. Zhiping, "Analysis and Compensation on Static Error of Accelerometer in GFSINS," in *Measuring Technology and Mechatronics Automation, 2009. ICMTMA '09. International Conference on*, 2009, pp. 429-432.

[25] S. Shafigh, T. Zia, and N. Mouzehkesh, "Wireless accelerometer sensor data filtering using Recursive Least Squares adaptive filter," in *Intelligent Sensors, Sensor Networks and Information Processing, 2013 IEEE Eighth International Conference on*, 2013, pp. 66-70.

[26] W. Hernandez, J. de Vicente, O. Sergiyenko, Ferna, x, and E. ndez, "Improving the Performance of an Accelerometer by Using a BLMS Adaptive Filter," in *Sensor Device Technologies and Applications (SENSORDEVICES), 2010 First International Conference on*, 2010, pp. 221-225.

[27] W. T. Latt, U. X. Tan, C. Y. Shee, and W. T. Ang, "Identification of accelerometer orientation errors and compensation for acceleration estimation errors," in *Robotics and Automation, 2009. ICRA '09. IEEE International Conference on*, 2009, pp. 1232-1237.

[28] L. Wang, S. W. Su, B. G. Celler, and E. Ambikairajah, "Analysis of Orientation Error of Triaxial Accelerometers on the Assessment of Energy Expenditure," in

Engineering in Medicine and Biology Society, 2005. IEEE-EMBS 2005. 27th Annual International Conference of the, 2005, pp. 3514-3517.

[29] W. Dargie and M. K. Denko, "Analysis of Error-Agnostic Time- and Frequency-Domain Features Extracted From Measurements of 3-D Accelerometer Sensors," *Systems Journal, IEEE*, vol. 4, pp. 26-33, 2010.

[30] C. Jagadish and C. Bor-Chin, "Diversified redundancy in the measurement of Euler angles using accelerometers and magnetometers," in *Decision and Control, 2007 46th IEEE Conference on*, 2007, pp. 2669-2674.

[31] D. Pei and W. Sheng, "An Accelerometer Error Compensation Method Based on Forward Velocity Estimation," in *Instrumentation, Measurement, Computer, Communication and Control (IMCCC), 2013 Third International Conference on*, 2013, pp. 652-657.

[32] Y. Huang, J. Chen, and P. Yin Li, "Experimental analysis of accelerometer installation error," in *Computer, Mechatronics, Control and Electronic Engineering (CMCE), 2010 International Conference on*, 2010, pp. 40-42.

[33] F. Jiancheng and L. Zhanchao, "A New Inclination Error Calibration Method of Motion Table Based on Accelerometers," *Instrumentation and Measurement, IEEE Transactions on*, vol. 64, pp. 487-493, 2015.

[34] H. Jiqiang, H. Junfen, Z. Yong, J. Lipei, X. Long, and H. Minshuang, "Study on a Pipe Welding Robot based on Laser Vision Sensing," in *Robotics, Automation and Mechatronics, 2008 IEEE Conference on*, 2008, pp. 720-723.

[35] W. Huang and R. Kovacevic, "A Laser-Based Vision System for Weld Quality Inspection," *SENSORS*, vol. 11, pp. 506-521, 2011.

[36] S. Liu, L. Liu, H. Zhang, J. Bai, and G. Wang, "Study of robot seam tracking system with laser vision," in *Mechatronics and Automation, 2009. ICMA 2009. International Conference on*, 2009, pp. 1296-1301.

[37] R. S. Lu, Y. F. Li, and Q. Yu, "On-line measurement of the straightness of seamless steel pipes using machine vision technique," *Sensors and actuators. A. Physical.*, vol. 94, pp. 95-101, 2001.

[38] P. Schalk, R. Ofner, and P. O'Leary, "Pipe eccentricity measurement using laser triangulation," *Image and Vision Computing*, vol. 25, pp. 1194-1203, 2007.

[39] T. A. Davis and Y. C. Shin, "Vision-based clad height measurement," *Machine Vision and Applications*, vol. 22, pp. 129-136, 2011.

[40] K. Min-Goo, K. Joon-Hong, P. Young-Jun, and W. Gap-Joo, "Laser vision system for automatic seam tracking of stainless steel pipe welding machine (ICCAS 2007)," in *Control, Automation and Systems, 2007. ICCAS '07. International Conference on*, 2007, pp. 1046-1051.

[41] P. Kim, S. Rhee, and C. H. Lee, "Automatic teaching of welding robot for free-formed seam using laser vision sensor," *Optics and Lasers in Engineering*, vol. 31, pp. 173-182, 1999.

[42] P. Xu, X. Tang, and S. Yao, "Application of circular laser vision sensor (CLVS) on welded seam tracking," *Journal of Materials Processing Tech*, vol. 205, pp. 404-410, 2008.

[43] S. Yong-Hua, W. Guo-Rong, and L. Guo-Jin, "Adaptive Robotic Welding System Using Laser Vision Sensing for Underwater Engineering," in *Control and Automation, 2007. ICCA 2007. IEEE International Conference on*, 2007, pp. 1213-1218.

[44] F. Xi and C. Shu, "CAD-based path planning for 3-D line laser scanning," *Computer-Aided Design*, vol. 31, pp. 473-479, 1999.

[45] F. Prieto, R. Lepage, P. Boulanger, and T. Redarce, "A CAD-based 3D data acquisition strategy for inspection," *Machine Vision and Applications,* vol. 15, pp. 76-91, 2003.
[46] Z. Qu, A. Bennecer, C. Selcuk, and T.-H. Gan, "Development of a laser-based weld flaw identification system."
[47] Z. Zhengyou, "Flexible camera calibration by viewing a plane from unknown orientations," in *Computer Vision, 1999. The Proceedings of the Seventh IEEE International Conference on,* 1999, pp. 666-673 vol.1.
[48] F. Zhou and G. Zhang, "Complete calibration of a structured light stripe vision sensor through planar target of unknown orientations," *Image and Vision Computing,* vol. 23, pp. 59-67, 2005.
[49] A. ElSoussi, A. E. Al Alami, and B. Abu-Nabah, "Virtual Environment Assessment for Laser-Based Vision Surface Profiling," *AIP Conference Proceedings,* vol. 1650, pp. 1326-1333, 2015.
[50] J. Forest, J. Salvi, E. Cabruja, and C. Pous, "Laser stripe peak detector for 3D scanners. A FIR filter approach," in *Pattern Recognition, 2004. ICPR 2004. Proceedings of the 17th International Conference on,* 2004, pp. 646-649 Vol.3.
[51] Z. D. Yang, P. Wang, X. H. Li, and C. K. Sun, "3D laser scanner system using high dynamic range imaging," *Optics and Lasers in Engineering,* vol. 54, pp. 31-41, 2014.
[52] C. Huber and R. Zoughi, "Detecting stress and fatigue cracks," *IEEE Potentials,* vol. 15, pp. 20-24, 1996.
[53] S. Gupta, A. Ray, and E. Keller, "Online fatigue damage monitoring by ultrasonic measurements: A symbolic dynamics approach," *International Journal of Fatigue,* vol. 29, pp. 1100-1114, 2007.
[54] Y. Ju, M. Saka, and Y. Uchimura, "Evaluation of the shape and size of 3D cracks using microwaves," *NDT and E International,* vol. 38, pp. 726-731, 2005.
[55] S. Kharkovsky, M. T. Ghasr, and R. Zoughi, "Near-Field Millimeter-Wave Imaging of Exposed and Covered Fatigue Cracks," *Instrumentation and Measurement, IEEE Transactions on,* vol. 58, pp. 2367-2370, 2009.
[56] A. M. Sabatini, "Quaternion-based extended Kalman filter for determining orientation by inertial and magnetic sensing," *Biomedical Engineering, IEEE Transactions on,* vol. 53, pp. 1346-1356, 2006.
[57] B. Huyghe, J. Doutreloigne, and J. Vanfleteren, "3D orientation tracking based on unscented Kalman filtering of accelerometer and magnetometer data," in *Sensors Applications Symposium, 2009. SAS 2009. IEEE,* 2009, pp. 148-152.
[58] H. Himberg, Y. Motai, and C. Barrios, "R-adaptive kalman filtering approach to estimate head orientation for driving simulator," in *Intelligent Transportation Systems Conference, 2006. ITSC '06. IEEE,* 2006, pp. 851-857.
[59] H. P. Bruckner, C. Spindeldreier, and H. Blume, "Modification and fixed-point analysis of a Kalman filter for orientation estimation based on 9D inertial measurement unit data," in *Engineering in Medicine and Biology Society (EMBC), 2013 35th Annual International Conference of the IEEE,* 2013, pp. 3953-3956.
[60] J. L. Marins, Y. Xiaoping, E. R. Bachmann, R. B. McGhee, and M. J. Zyda, "An extended Kalman filter for quaternion-based orientation estimation using MARG sensors," in *Intelligent Robots and Systems, 2001. Proceedings. 2001 IEEE/RSJ International Conference on,* 2001, pp. 2003-2011 vol.4.

[61] J. Go, x015B, li, x, ski, W. Giernacki, *et al.*, "Unscented Kalman Filter for an orientation module of a quadrotor mathematical model," in *Control Conference (ASCC), 2013 9th Asian*, 2013, pp. 1-6.

[62] K. R. Sharma, D. Honc, F. Du, x, and ek, "Sensor fusion for prediction of orientation and position from obstacle using multiple IR sensors an approach based on Kalman filter," in *Applied Electronics (AE), 2014 International Conference on*, 2014, pp. 263-266.

[63] R. G. Valenti, I. Dryanovski, and X. Jizhong, "A Linear Kalman Filter for MARG Orientation Estimation Using the Algebraic Quaternion Algorithm," *IEEE Transactions on Instrumentation and Measurement*, vol. 65, pp. 467-481, 2016.

[64] S. h. Won, W. Melek, and F. Golnaraghi, "Position and orientation estimation using Kalman filtering and particle diltering with one IMU and one position sensor," in *Industrial Electronics, 2008. IECON 2008. 34th Annual Conference of IEEE*, 2008, pp. 3006-3010.

[65] S. Sabatelli, M. Galgani, L. Fanucci, and A. Rocchi, "A double stage Kalman filter for sensor fusion and orientation tracking in 9D IMU," in *Sensors Applications Symposium (SAS), 2012 IEEE*, 2012, pp. 1-5.

[66] S. Zihajehzadeh, D. Loh, M. Lee, R. Hoskinson, and E. J. Park, "A cascaded two-step Kalman filter for estimation of human body segment orientation using MEMS-IMU," in *Engineering in Medicine and Biology Society (EMBC), 2014 36th Annual International Conference of the IEEE*, 2014, pp. 6270-6273.

[67] Y. Xiaoping, M. Lizarraga, E. R. Bachmann, and R. B. McGhee, "An improved quaternion-based Kalman filter for real-time tracking of rigid body orientation," in *Intelligent Robots and Systems, 2003. (IROS 2003). Proceedings. 2003 IEEE/RSJ International Conference on*, 2003, pp. 1074-1079 vol.2.

[68] Z. Q. Zhang, X. L. Meng, and J. K. Wu, "Quaternion-Based Kalman Filter With Vector Selection for Accurate Orientation Tracking," *Instrumentation and Measurement, IEEE Transactions on*, vol. 61, pp. 2817-2824, 2012.

[69] G. Pengfei, T. Liqiong, and S. Mukhopadhyay, "MEMS based IMU for tilting measurement: Comparison of complementary and kalman filter based data fusion," in *Industrial Electronics and Applications (ICIEA), 2015 IEEE 10th Conference on*, 2015, pp. 2004-2009.

[70] R. Diamant and J. Yunye, "A Machine Learning Approach for Dead-Reckoning Navigation at Sea Using a Single Accelerometer," *Oceanic Engineering, IEEE Journal of*, vol. 39, pp. 672-684, 2014.

[71] S. P. Tseng, W. L. Li, C. Y. Sheng, J. W. Hsu, and C. S. Chen, "Motion and attitude estimation using inertial measurements with complementary filter," in *Control Conference (ASCC), 2011 8th Asian*, 2011, pp. 863-868.

[72] L. Xiang, H. Chuan, W. Yongjun, and L. Zhi, "Generalized complementary filter for attitude estimation based on vector observations and cross products," in *Information and Automation, 2015 IEEE International Conference on*, 2015, pp. 1733-1737.

[73] X. Yun, E. R. Bachmann, H. Moore, and J. Calusdian, "Self-contained Position Tracking of Human Movement Using Small Inertial/Magnetic Sensor Modules," in *Proceedings 2007 IEEE International Conference on Robotics and Automation*, 2007, pp. 2526-2533.

[74] E. Akeila, Z. Salcic, and A. Swain, "Reducing Low-Cost INS Error Accumulation in Distance Estimation Using Self-Resetting," *Instrumentation and Measurement, IEEE Transactions on*, vol. 63, 2014.

[75] P. Axelsson and M. Norrlof, "Method to Estimate the Position and Orientation of a Triaxial Accelerometer Mounted to an Industrial Manipulator," *IFAC Proceedings Volumes,* vol. 45, pp. 283-288, 2012.

Vita

Bassel Mohamad Al Homssi born on October 5, 1991 in Al Ain, UAE. He accomplished his high school education in Wesgreen International School in Sharjah, UAE. Later on, he joined the American University of Sharjah in 2009 to acquire his Bachelor of Science in Electrical Engineering in 2013. Post-graduation, he joined Drake & Scull Engineering for nine months as a Procurement Engineer in Dubai, UAE. Driven by research passion, he later rejoined the American University of Sharjah in 2014 to complete his Masters of Science in Electrical Engineering in 2016. His research area includes Electromagnetics, Microwave Systems, Laser Profiling Systems and Digital Signal Processing.